David Prochinig , BSc BSc

Ptychographic X-ray Computed Tomography Study of the Paper Pulp Fiber to Fiber Bond

MASTER'S THESIS

to achieve the university degree of

Diplom - Ingenieur

Master's degree programme: Technical Physics

submitted to

Graz University of Technology

Supervisor

Ao.Univ.-Prof. Mag. Dr.rer.nat. Robert Schennach

Institute of Solid State Physics

Graz, June 2020

AFFIDAVIT

I declare that I have authored this thesis independently, that I have not used other than the declared sources/resources, and that I have explicitly indicated all material which has been quoted either literally or by content from the sources used. The text document uploaded to TUGRAZonline is identical to the present master's thesis.

Date, Signature

Abstract

Paper consists of a network of cellulose fibers bonded to each other without the aid of glue or adhesive. These bonds play a major role in the overall strength of paper. Several mechanisms are responsible for the bonding, though the contributions of each mechanism are not exactly known to this day. For a reliable estimation of the contribution of intermolecular bonding mechanisms, as Coulomb forces, van der Waals forces and hydrogen bonding, the area in molecular contact between two bonded cellulose fibers, called FtF-bond, has to be known precisely.
In this Master's Thesis, ptychographic X-ray computed tomography measurements were performed to determine the contact area of FtF-bonds. The measurement technique utilizes highly brilliant, coherent X-rays from a synchrotron source, passing through the sample. The X-ray intensity is recorded in the far field and used to reconstruct the phase information of the X-ray wave-field, in the sample plane, via ptychography. Combined with computed tomography, this not only allows for high-resolution 3D reconstructions of the sample morphology, but also the sample's refractive index and thus, a quantitative analysis. In total, two FtF-bonds made from bleached hardwood kraft pulp were measured at about 90 K and ultra-high vacuum and one FtF-bond consisting of unbleached softwood kraft pulp was measured at ambient conditions.
The experiments and the resulting 3D reconstructions revealed a variety of findings. First of all, it was demonstrated that this technique is very promising for the characterization of cellulosic material. Moreover, it was shown that radiation damage to cellulose is relevant and has to be considered in measurements with ionizing radiation. Furthermore, the optimal parameters for this type of measurement were obtained. In addition, the relative contact area of FtF-bonds was estimated from 3D reconstructions with a resolution in the range of 50 nm and 90 nm and an isotropic voxel size of 37.6 nm. This is amongst the best resolutions reported on measurements of cellulose FtF-bonds to this day. Furthermore, the 3D reconstructions allowed for an estimation of the mass density of the cellulose samples. Additionally, several sample preparation methods were examined, revealing that simple manual sample preparation is in principle possible, but further experiments with these samples have to be made at the synchrotron facility.

Special thanks to Eduardo Machado-Charry, Robert Schennach, Roland Resel, Georg Urstöger and the whole team of the cSAXS beamline at the Swiss Light Source.

Contents

1 Introduction

Paper is a very versatile material used in various applications, ranging from packaging of goods to standard writing and printing paper in offices or tissue paper for hygiene. It is one of the oldest materials used by humanity and is still of utmost importance in this day and age, especially due to the increasing demand for paper as a packaging material [1]. This is partly due to the need to replace plastic with more environmentally friendly products. In order to meet these expectations, the industry faces two important challenges: On the one hand, to provide paper products strong enough for any type of packaging, on the other hand to reduce the energy consumption and the environmental impact. The latter seems particularly clear in view of the fact, that the paper industry is still considered one of the most polluting industrial sectors in many places, especially due to the high demand for energy and natural resources like wood or water [2].

Nevertheless, paper is an easily recyclable material. It consists of a network of cellulose fibers that bond to each other without the aid of glue or adhesive, thus the bonds are fully reversible. These bonds contribute significantly to the strength of paper [3], though they are not fully understood to this day. Especially the contributions of the underlying binding mechanisms are a matter of debate among researchers. Furthermore, the strength of the bonds also depends on the fiber bond area, i.e., the area in molecular contact. Several attempts have been made by various groups to characterize the actual bonded area, utilizing different methods like confocal laser scanning microscopy [4], polarization microscopy [5] and microtome serial sectioning [6] or X-ray nanotomography [7], only to name a few. Though all of these techniques faced the problem of accuracy, as the relevant length scales are in the molecular regime. Hence, new methods have to be examined that are capable of accurately quantifying the contact area between bonded cellulose fibers.

Ptychographic X-ray computed tomography (PXCT) is a coherent diffractive imaging technique that has shown to provide 3D reconstructions of the sample's refractive index with a resolution in the nanometer regime [8]. It utilizes highly brilliant coherent X-rays from a synchrotron source to scan the sample from various angles. The X-ray intensity is recorded and used to reconstruct the phase information of the X-ray wave-field in the sample plane, thus allowing for high contrast images. Another advantage is that the phase information is proportional to the sample's refractive index and the electron density, which allows for quantitative high-resolution 3D electron density maps [9].

The goal of this Master's Thesis is to characterize the bond between two cellulose fibers using PXCT with a resolution in the regime of tens of nanometers. The following scientific questions will be addressed:

- Is there a simple and efficient way for sample preparation?
- Is PXCT suitable to measure cellulose samples with high accuracy?
- How do cellulose samples behave upon long and intense radiation exposure?
- What are the optimal parameters for PXCT measurements with cellulose samples?
- How does the bond between two cellulose fibers look like and what is the actually bonded area?

2 Theory

2.1 Paper

Paper consists of a network of almost randomly oriented cellulose fibers, which are bonded at certain points, creating a composite material with notable strength per unit area. Bonding takes place without the use of any glue or adhesive. The bonds between cellulose fibers are called fiber to fiber (FtF) bonds and are amongst the most important elements affecting paper strength, besides network- and fiber properties. According to Page [3], the tensile strength of paper depends on the strength of the individual fibers and the strength of the individual FtF-bonds. Cellulose fibers are usually acquired from wood by so-called pulping processes. The properties of cellulose fibers depend on many factors, as the type of wood used to obtain the fibers and the processing steps of the wood and the fibers.

2.1.1 Wood, Pulping Processes and Papermaking

Wood Wood can be categorized into the groups hardwood and softwood, according to their anatomical features. Softwoods are gymnosperm, coniferous trees which carry needles throughout the whole year and hardwoods are angiosperm, deciduous trees with broad leaves that are dropped seasonally. Despite the classification into hard- and softwood, softwoods are not generally softer than hardwoods and vice versa. Furthermore, softwoods are evolutionary older and thus simpler in structure than hardwoods.
Trees have an outer bark layer and an inner wood cylinder. In between the bark and the wood there is the so-called cambium, which is responsible for forming new wood cells. The tissue inside the cambium is called xylem and outside of it phloem. Due to the seasonal differences in cell wall thickness and/or diameter, trees form so-called growth rings. Within the growth rings, a distinction between earlywood and latewood can be made. Earlywood cells are formed in the beginning of a vegetation period and are characterized by a large diameter and a thin cell wall. In contrast, latewood cells are formed in the end of a vegetation period and are usually smaller cells with a thick cell wall. Earlywood cells are usually responsible for the transport of water, whereas latewood cells serve the purpose of mechanically supporting the tree. Moreover, as the location of the cambium suggests, the wood growth takes place in radial direction. Thus, the inner region of a tree, called heartwood, is older than the region around the cambium, which is called sapwood. Heartwood consists of physiologically inactive (dead) cells, whereas sapwood consists of physiologically active (living) cells. [10]
The schematic cross-section of a tree is sketched in fig. (1).

Wood consists of different types of cells. Approximately $90-95\,\%$ of the cells in softwood are ordinary tracheids. Thus, its structure is simpler compared to that of hardwood with roughly $50\,\%$ of the cells being tracheids. Tracheids usually serve the purpose of transporting water and are long and slender cells mostly oriented longitudinally within a tree. Wood cells differ in structure, as they serve different functions. The basic functions are of mechanical, storing, transporting and secreting nature. The simpler softwood consists of basically two types of cells, namely tracheids and parenchyma cells, which fulfill the aforementioned functions. Different types of tracheids fulfill the mechanical and the transport function and different types of parenchyma cells fulfill the storing and secreting

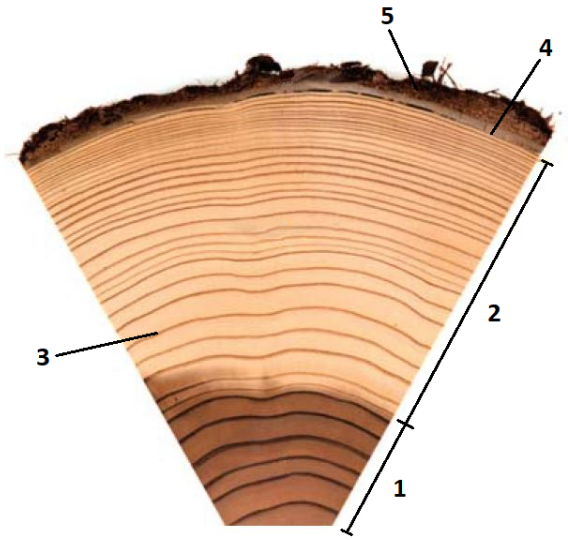

Fig. 1: Cross section of a tree - adapted from [10]
1 ... heartwood, 2 ... sapwood, 3 ... growth ring, 4 ... cambium, 5 ... bark, 1 and 2 together form the xylem and the phloem is located between 4 and 5

function. In hardwoods, the mechanical function is performed by libriform fibers and fiber tracheids, the transport function by vessels and vessel tracheids, the storing function by ray- and longitudinal parenchyma and the secreting function by epithelial cells. [11]

The walls of wood cells consist of cellulose, hemicellulose, lignin, extractives and minerals, with the main constituent usually being cellulose. Typical European woods have a mass fraction of about $40-44\,\%$ cellulose. The content of hemicellulose for softwoods is roughly $25-30\,\%$ and for hardwoods $30-35\,\%$. The lignin content for softwoods is usually between $25\,\%$ and $32\,\%$ and between $18\,\%$ and $25\,\%$ for hardwoods. Furthermore, most European woods contain about $1-5\,\%$ extractives and $0.1-1\,\%$ minerals or ash. [10]
A more detailed description about the constituents of wood cell walls, i.e., cellulose fibers, is given in section 2.1.2.

Pulping Processes In paper technology, pulping processes are used to gather cellulose fibers, usually from wood. There are two main methods of pulping, namely mechanical- and chemical pulping, which can also be combined. As the name suggests, chemical pulping makes use of chemical reactions to release the fibers from the wood matrix. The advantage is that there is no need for external energy for the process. However, in return, only about $50\,\%$ of the wood is transformed into pulp, whereas the rest is dissolved. Thus, chemical pulping usually makes use of recovery systems, where the cooking chemicals and the energy in the dissolved material is reused. In contrast, mechanical methods have a much higher yield, making use of nearly everything of the whole wood input. However, the disadvantage is the high demand for electric energy. Furthermore, bleaching steps are performed to obtain brighter paper, remove impurities and prevent paper aging. [12]

Mechanical pulp is produced by using grinders that are fed with wood logs or wood chips. Extractives are lost in the process, leading to a pulp output lower than $100\,\%$, but greater

than 90 %. The obtained fibers are usually stiff and mostly uncollapsed. Additionally, some smaller fibers, called fines, are obtained, which consist of broken fibers and fragments of the fiber walls. So-called groundwood pulp is obtained by using stone grinders. Round wood logs are fed parallel to a rotating sandstone cylinder and pressed against it, such that fibers are shaved off. A second method makes use of refining plates to obtain the so-called refiner pulp. The machine is fed with wood chips, which are shredded by two rotating plates. The plates have groove marks which are usually coarse in the center and finer towards the edge of the plate. [12]

Chemical pulping is based on the removal of lignin from the wood matrix, since lignin plays a major role in holding the fibers together, acting as glue. The removal of lignin is called delignification and is conducted by decomposing the lignin molecules into charged groups, which are eventually washed out. However, pulping chemicals are not fully selective towards lignin as they also degrade carbohydrates of the wood. Thus, the process is stopped at a certain point with lignin remaining in the pulp. The most prominent chemical pulping method is Kraft cooking, which is named after the German and Swedish word "Kraft" meaning strength, as Kraft pulp fibers are more robust than mechanical pulp fibers. The chemicals used for Kraft cooking are sodium hydroxide NaOH and sodium sulfide Na_2S, where OH^- and HS^- act as active cooking species. Hydrogen sulfide is responsible for delignification, while hydroxide keeps the lignin fragments in solution. [12]

As mentioned before, after creating the pulp, the fibers may get bleached if needed for the paper product. Paper made from bleached fibers is much whiter, allowing for better contrast between the paper and the print. Furthermore, impurities are reduced and the paper lasts longer. Bleaching can also reduce the amount of lignin in the fibers, however lignin-removing bleaching is mostly applied to chemical pulps. Typically, chemical pulps are pre-bleached with oxygen prior to treatment with the actual bleaching agents. A typical bleaching agent for chemical pulps as well as for mechanical pulps is hydrogen peroxide. [12]

Papermaking In order to create paper, the pulp fibers have to be processed to form a network. The basic idea is to make a dilute suspension of fibers in water, which is then pressed and dried to obtain paper. This process can be performed without the aid of glue, as the fibers bond to each other when pressed and dried. To do so, paper machines, as sketched in fig. (2), were created. In the headbox, the fiber suspension is sprayed onto the moving belt, also known as wire, uniformly. The suspension may contain some additives to control or change paper properties. The moving belt is a woven fabric that supports the fiber suspension and additionally allows the water to flow off. In the press section, the suspension is pressed with a press felt and a press roll to remove water. The water content is further reduced in the drying section using hot cylinders, which are steam heated. After drying, the paper web is calendered and coated to smoothen and flatten the surface. Eventually, the paper web is reeled up on a roll. [12]

2.1.2 Cellulose Fibers

Since the main constituents of wood fibers are cellulose molecules, they are named cellulose fibers. Besides cellulose, they also contain hemicellulose, lignin and a small portion of

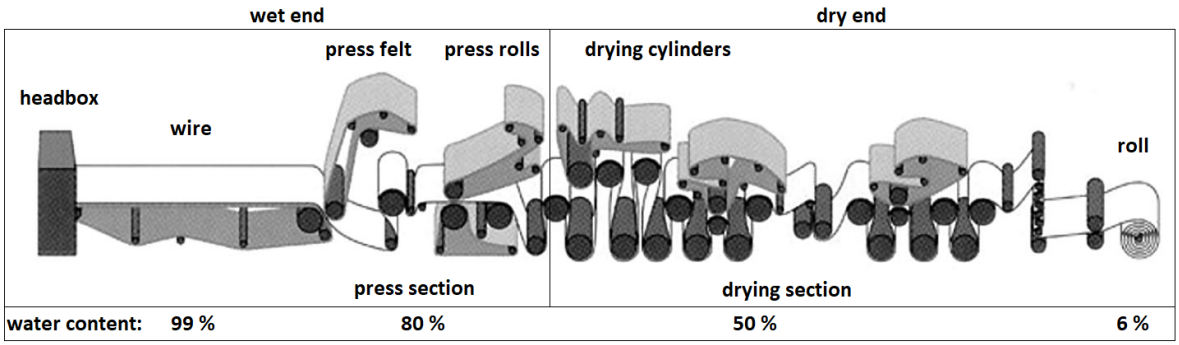

Fig. 2: Sketch of a Fourdrinier papermachine - adapted from [12]

extractives and minerals. Cellulose is a linear, organic polymer consisting of a single type of saccharide and is thus a homopolysaccharide. The chain is made of repeating β-(1,4)-glycosidically bonded *D*-glucose units [10]. Wood cellulose has a degree of polymerization of about 10000 [13]. The glucose occurs in the form of pyranose rings in the $^4C_1$ confirmation, which is thermodynamically most stable and contains equatorial hydroxyl (OH) groups (see fig. (3)). Hydrogen bonding gives rise to a hierarchical structure in cellulose. Hydrogen bonds within the chains make them highly oriented and rigid. Parallel chains are bonded via regular H-bonding and form cellulose sheets. The sheets interact via van der Waals forces and hydrophobic interactions, forming crystalline fibrils. Furthermore, parallel fibrils, as well as the fibrils ends, can bond via hydrogen bonding, giving rise to so-called microfibrils [10]. One microfibril cross-section contains about $30-200$ fibrils [13]. The size of the microfibrils depends on the type of wood. They are typically between 2 and 30 nm in diameter and up to several micrometers in length [14].

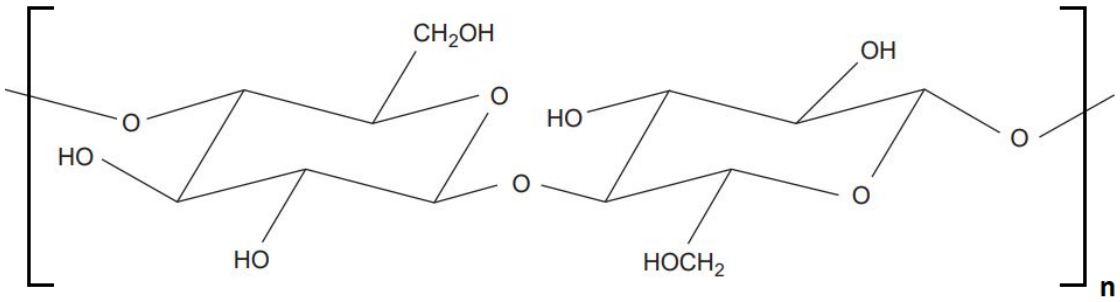

Fig. 3: Repeating unit of the cellulose chain - adapted from [13]

Hemicellulose is a general term for heteropolysaccharides that occur in plants. Compared to cellulose they consist of several, mostly branched sugars with lower molecular masses. In cellulose fibers they are located between the microfibrils [13]. The degree of polymerization is about $50-200$, which is much lower than that of cellulose. The main role of hemicelluloses within cellulose fibers is strengthening the cell wall due to interaction with cellulose and lignin. The two most important hemicelluloses in wood are xylans and mannans with different occurrences in hard- and softwood. Hardwood contains about $10-35\,\%$ xylans and $2-5\,\%$ mannans, whereas softwood has about $7-15\,\%$ xylans and

$15 - 23\,\%$ mannans. The repeating unit of xylan is *D*-Xylose and that of mannans is *D*-mannose. [10]

Lignin consists of an aromatic system composed of phenylpropane units. It is an amorphous substance located between the microfibrils, mostly in the middle lamella and the secondary walls and plays an important role in strengthening the cell wall [11]. Lignin is sometimes referred to as wood's "glue" which holds the fibers together [12].

Extractives are compounds with a low molecular mass. As the name suggests, they can be extracted from wood with organic solvents or hot water. Typical extractives of softwoods and hardwoods are terpenes and tannins, respectively, but the occurrence strongly depends on the tree species. [10]

The wall of a cellulose fiber consists of several layers, as depicted in fig. (4). The so-called lumen (L) is located in the center of a fiber and is responsible for the transport of water. Around the lumen, there are usually three stiff secondary wall layers (S1, S2, S3). The S3 layer is usually very thin and the S2 layer is the thickest. The secondary wall mainly consists of cellulose and hemicellulose. The microfibrils within the layers have different orientations relative to the longitudinal cell axis, as indicated in fig. (4). The angle between the microfibrils and the longitudinal cell axis is roughly $50 - 75°$ in the S1 layer, $10 - 30°$ in the S2 layer and $60 - 80°$ in the S3 layer. Furthermore, the microfibrils in the S2 layer are more closely packed compared to the fibrils of the other layers. The layer outside of the secondary wall is the primary wall (P), which is again surrounded by a layer called the middle lamella (ML). The primary wall has a matrix consisting of pectin and hemicellulose in which cellulosic material is embedded. Thus, the orientation of the microfibrils is random. The middle lamella serves as a separation layer between adjacent cellulose fibers. Additionally, the wall gets incrusted with lignin. [10]

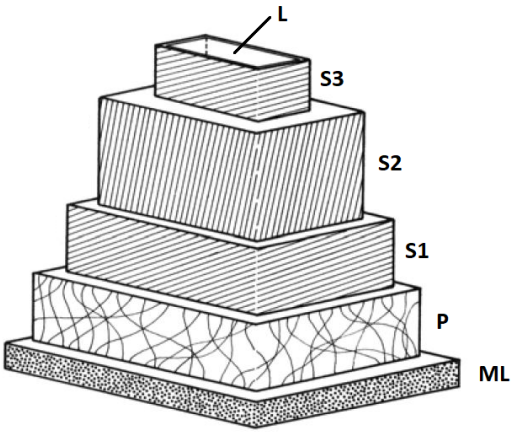

Fig. 4: Sketch of a cellulose fiber wall - adapted from [10]
ML ... middle lamella, P ... primary wall, S ... secondary wall layers, L ... lumen

2.1.3 Fiber to Fiber Bonds

Since paper consists of a network of bonded cellulose fibers, understanding the bonding mechanisms as well as having a full picture of the bond interfaces is of utmost importance.

According to Page [3], the tensile strength T of paper depends on the strength of the individual fibers F and the strength of the individual FtF-bonds B as follows:

$$\frac{1}{T} = \frac{1}{F} + \frac{1}{B} \tag{1}$$

Page [3] further derived a refined equation based on theoretical considerations and empirical studies, which is known as the "Page equation":

$$\frac{1}{T_{\mathrm{B}}} = \frac{9}{8Z} + \frac{12A\rho g}{bPl(RBA)}, \tag{2}$$

where T_{B} is the tensile strength of paper expressed as breaking length, Z is the breaking length of single fibers, A is the mean fiber cross-sectional area, ρ is the density of the fibers, g is the gravitational acceleration, b is the shear strength per unit bonded area, P is the mean perimeter of the fiber cross-sections, l is the mean length of the fibers and RBA is the relative bonded area [3]. When inspecting eq. (1) and eq. (2) it becomes obvious that the fiber strength and the bond between individual fibers have to be investigated to fully understand the strength of paper. FtF-bonds have not been completely understood to this day, since there are various bonding mechanisms involved in bonding of cellulose fibers. In this Master's Thesis similar definitions as in the work of Sormunen [15] are chosen, regarding FtF-bonds. An FtF-bond is the intersection of two cellulose fibers that are bonded to each other. The optically overlapping area between the two fibers is defined as the intersection area A_{I} (see fig. (5) blue area) and the bonded area is the area in which the two fibers are in molecular contact. Since measuring a whole FtF-bond with a resolution in the molecular regime is yet not possible, a further quantity, namely the relative contact area (RCA), is introduced. The RCA is the subsection of the intersection area that is measured to be in contact A_{C}, regarding the achieved experimental resolution, divided by the intersection area and reads

$$RCA = \frac{A_{\mathrm{C}}}{A_{\mathrm{I}}}. \tag{3}$$

In comparison, the RBA is the fraction of the fiber surface that is bonded, regarding a whole sheet of paper [3].

The basic mechanisms responsible for fiber bonding are hydrogen bonding, van der Waals forces, Coulomb forces, capillary forces, mechanical interlocking and interdiffusion [17]. In the process of papermaking wet fibers are dried, thus establishing molecular contact due to capillary forces pressing the fibers together in the first place [18] [16] (see fig. (5)). Since cellulose fibers are known to have a smooth and soft surface under wet conditions [19], the degree of molecular contact should be high. Wet cellulose fibers are swollen and even form a hydrogel layer on their surface [20], enabling interdiffusion. Interdiffusion is the diffusion of cellulose molecules from one fiber to another, thus increasing the contact area and enhancing the bond strength. After drying, pulp fibers still contain about 10 % water (by mass) at ambient conditions, thus capillary bridges may be formed that contribute to the bonding of the two fibers [17]. As discussed in section 2.1.2, cellulose molecules have a significant amount of hydroxyl groups, which tend to form hydrogen bonds. Hence, hydrogen bonds do also play a role in FtF-bonds. If the two cellulose fiber surfaces are together close enough, van der Waals forces, i.e., attractive electric dipole moments, start

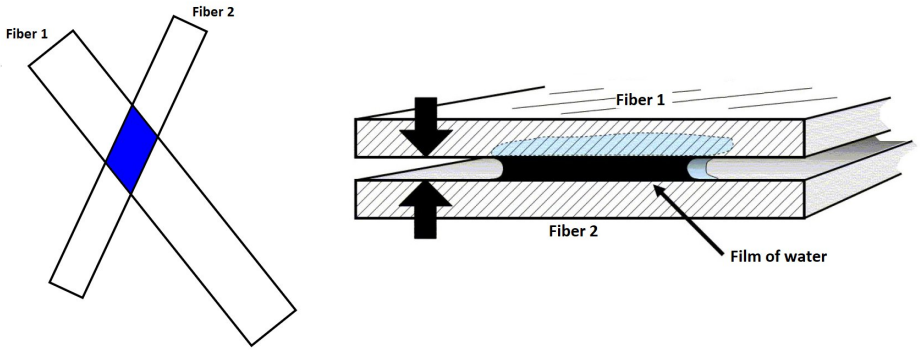

Fig. 5: Sketch of two cellulose fibers bonding together due to capillary forces - adapted from [16]
Left: Two overlapping cellulose fibers, forming an FtF-bond in the intersection area which is marked in blue. Right: Sketch of a film of water between two cellulose fibers, leading to an attractive force.

to play a role. During pulping, negative charges of acid functions of hemicelluloses can dissociate and interact with anions from the water of the fiber suspension [17], giving rise to Coulomb forces. Mechanical interlocking arises from the fibrillar structure of the cellulose fibers. Microfibrils sticking out of the surface can be entangled during bond formation which leads to an increase in bond strength [17].

Hirn and Schennach [17] estimated the specific binding energies of each of the aforementioned bonding mechanisms. One of their main findings is that hydrogen bonding, which was believed to play a major role in bond strength, is of less importance than other mechanisms (see fig. (6)). According to their calculations, the highest contributions stem from van der Waals forces and Coulomb forces, though with a big error bar for Coulomb forces. Capillary forces show the lowest contribution, as they can only occur in regions that are not in molecular contact and these regions were assumed to make up only about 10 % of the intersection area of the FtF-bond. For the calculation, the upper and lower limit of molecular contact was 100 % and 30 % of the intersection area, respectively. The maximum contribution of interdiffusion was assumed to be a doubling of the area in molecular contact.

Intermolecular bonding mechanisms such as van der Waals forces, hydrogen bonding and Coulomb forces only play a role if molecular contact between the fibers is established, i.e., the fibers are within a distance smaller than approximately 30 nm [17]. Thus, the area in molecular contact contributes significantly to bond strength and needs to be quantified precisely. Fig. (7) illustrates the importance of high-resolution measurements of the intersection region between two cellulose fibers. Regions that seem to be in molecular contact may turn out not to be in contact when taking a look under larger magnification, i.e., better resolution. Several attempts have been made by various groups to determine the area in molecular contact accurately by using different methods. A comprehensive review of various methods to measure the contact area of FtF-bonds is given in a report by Hirn et al. [21]. In the following some characterization methods are briefly introduced.

Adsorption based methods rely on the idea that a dye or a gas is adsorbed on the surface of the FtF-bond in non-contact regions, thus making regions in molecular contact distin-

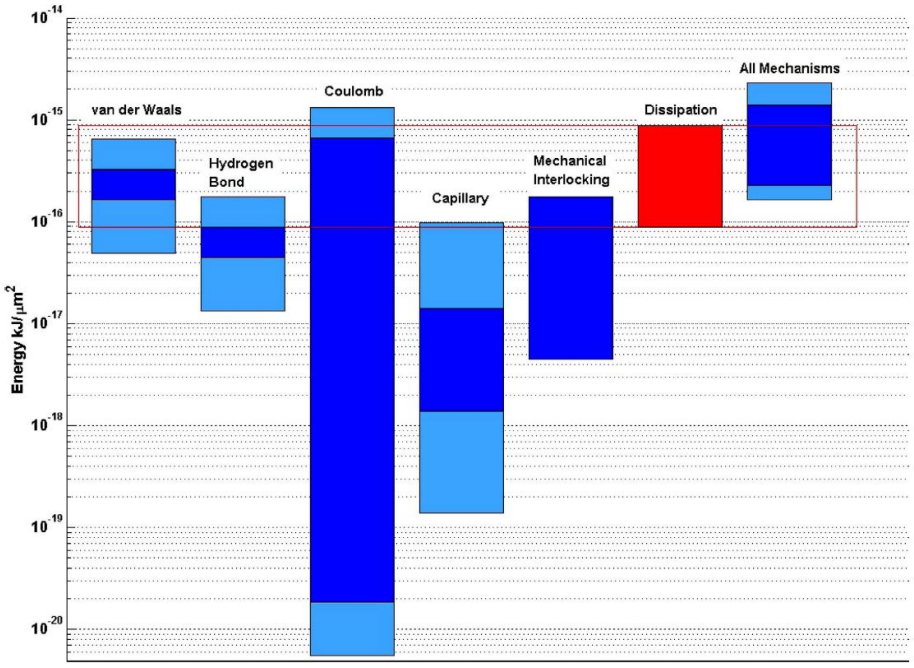

Fig. 6: Binding energies of different mechanisms in FtF-bonds - from [17]
The estimated contributions without interdiffusion and a fixed area of molecular contact are depicted in dark blue. The uncertainties are increased, considering an upper and lower limit for interdiffusion and the area in molecular contact (light blue). The dissipated energy from measurements of FtF-bonds is displayed in red.

guishable from non-contact regions when opening the bond. The problem though, is that isolated non-contact regions are not accessible to the dye or the gas. These methods were performed, e.g., by Haselton et al. [23] using nitrogen gas and by Torgnysdotter et al. [24] using a dye.
Another method is Förster resonance energy transfer (FRET), which is capable of determining the degree of close contact ($1 - 10\,\text{nm}$) between two surfaces. It makes use of two different fluorescent dyes, the so-called donor dye and the acceptor dye. The two fibers of an FtF-bond are stained with one of the dyes, respectively. After excitation of a donor molecule with light of a specific wavelength, the energy is transferred to acceptor molecules non-radiative, if the distance between the donor and the acceptor molecule is close enough. Thus, a so-called FRET-signal can be measured and the contact area in the nanometer regime can be deduced. Urstöger et al. [25] applied this method to pulp fibers, though they could not measure a significant FRET-signal. However, they showed that with their system, a quantification of the contact area between two surfaces in the nanometer regime is in principle possible, if the dyeing method is changed from bulk dyeing to surface dyeing.
Sormunen et al. [7] imaged 26 FtF-bonds formed from softwood kraft pulp fibers, using laboratory-based X-ray nanotomography. The technique uses X-rays passing through the sample. The sample is scanned from various angles and the attenuation of the X-ray intensity is recorded. From these measurements, computed tomography is performed to reconstruct a 3D representation of the sample. The mean value of the RCA turned out to be about 58 %, though with wide variation from approximately 6 to 85 %. The recon-

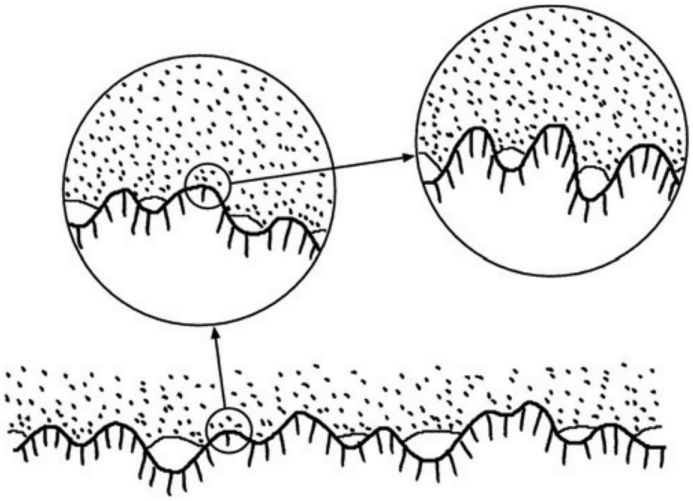

Fig. 7: Sketch of two rough cellulose fiber surfaces partially in contact - from [22]
With increasing magnification or better resolution, gaps may be resolved in regions that previously seemed to be in contact.

structed pixel size was 65 nm and the resolution of the device was determined empirically to be 128 nm. Nevertheless, it has to be mentioned that this does not necessarily correspond to the resolution of the reconstructions, which could be worse. Additionally, the reconstructions showed a rather poor signal to noise ratio and contrast.
Light optical methods are not feasible to detect non-contact regions with gaps smaller than half the wavelength of light due to physical limitations. Though, these methods are important to investigate the intersection area on larger length scales. Kappel et al. utilized polarization microscopy [6] and microtome serial sectioning [5] to measure FtF-bonds formed from beaten and unbeaten unbleached softwood kraft pulp fibers. They measured 73 FtF-bonds from unbeaten pulp and 68 FtF-bonds from beaten pulp. The average RCA of FtF-bonds formed from unbeaten and beaten fibers turned out to be 86 % and 98 %, respectively [26]. However, the resolution in this study is only in the micrometer regime, thus the RCA is higher compared to the previously mentioned study from Sormunen et al.
A further technique to determine the RCA is confocal laser scanning microscopy (CLSM) and was applied to FtF-bonds formed from lignocellulose fibers by Li et al. [4] in 2018. CLSM makes use of optical sectioning with a laser light source rather than mechanical sectioning by a microtome. Several 2D images are collected, thus allowing for a 3D reconstruction. In total, 52 FtF-bonds were imaged, resulting in an average RCA of about 58 %. The achieved resolution was about $0.15 - 0.4\,\mu m$ in x/y-direction and about $0.8\,\mu m$ in z-direction.

However, none of these methods can resolve FtF-bonds with a resolution smaller than 30 nm, where intermolecular bonding mechanisms start to play a role. Hence, new techniques have to be explored or older ones refined to improve resolution and contrast.

2.2 Ptychographic X-ray Computed Tomography

2.2.1 The Phase Problem

For this section, mainly the PhD thesis of Dierolf [27] served as a basis.
If an electromagnetic wave, in our case X-rays, passes through a medium, the complex refractive index $n(\vec{r}, \lambda)$ has to be taken into account. The complex refractive index is a function of the spatial coordinates $\vec{r} = (x, y, z)$ and the wavelength λ of the X-rays and reads:

$$n(\vec{r}, \lambda) = 1 - \delta(\vec{r}, \lambda) + i\beta(\vec{r}, \lambda) \tag{4}$$

δ is linked to the electron density $n_\mathrm{e}(\vec{r})$ and can be expressed as

$$\delta(\vec{r}, \lambda) = \frac{r_\mathrm{e}\lambda^2}{2\pi} n_\mathrm{e}(\vec{r}), \tag{5}$$

if the radiation energy is higher than the binding energy of core electrons, with the classical electron radius $r_\mathrm{e} \approx 2.818 \cdot 10^{-15}\,\mathrm{m}$.

β is linked to the photoelectric linear attenuation coefficient $\mu(\vec{r})$ and is defined as

$$\beta(\vec{r}, \lambda) = \frac{\lambda}{4\pi}\mu(\vec{r}). \tag{6}$$

Considering an incoming wave $\psi_0(x, y)$ propagating along the z-axis which passes through an object with some refractive index $n(\vec{r})$, the wave $\psi(x, y)$ exiting the object, called exit wave, can be described as

$$\psi(x, y) = O(x, y) \cdot \psi_0(x, y), \tag{7}$$

for waves that are sufficiently constant over the thickness of the object.
$O(x, y)$ is the object transmission function along the propagation direction and consists of an absorbing part $T(x, y)$ and a phase shifting part $\Phi(x, y)$.

$$O(x, y) = T(x, y) \cdot e^{i\Phi(x,y)} \tag{8}$$

$$T(x, y) = e^{-\frac{2\pi}{\lambda}\int \beta(\vec{r})\mathrm{d}z} \tag{9}$$

$$\Phi(x, y) = -\frac{2\pi}{\lambda}\int \delta(\vec{r})\mathrm{d}z \tag{10}$$

Hence, the amplitude of the wave gets attenuated and the phase of the wave gets shifted. By using a detector, the intensity I of the wave can be recorded. When considering an electromagnetic wave with the complex scalar amplitudes E_0 and H_0, the intensity can be expressed as the time average of the Poynting vector $\vec{S}$.

$$I = \left\langle \left| \vec{S} \right| \right\rangle_t = \frac{1}{2} E_0 H_0^* = \frac{|E_0|^2}{2c\mu_0} \tag{11}$$

c ... speed of light in the medium
$\mu_0 = 4\pi \cdot 10^{-7}\,\mathrm{V\,s\,A^{-1}\,m^{-1}}$ ... magnetic constant [28]

Consequently, in a measurement, the phases of the electromagnetic wave are lost. This problem is known as the phase problem and one way to solve it and retrieve the phases is ptychography.

2.2.2 Ptychography

Ptychographic X-ray computed tomography (PXCT) is a type of coherent diffractive imaging (CDI) that utilizes coherent X-rays from a synchrotron source to retrieve the 3D phase information of the X-ray wave-field in the object plane. The term ptychography is deduced from the Greek words for "fold" ($\pi\tau\upsilon\xi$) and "writing/drawing" ($\gamma\rho\alpha\phi\eta$) and was first introduced by Hegerl and Hoppe in 1970 [29]. The concept of ptychography is based on the work from Hoppe in 1969 [30], who proposed a direct method of phase retrieval for thin crystalline samples with a transmission electron microscope operated in diffraction mode. He showed that phase retrieval is possible if the Bragg peaks of the diffraction patterns do interfere. The idea is based on using a finite coherent illumination with a size in the regime of one unit cell. Consequently, the diffraction peaks are convolved with the Fourier transform of the illumination and the patterns of adjacent Bragg peaks do interfere. This allows for the calculation of relative phases. Due to the convolution step, ptychography can be translated as "convolution imaging" [27].
Later, ptychography was extended to non crystalline objects as an iterative phase retrieval algorithm. A general definition of ptychography was given by Rodenburg in 2008 [31] as follows:

1. In the experimental setup a transmission object is illuminated by a localized field of radiation. This results in scattering of the radiation and provides a diffraction pattern. The intensity of the scattered radiation, i.e., the diffraction pattern, is recorded (usually, but not necessarily in the far field).
2. At least two diffraction patterns are recorded for either shifted positions of the illumination with respect to the object, or a changed structure of the illumination.
3. A calculation including at least two of these diffraction patterns is performed to retrieve all phases in diffraction plane, or, equivalently, the exit wave of the object in real space.
4. A nonperiodic object of, theoretically, unlimited size can be imaged by processing a large number of diffraction patterns, if the illumination is only changed by lateral shifts.

In the experiments presented in this Master's Thesis, the change of the illumination was only performed by lateral shifts of the sample with respect to a fixed illumination. Thus, a ptychographic data set for this Thesis is defined as follows [27]:

Diffraction patterns $I_i(q_x, q_y)$, obtained from a fixed, localized illumination, called probe $P(x, y)$, impinging on an object, are recorded in the far field. Such diffraction patterns are recorded for several overlapping spots, at positions $\vec{r_i} = (x_i, y_i)$, of the probe on the object. The probe is represented by the full wave field incident on the object and the

object is represented by the complex object transmission function $O(x, y)$, as stated in eq. (8).

$$I_i(\vec{q}) = |\mathcal{F}[P(\vec{r} - \vec{r}_i) \cdot O(\vec{r})]|^2 \tag{12}$$

$\vec{q}$ ... reciprocal space coordinates

Consequently, the goal of ptychography is to reconstruct the object transmission function $O(\vec{r})$ numerically for all scanning points i, such that it satisfies eq. (12).

2.2.3 Coherence

In CDI, the coherence of the illuminating waves is required to achieve interference of the diffraction patterns. There is spatial and temporal coherence, which can be described by the so called coherence lengths, i.e., the length scales for which the degree of coherence is high.

Temporal coherence is usually characterized by the longitudinal coherence length ξ_l. It can be derived when considering two wave fronts with the wavelength λ and $\lambda + \Delta\lambda$, simultaneously departing from the same point. After the distance ξ_l, the two waves are in antiphase, i.e., their phase difference is π (see fig. (8)). Consequently, for N oscillations of the first wave within the distance ξ_l, the second wave must have made $N - \frac{1}{2}$ oscillations. This results in the condition $N\lambda = (N - \frac{1}{2})(\lambda + \Delta\lambda)$. Solving this equation for N and considering $\xi_\mathrm{l} = N\lambda$ results in:

$$\xi_\mathrm{l} \approx \frac{\lambda^2}{2\Delta\lambda} \tag{13}$$

Hence, the longitudinal coherence length depends on the spectral bandwidth of the radiation, which can be tuned by Si(111) monochromators. Typically, the longitudinal coherence length for ptychography experiments is in the sub-µm regime. [32]

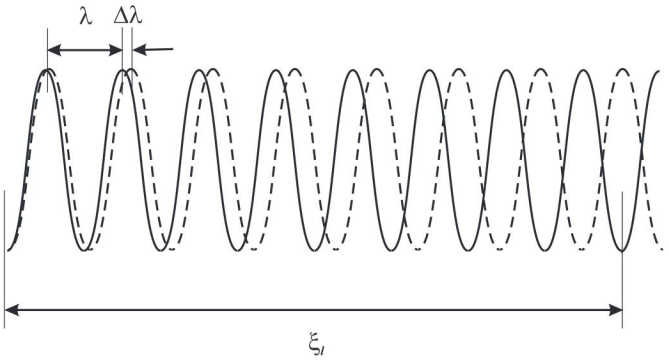

Fig. 8: Sketch of two propagating waves with wavelength λ and $\lambda + \Delta\lambda$ - from [32]
The longitudinal coherence length ξ_l is the distance over which the two waves develop a phase shift of π

Spatial coherence is usually described by the transverse coherence length ξ_t and can be explained by a Young's double slit experiment, as sketched in fig. (9). Two slits with separation d are placed at a distance R from a 1D incoherent light source of height w. The diffraction pattern is visualized on a screen at a distance L behind the double slit. ξ_t is then defined as the slit distance d for which the interference fringes vanish, i.e., the minima

produced by an infinitesimally small source element located in the middle of the extended light source coincide with the maxima produced by an emitting element at the border of the source. The interference fringes produced by the central point source appear at diffraction angles $\alpha = \frac{m\lambda}{d}$, with $m = 0, \pm1, \pm2, ...$ for the maxima and $m = \pm\frac{1}{2}, \pm\frac{3}{2}, \pm\frac{5}{2}, ...$ for the minima, in the small angle approximation. For the emitting element at the border of the extended source, the fringes are shifted by an angle $\alpha_\mathrm{s} = \frac{w}{2R}$. Hence, the maxima and minima of these patterns coincide if $\frac{\lambda}{2d} = \frac{w}{2R}$, which yields the transverse coherence length, when solving for d.

$$\xi_\mathrm{t} = \frac{\lambda R}{w} \tag{14}$$

Since light sources often have a 2D extent, there are two different transverse coherence lengths for both directions (vertically and horizontally).

$$\begin{aligned} \xi_\mathrm{h} &= \frac{\lambda R}{w_\mathrm{h}} \\ \xi_\mathrm{v} &= \frac{\lambda R}{w_\mathrm{v}} \end{aligned} \tag{15}$$

Furthermore, realistic synchrotron sources tend to have a Gaussian intensity distribution. Thus, the sigma widths (σ_h and σ_v) of the Gaussian source are used instead of the standard width w, which leads to:

$$\begin{aligned} \xi_\mathrm{h} &= \frac{\lambda R}{2\pi\sigma_\mathrm{h}} \\ \xi_\mathrm{v} &= \frac{\lambda R}{2\pi\sigma_\mathrm{v}} \end{aligned} \tag{16}$$

Typical values for the transverse coherence lengths in modern synchrotrons are $\xi_\mathrm{v} \approx 25 - 100\,\mu\mathrm{m}$ and $\xi_\mathrm{h} \approx 3 - 10\,\mu\mathrm{m}$ for typical values of $R = 40\,\mathrm{m}$ and $\lambda = 0.1\,\mathrm{nm}$. [32]

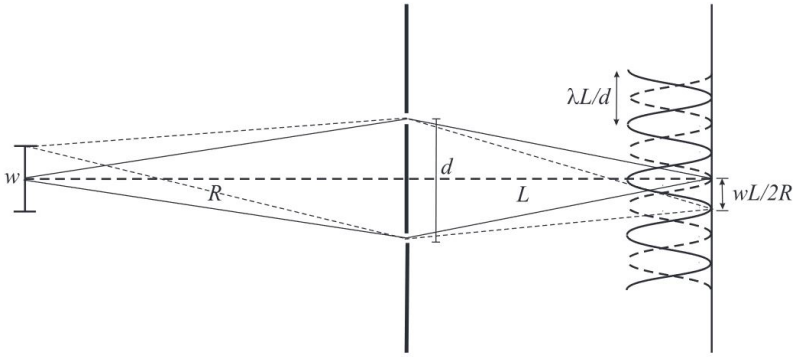

Fig. 9: Sketch of Young's double slit experiment - from [32]
The diffraction patterns are shown for a central point source (solid line) and for a point source at the edge of the extended source (dashed line). The transverse coherence length ξ_t is the slit separation d for which the two patterns are in antiphase, like shown.

2.2.4 Iterative Phase and Probe Retrieval

An early approach to solve a ptychographic problem is the "Wigner deconvolution" [33], where simultaneous reconstruction of the object transmission function and the probe

function were attempted. In this formalism the probe positions $\vec{r}_i$ have to be on a grid with a spacing as small as the aimed resolution, thus being inefficient for many applications. Another algorithm is the ptychographic iterative engine (PIE) [34], which cycles through the data set iteratively to reconstruct the object transmission function. The problem with this algorithm is the lack of simultaneous probe retrieval. Thus, the probe function has to be known a priori, which is disadvantageous, as the illuminating radiation can undergo fluctuations during the experiment, leading to errors in the reconstruction. In 2009 Thibault et al. [35] reported the implementation of an iterative algorithm, based on difference map (DM) [36], with simultaneous retrieval of both the object transmission function and the probe function, without the problems of the aforementioned methods. This algorithm was used for the reconstructions presented in this Master's Thesis and is explained in this section, based on the article from Thibault et al. [35]. The algorithm is based on reformulating the ptychographic problem, as introduced in eq. (12), as the search for the intersection point between two constraint sets. For this, so-called exit waves ψ_i (views on the sample) were introduced. The two constraint sets are the Fourier constraint

$$I_i(\vec{q}) = |\mathcal{F}[\psi_i(\vec{r})]|^2, \tag{17}$$

and the overlap constraint

$$\psi_i(\vec{r}) = P(\vec{r} - \vec{r}_i) \cdot O(\vec{r}). \tag{18}$$

The Fourier constraint contains the measured intensities whereas the overlap constraint implies that each view can be expressed as a multiplication of the probe and the object transmission function. The iterations then take place on the state vector $\vec{\Psi} = (\psi_1(\vec{r}), \psi_2(\vec{r}), ..., \psi_{\mathrm{N}}(\vec{r}))$ embedded in the search space. This search space is the direct product of the spaces of all the individual views. The DM algorithm requires a projection of the state vector onto the constraint sets and a distance minimization between the current state and the projected state $\left\|\vec{\Psi} - \Pi(\vec{\Psi})\right\|^2$.

The projection concerning the Fourier constraint Π_{F} is given by applying the Fourier projection p_{F} on each individual view

$$\Pi_{\mathrm{F}}(\vec{\Psi}) : \psi_i \rightarrow \psi_i^{\mathrm{F}} = p_{\mathrm{F}}(\psi_i). \tag{19}$$

The Fourier projection p_{F} replaces the current amplitudes with the measured intensity $\sqrt{I_i}$ while keeping the phases

$$p_{\mathrm{F}} : \mathcal{F}[\psi_i(\vec{r})] \rightarrow \mathcal{F}[\psi_i(\vec{r})]^{\mathrm{F}} = \sqrt{I_i(\vec{q})} \frac{\mathcal{F}[\psi_i(\vec{r})]}{|\mathcal{F}[\psi_i(\vec{r})]|} \tag{20}$$

The projection concerning the overlap constraint can be expressed as

$$\Pi_{\mathrm{O}}(\vec{\Psi}) : \psi_i \rightarrow \psi_i^{\mathrm{O}} = \hat{P}(\vec{r} - \vec{r}_i) \cdot \hat{O}(\vec{r}), \tag{21}$$

and the overlap projection can be computed from distance minimization of $\left\|\vec{\Psi} - \Pi_{\mathrm{O}}(\vec{\Psi})\right\|^2$. To do so, the functions $\hat{O}$ and $\hat{P}$ have to be found that minimize

$$\left\|\vec{\Psi} - \Pi_{\mathrm{O}}(\vec{\Psi})\right\|^2 = \sum_i \sum_{\vec{r}} \left|\psi_i(\vec{r}) - \hat{P}(\vec{r} - \vec{r}_i) \cdot \hat{O}(\vec{r})\right|^2. \tag{22}$$

A numerical approach for the minimization of eq. (22) has to be performed, as an analytical minimization cannot be carried out. Setting the derivative of eq. (22) to zero yields the solution as a system of coupled equations

$$\hat{O}(\vec{r}) = \frac{\sum_i \hat{P}^*(\vec{r} - \vec{r}_i) \cdot \psi_i(\vec{r})}{\sum_i \left|\hat{P}(\vec{r} - \vec{r}_i)\right|^2} \tag{23}$$

$$\hat{P}(\vec{r}) = \frac{\sum_i \hat{O}^*(\vec{r} + \vec{r}_i) \cdot \psi_i(\vec{r} + \vec{r}_i)}{\sum_i \left|\hat{P}(\vec{r} + \vec{r}_i)\right|^2}. \tag{24}$$

For the retrieval of both $\hat{P}$ and $\hat{O}$, eq. (23) and eq.(24) have to be solved simultaneously. As there is no analytical solution, the equations have to be applied iteratively in turns. As a starting point, a rough model of the probe $\hat{P}$ is used. Subsequently, for every new iteration, $\hat{O}$ and $\hat{P}$ are taken from the previous iteration, as initial guesses. With standard parameters of the DM algorithm [36], the iterations for the state vector have a form of

$$\vec{\Psi}_{n+1} = \vec{\Psi}_n + \Pi_\mathrm{F}[2\Pi_\mathrm{O}(\vec{\Psi}_n) - \vec{\Psi}_n] - \Pi_\mathrm{O}(\vec{\Psi}_n) \tag{25}$$

and

$$\psi_i^{n+1}(\vec{r}) = \psi_i^n(\vec{r}) + p_\mathrm{F}[2\hat{P}(\vec{r} - \vec{r}_i) \cdot \hat{O}(\vec{r}) - \psi_i^n(\vec{r})] - \hat{P}(\vec{r} - \vec{r}_i) \cdot \hat{O}(\vec{r}) \tag{26}$$

for the individual views. Within these iterations, $\hat{O}$ and $\hat{P}$ are refined iteratively, based on eq. (23) and eq. (24) as mentioned above. The initial guess for the state vector $\vec{\Psi}_0$ can just be an array of random numbers, or setting the individual views to the initial guess for the probe. Convergence of this algorithm has been verified in multiple situations [37]. Iterations of eq. (25) take place until reaching a fixed point where the state vectors do not change any more, i.e., $\vec{\Psi}_{n+1} = \vec{\Psi}_n$. The solutions of the phase retrieval problem are then the second or third term of eq. (25), which are equivalent if converged. The third term $\Pi_\mathrm{O}(\vec{\Psi}_n)$ contains $\hat{P}$ and $\hat{O}$, which are the quantities of interest and are computed within the iterations, so no extra effort has to be done to calculate them. Monitoring of convergence is done with the DM error

$$\epsilon_{n+1} = \left\| \vec{\Psi}_{n+1} - \vec{\Psi}_n \right\|, \tag{27}$$

which would be zero in an ideal case, but in practice is not, due to experimental limitations and noise.

However, there are some problems that have to be accounted for, as the solution is not necessarily unique. Firstly, there may be constant phase terms, which means that the retrieved phases can be multiplied with an arbitrary phase factor $e^{i\phi}$ while still being consistent with the two constraints. Secondly, linear phase terms do occur, as, according to the Fourier shift theorem, a shift in Fourier space comes with a multiplication with a linear phase in real space. These constant and linear phase terms can be removed by measuring a region outside the sample as a reference. The phase for this region should be zero, hence can be used for calibration (for more details please refer to [38]). Thirdly, there is the problem of phase wrapping, as the reconstructed phase is only known modulo 2π. So-called phase unwrapping can be performed for one ptyhcographic reconstruction, or more efficiently in the tomography step of many 2D ptychographic reconstructions,

as explained in [38]. And finally, the so-called "raster grid pathology" has to be taken into account. This means that, if $O(\vec{r})$ and $P(\vec{r})$ are solutions to the ptychographic problem, also $O'(\vec{r}) = f(\vec{r}) \cdot O(\vec{r})$ and $P'(\vec{r}) = f^{-1}(\vec{r}) \cdot P(\vec{r})$, with $f(\vec{r}) = f(\vec{r} - \vec{r}_i), \forall \vec{r}_i$, are solutions. In an article from Huang et al. [39] in 2014, it has been shown that the raster grid pathology can be accounted for, by avoiding the use of scan points lying on a regular 2D lattice, but using scan points following a Fermat spiral instead.
Furthermore, the ptychographic reconstructions can be refined by maximum likelihood (ML) principles, introduced by Thibault and Guizar-Sicairos in 2012 [40] for ptychography. The idea is to include statistical models into the ptychographic reconstruction process to account for statistical noise.

2.2.5 Computed Tomography

In order to obtain a 3D representation of the sample, it has to be imaged from various angles between 0° and 180° and ptychographic reconstructions have to be made for each angle. The ptychographic reconstruction from the measurement from a certain angle is called projection. All the measured projections can be used to compute a 3D tomogram via computed tomography (CT). For this, all the projections have to be aligned to each other. Usually, for the alignment, a method based on the tracking of marker particles is performed. Nevertheless, for the reconstructions in this Master's Thesis a different approach, as described in an article from Guizar-Sicairos et al. [38], was used. The alignment in the horizontal x-direction is based on a center of mass computation of a phase-unwrapped region. Here, mass means the integral of the projected phase. For the phase unwrapping, a well-behaved region in the projection is used. In such a well-behaved region no phase residues or only a few are present, making the unwrapping easier. These residues are points in the phase that lead to inconsistencies in the unwrapped phase, thus making the result dependent on the selected unwrapping path. The alignment of the projections in the vertical y-direction is based on a method called vertical mass fluctuation (VMF), which iteratively maximizes the correlation of vertical variations in the mass of the specimen. The vertical mass distribution $M_\theta(y)$ can be obtained by integrating the phase along the horizontal x-direction for each projection

$$M_\theta(y) = \int \Phi(x, y, \theta) \mathrm{d}x = -\frac{2\pi}{\lambda} \iint \delta(x \cos\theta - z \sin\theta, y, z \cos\theta + x \sin\theta) \mathrm{d}x \mathrm{d}z, \qquad (28)$$

where θ is the rotation angle between the specimen and the X-ray beam. In an ideal case, the mass distribution would be the same for each projection. $M_\theta(y)$ is computed for all projections in the selected area and Legendre polynomial terms along the vertical y-direction are removed with a least squares fit. This results in a function $\varphi_\theta(y)$ that indicates small sample fluctuations and provides a visual representation of the sample misalignment. The alignment function $\varphi_\theta(y)$, before alignment, is shown in fig. (10a) exemplary for a measurement of a cellulose sample. The position estimate for the $(n+1)$-th iteration for the alignment is then calculated by minimizing the squared error E^2 with respect to the average $\langle \varphi_\theta(y) \rangle$ taken over rotation angle

$$E^2 = \sum_{y,\theta} [\varphi(y - \Delta y_\theta^{(n+1)}, \theta) - \langle \varphi(y - \Delta y_\theta^{(n)}, \theta) \rangle]^2. \qquad (29)$$

At first, the calculation is done with single-pixel precision alternating within the iterations between x and y alignment. Subsequently, an iterative subpixel refinement is performed,

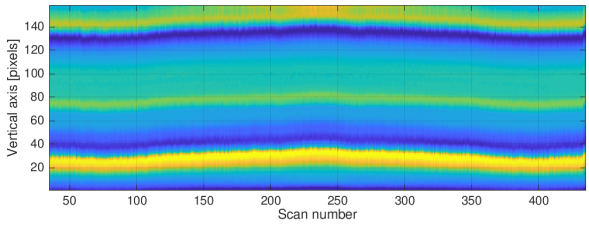

(a) Alignment function $\varphi_\theta(y)$ before alignment

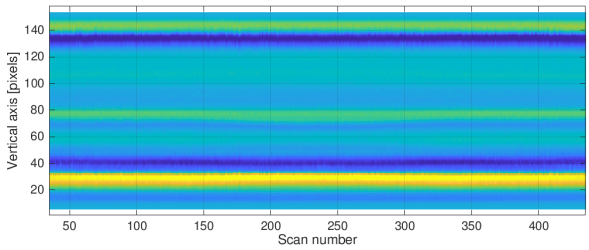

(b) Alignment function $\varphi_\theta(y)$ after alignment

Fig. 10: Alignment functions of measured projections of a cellulose sample

where the contribution to E^2 is calculated for each projection at three subpixel displacement points. Then, a parabola is fitted and the best alignment is set as minimum point. The alignment function $\varphi_\theta(y)$ after the alignment is displayed in fig. (10b), for the same sample as mentioned before.

After the alignment of projections, CT is performed from the derivative of the wrapped phases, following a process as described in the previously mentioned article by Guizar-Sicairos et al. [38]. The method is based on filtered back-projection (FBP), which is a well-known algorithm used in CT. When FBP is applied to phase projections, the result is proportional to the δ-part of the refractive index

$$-\frac{2\pi\Delta}{\lambda}\delta(\vec{r}) = \int_0^\pi \mathcal{F}_u^{-1}[|u|\mathcal{F}_{x'}[\Phi(x', y, \theta)]]\mathrm{d}\theta, \tag{30}$$

where Δ is the voxel side length, $|u|$ is the Fourier domain filter applied to the projections, $\mathcal{F}_x$ is a 1D Fourier transform from x to u coordinates and $\mathcal{F}_u^{-1}$ is the inverse Fourier transform from u to x coordinates. Though, this equation should not be used as it produces strong artifacts if the phase is wrapped. Thus, a modified Fourier filter has been introduced [38], allowing for tomographic reconstruction from the derivative of the phase

$$-\frac{2\pi\Delta}{\lambda}\delta(\vec{r}) = \int_0^\pi \mathcal{F}_u^{-1}\left[\frac{1}{2\pi i \cdot \mathrm{sgn}(u)}\mathcal{F}_x\left[\frac{\partial\Phi(x, y, \theta)}{\partial x}\right]\right]\mathrm{d}\theta. \tag{31}$$

Eq. (31) can easily be obtained from eq. (30) by using the Fourier theorem for the Fourier transform of derivatives $\mathcal{F}_x[\frac{\partial\Phi}{\partial x}] = 2\pi i\mathcal{F}_x[\Phi]$. Thus, a tomogram can be computed directly from the derivative of the phase. In case of wrapped phases, the derivative can be computed numerically by

$$\frac{\partial\Phi(x, y, \theta)}{\partial x} = \frac{1}{h}(g(x + h/2, y, \theta)g^*(x - h/2, y, \theta)), \tag{32}$$

with the step h for the numerical differentiation and $g(x, y, \theta) = e^{i\Phi(x,y,\theta)}$ to avoid interpolating artifacts. Eq. (32) maps the phase to the unit circle, and thus wrapping discontinuities vanish. The processing steps are depicted in fig. (11).

The quality of the resulting tomogram may be improved by adopting the Fourier domain filter. The ramp filter $|u|$ in eq. (30), also called Ram-Lak filter, may be adopted by multiplication with a window function to account for noise. With the Ram-Lak filter, the frequency components are weighted proportional to the absolute value of their frequency, thus making the reconstruction sensitive to high-frequency noise. Multiplication with a window function, f.e. a Hann window, reduces the weight of high frequencies and may thus be beneficial.

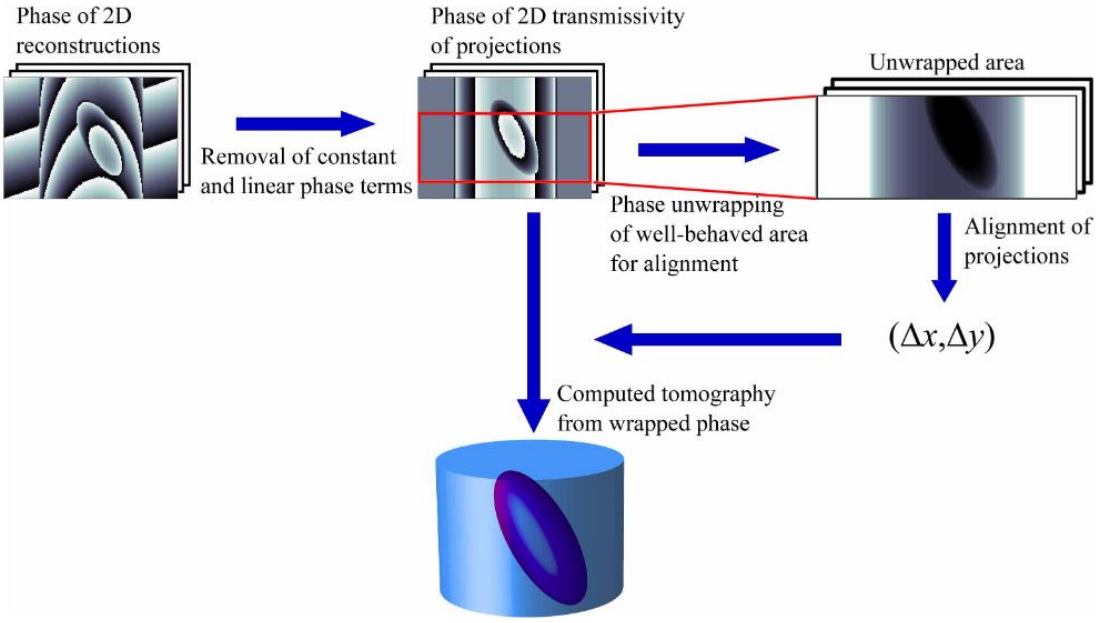

Fig. 11: Sketch of processing steps for computed tomography - from [38]
After the ptychographic reconstruction, linear and constant phase terms are removed. Subsequently, a well-behaved area is chosen for phase unwrapping and alignment of the projections. Then, the aligned, wrapped projections are used for CT to obtain a 3D tomogram of the refractive index of the sample.

2.3 Image Segmentation

The result of the PXCT measurements are grey-scale 3D image stacks, with every pixel having a value proportional to the refractive index of the measured volume. In order to achieve a quantitative analysis of the region of interest, image segmentation has to be performed. Image segmentation divides the image into different classes, such that the area of interest can be extracted and analyzed more easily. The segmentation could be done manually, but the 3D image stack consisting of a large number of 2D cross-sections, makes this an inefficient task. Thus, automated image segmentation algorithms were used for this Master's Thesis. For some tasks, threshold segmentation was performed and for others, a machine learning approach, called *Trainable Weka Segmentation* [41] was used. For the threshold segmentation, Otsu's method [42], as well as simply choosing a manual threshold

by visual inspection, was performed. In some cases, the simple threshold segmentation did not result in a sufficient segmentation, thus the more sophisticated machine learning approach was used.

2.3.1 Otsu's Method

Otsu's method is a threshold segmentation method, introduced by Otsu in 1979 [42], that is only based on the gray-level histogram without other a priori knowledge. The calculation includes a measure for the "goodness" of the threshold and assigns every pixel of a given image to either of two classes, here called C_0 and C_1. For a histogram with L bins, each bin containing n_i pixels and a total number of N pixels, the probability of class occurrence is given by

$$\omega_0 = \sum_{i=1}^{k} p_i = \omega(k) \tag{33}$$

$$\omega_1 = \sum_{i=k+1}^{L} p_i = 1 - \omega(k), \tag{34}$$

where the histogram is considered as a probability distribution, i.e., $p_i = n_i/N$ and $p_i \geq 0, \sum_{i=1}^{L} p_i = 1$, and k is the threshold level, dividing the set of bins into $[1, 2, ..., k]$ for class C_0 and $[k+1, k+2, ..., L]$ for class C_1. The class mean levels are given by

$$\mu_0 = \sum_{i=1}^{k} \frac{ip_i}{\omega_0} = \frac{\mu(k)}{\omega(k)} \tag{35}$$

$$\mu_1 = \sum_{i=k+1}^{L} \frac{ip_i}{\omega_1} = \frac{\mu_\mathrm{T} - \mu(k)}{1 - \omega(k)}, \tag{36}$$

where $\omega(k) = \sum_{i=1}^{k} p_i$ is the zeroth- and $\mu(k) = \sum_{i=1}^{k} ip_i$ is the first cumulative moment of the histogram up to level k and $\mu_\mathrm{T} = \mu(L)$ is the total mean level of the original image. The "goodness" of the threshold is given by

$$\eta(k) = \frac{\sigma_\mathrm{B}^2(k)}{\sigma_\mathrm{T}^2}, \tag{37}$$

where

$$\sigma_\mathrm{B}^2(k) = \omega_0(\mu_0 - \mu_\mathrm{T})^2 + \omega_1(\mu_1 - \mu_\mathrm{T})^2 = \omega_0\omega_1(\mu_1 - \mu_0)^2 = \frac{(\mu_\mathrm{T}\omega(k) - \mu(k))^2}{\omega(k)(1 - \omega(k))} \tag{38}$$

is the between-class variance and

$$\sigma_\mathrm{T}^2 = \sum_{i=1}^{L} (i - \mu_\mathrm{T})^2 p_i \tag{39}$$

is the total variance of the levels. The optimal threshold k^* can then be found by maximizing the parameter η or equivalently σ_B^2:

$$\sigma_\mathrm{B}^2(k^*) = \max_{1 \leq k < L} \sigma_\mathrm{B}^2(k) \tag{40}$$

2.3.2 Trainable Weka Segmentation

Trainable Weka Segmentation (TWS) is a machine learning tool, developed by Arganda-Carreras et al. [41] and is available as open-source software as part of the *FIJI - ImageJ* [43] image processing software. It is based on the data mining and machine learning toolkit Waikato Environment for Knowledge Analysis (WEKA) [44]. The idea of TWS is to transform the segmentation problem into a pixel classification problem, where each pixel is assigned to a specific class. This assignment is done by manually classifying an image or a representative region of the image. These pixels are then represented in feature space and used as input for the training of a classifier. The trained classifier can then be used to classify the rest of the original image or completely new images. TWS works for 2D as well as 3D grey-scale or color images. The addressed image features are obtained by applying filters to the manually classified pixels or manipulating the pixels with other plugins of *FIJI - ImageJ*. The graphical user interface (GUI) allows the user to select different training features, i.e., filters, change the classifier and create several classes for the segmentation. Additionally, one obtains on-the-fly test results in the GUI, which allows for refinement of the parameters and retraining of the classifier. The TWS pipeline is displayed in fig. (12).
The classifier used for the TWS in this Master's Thesis was a random forest [45]. A random forest consists of several decision trees, grown from an underlying data set and typically contains the following steps (regarding classification trees) [46]:

1. Draw a bootstrap sample with replacement
2. For every bootstrap sample, different features can be chosen for the tree growing (often the features are chosen randomly)
3. Grow a tree for every bootstrap sample
4. Every tree votes for a class and the majority vote is taken as decision for the class

A bootstrap sample is chosen via bootstrap aggregation or bagging [47], which means basically choosing random samples from the whole data set for training.

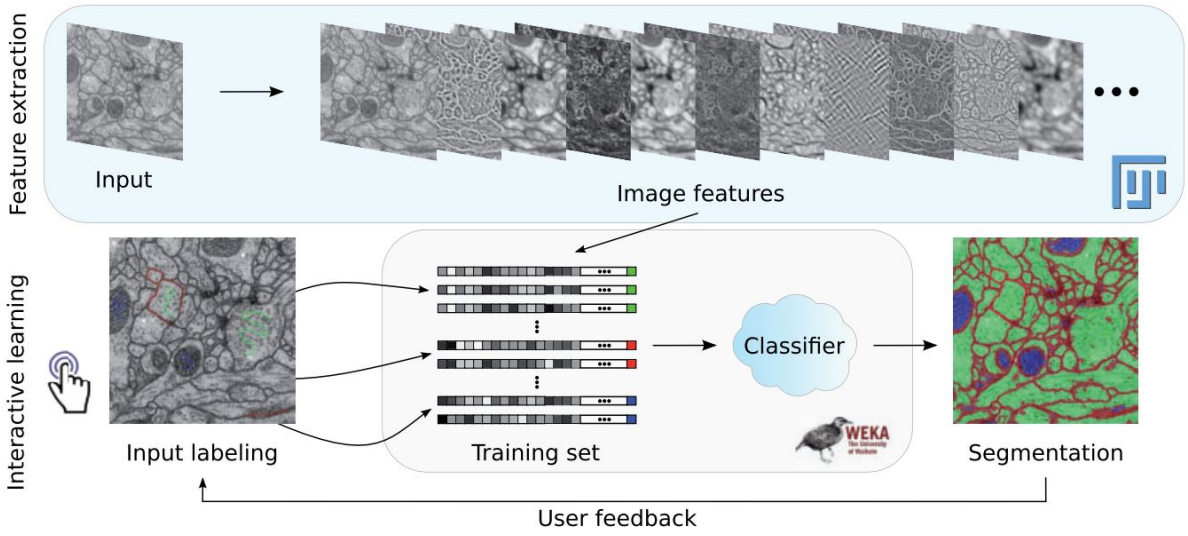

Fig. 12: Sketch of the TWS pipeline - from [41]
An input image is classified manually and features for these pixels are extracted and represented as feature vectors. The feature vectors are used for training a WEKA learning scheme which can then be applied to classify the rest of the image (2D and 3D). On-the-fly results in the GUI allow for changing the parameters and labelling of more pixels for refinement and retraining of the classifier.

3 Experimental Setup

The experiments were carried out at the coherent-small-angle-X-ray-scattering (cSAXS) beamline of the Swiss Light Source (SLS). The experimental setup was constructed by them and the description given in this section is based on the cSAXS website [48], the beamline manual [49] and two articles, both by Holler et al. [50] [51], which describe two different ptychography instruments.

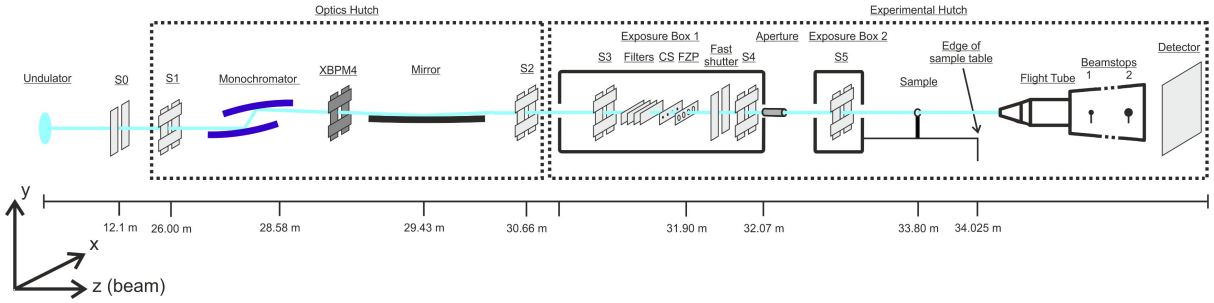

Fig. 13: Sketch of the experimental setup - adapted from [52]

The SLS is a third generation synchrotron source with a 2.4 GeV electron storage ring with a circumference of 288 m and 12 straight sections. The beamcurrent is kept constant at about 400 mA. The source for the cSAXS beamline is an in-vacuum undulator, generating X-ray light with extreme brightness, in one of the straight sections. The undulator length is 1.82 m, consisting of 96 periods with a length of 19 mm. The minimum undulator gap is 4.6 mm and the maximum K-parameter is 2.46. The K-parameter basically characterizes the amplitude of the electron oscillations within the undulator. The extent of the source, at an energy of 12.4 keV, given as full width at half maximum (FWHM), is 202 µm x 18 µm with a divergence of 135 µrad x 25 µrad (FWHM).
The beamline setup is sketched in fig. (13). The setup contains 6 slits. The slits S1 to S5 consist of four individually movable blades, respectively and allow for controlling the shape of the beam. Slit S0 is closest to the source and only consists of two movable blades. It allows for horizontal confinement of the beam and creates a secondary source. By default, the width of the slit is set to 20 µm, to have a spatially coherent illumination of the Fresnel zone plate (FZP). In order to define the X-ray energy, a Si(111) double crystal monochromator is used. The first crystal is cooled with liquid nitrogen. It offers an energy range of about 4 keV to 18.6 keV with a energy resolution of about $\Delta E/E \approx 2 \cdot 10^{-4}$. The second crystal is bendable and can be used for horizontal focusing of the beam down to 20 µm (FWHM) at sample position. The mirror, as indicated in fig. (13), is a fused silica mirror, containing three stripes with different coatings. The coatings are rhodium, platinum and no coating. The purpose of the mirror is to suppress higher harmonics of the source and it can further be used for vertical focusing of the beam via a bending mechanism. At the sample position, a spot size in the vertical direction down to 5 µm can be reached. In between the mirror and the monochromator, there is a X-ray beam position monitor (XBPM4) for monitoring the beam position.
Besides slits and a fast shutter, exposure box 1 contains filters, a central stop (CS) and a FZP. The filters are placed on filter wheels and contain silicon and germanium filters with different thicknesses and other calibration materials. The central stop blocks the central

part of the beam and the FZP is used for focusing of the beam.
Between the sample and the detector, there is a flight tube that is evacuated to a pressure in the regime of 10^{-4} mbar, to prevent air scattering and absorption of the X-rays upon propagation to the detector after interaction with the sample. Three flight tubes with different lengths of 2.06 m, 5.26 m and 7.00 m are available. At the end of the flight tube there is an in-vacuum detector. The detector used for the experiments performed for this Master's Thesis was a single photon counting *500k Eiger* detector [53] with an array size of 512 x 1024 pixels, a pixel size of 75 µm x 75 µm and an active area of 84 mm x 34 mm.

For positioning of the sample with respect to the beam, differential laser interferometry [54] is used. This allows for positioning accuracy and stability in the nm range even upon sample rotation as it is necessary for tomography. The setup offers the possibility to change between two stages for the experimental hutch, one operating at ambient conditions, called "flexible tOMography Nano Imaging" (flOMNI) [50] and one operating at cryogenic temperature and ultra-high vacuum (UHV), called "tOMography Nano crYo" (OMNY) [51]. The cooling for the OMNY stage is done with liquid nitrogen and leads to a sample temperature of about 90 K. To generate the UHV, turbomolecular pumps and ion-getter pumps are used, resulting in a pressure of about $2 \cdot 10^{-8}$ mbar. Due to the pressure difference between the OMNY chamber and the flight tube, they are separated by a 13 µm thick Kapton foil.

For the coarse alignment of the sample and the determination of the field of view (FOV) for the measurement, an X-ray eye is installed, which utilizes a 100 µm yttrium aluminum garnet scintillator. The scintillator is monitored by a CCD camera using a 10x microscope lens.

The coherence properties of the X-ray beam can be estimated with eq. (13) and eq. (16). The relation between the FWHM extent of the source and the sigma width is $\sigma = \frac{\mathrm{FWHM}}{2\sqrt{2\ln 2}}$ [27]. The distance R between the source and the sample is roughly 34 m. This results in a longitudinal coherence length of $\xi_\mathrm{l} = 0.5\,\mu\mathrm{m}$ and a transverse coherence length of $\xi_\mathrm{h} = 13\,\mu\mathrm{m}$ in horizontal direction and $\xi_\mathrm{v} = 142\,\mu\mathrm{m}$ in vertical direction.

For the experiments presented in this thesis, the beam was focused using a central stop, a FZP and a pinhole aperture. This setup was shown to provide ptychographic reconstructions with good resolution and good signal to noise ratio [55]. The filters, located in exposure box 1 were not used.

4 Sample Preparation

One goal of this thesis is to determine whether there is a simple technique for preparing samples to be measured at the cSAXS beamline at the SLS. Several methods for the preparation of FtF-bonds and transferring them to the tip of the pin, which is used for imaging at the cSAXS beamline at the SLS, were developed and examined. The preparation of the FtF-bonds turned out to be simple, whereas cutting them and transferring them to the pin was challenging if done manually. To start with, a manual approach was chosen since it would be more cost-efficient if a lot of samples were needed for representative statistics in future experiments. In the end, a sample preparation using Focused Ion Beam (FIB) and Scanning Electron Microscopy (SEM) was also done to obtain better and more promising samples.

4.1 The OMNY Pin

The sample preparation for the experiments turned out to be challenging as the sample had to be mounted on a pin specially designed for the flOMNI and OMNY experiments [56]. There are different variants of the OMNY pin for various types of samples. The pin used for the experiments performed for this Master's Thesis was the tip version depicted in fig. (14) and fig. (16). It provides a sharp tip that may also be flattened by using polishing paper, if needed for the sample mounting. The pins are made of oxygen-free copper, which provides a good thermal conductivity and coated with a 3 µm thick layer of gold. The gold layer prevents cold welding effects between the pin and the receptor. The receptor and the base geometry of the pin are displayed in fig. (15). For mounting, the pin has to be pushed into the matching pin receptor, where the conical area (1) provides the holding surface. To provide a good thermal conductivity from the receptor to the pin, a large contact area is needed. This is ensured by the conical shape, which creates high surface forces when mounting. Section (2), in fig. (15(a)), is the handling area in which the pin may be grabbed with tweezers. The gripping area has been introduced to avoid damaging the conical area, which could lead to cold welding effects between the pin and receptor. The sample position is 3 mm above the upper pin surface and centered on the pin's axis, as depicted in fig. (15(a) (3)).
Due to the experimental setup and pin design, there are several requirements for mounting a sample to the pin to achieve high-resolution images. Firstly, the sample has to be confined within a cylinder with a maximum diameter of about 100 µm at the tip of the pin. Secondly, there has to be air at both sides of the sample for all rotation angles. Thirdly, the sample should be centered to the axis of the pin. And finally, there has to be a separation layer between the pin and the sample to avoid X-rays passing through the metal pin, as this would introduce artifacts in the measurement.

4.2 Fiber to Fiber Bond Preparation

For the preparation of FtF-bonds in this study, two types of cellulose pulp fibers were used. Softwood fibers were used for the flOMNI experiment, whereas hardwood fibers were used for the OMNY experiment. The softwood was "MonopolX Langfaser Fraktion Unbleached Softwood Kraft Pulp" and the hardwood was "Santa Fe Bleached Hardwood Kraft Pulp" both produced by the company *Mondi*. The chemical composition is given

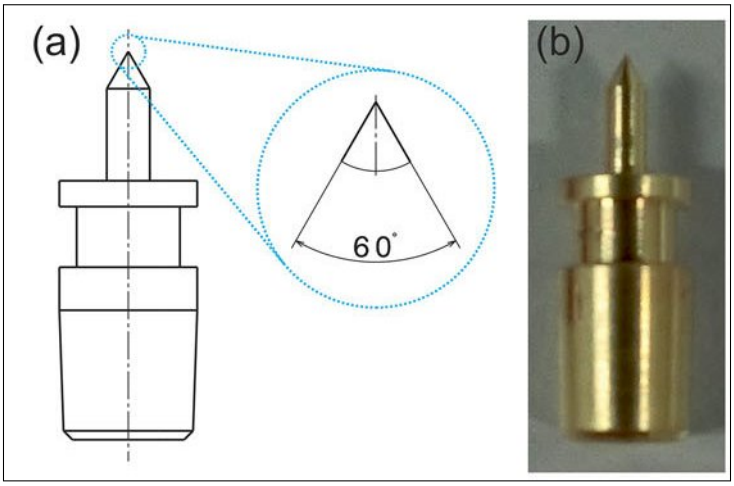

Fig. 14: Tip version of the OMNY pin - adapted from [56]
(a) ... schematical drawing
(b) ... photography of the pin

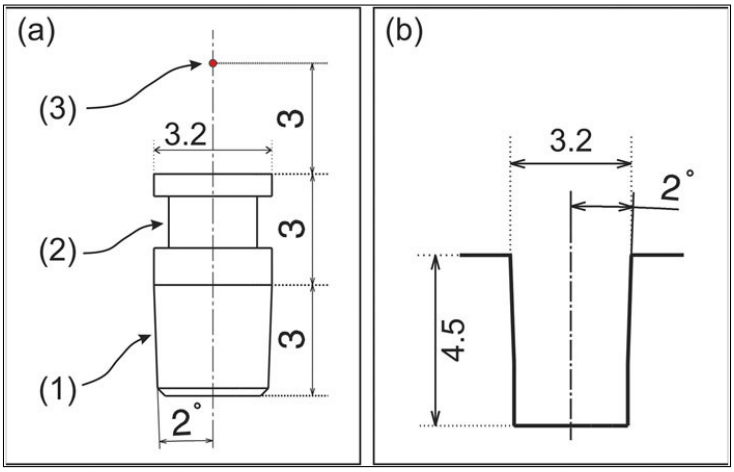

Fig. 15: Basic geometry of the OMNY pin - from [56]
(a) ... basic geometry - (1) conical mounting base, (2) handling area, (3) measurement position
(b) ... the matching pin receptor
All dimensions are shown in mm

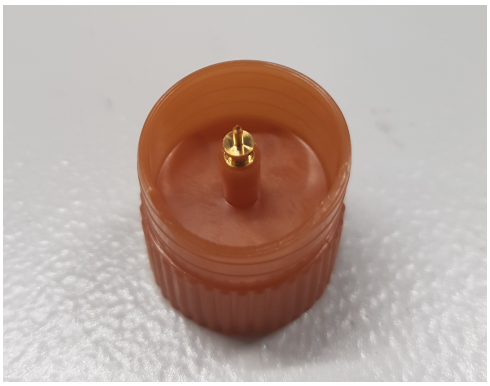

Fig. 16: Photo of the OMNY pin in the plastic pin holder

Tab. 1: Chemical composition of the cellulose fibers
The values are from measurements of the company *Mondi* and correspond to mass-percent.

Content	softwood	hardwood
Cellulose	78.1 %	77 %
Hemicellulose	16.4 %	23 %
Lignin	5.4 %	0 %
Extractives	0.1 %	0 %

in tab. (1). The softwood fibers are about three times longer and wider in diameter than the hardwood fibers.

In order to produce FtF-bonds, a method similar to the one reported by Stratton [57] was conducted.
A big droplet of distilled water was placed on a big Teflon plate. Then, cellulose fibers, taken out of a suspension with tweezers, were deposited inside the water droplet. In the next step, a small droplet of distilled water was placed on a small Teflon plate with a size of about 3 cm x 3 cm (see fig. (17a)). Two single fibers were taken from the fiber suspension of the big droplet and transferred to the small water droplet. While viewing with an optical microscope, as displayed in fig. (18), the two fibers were brought to a right-angled, overlapping position by manipulation with tweezers. The droplet was then covered with a second Teflon plate by slowly approaching from the top and forming a water meniscus. The Teflon plate was then wrapped in aluminum foil and pressed slightly with two fingers. Subsequently, a cylindrically shaped 1 kg weight with a diameter of about 10 cm was placed on top of the Teflon plate to press the fibers. The duration of the pressing step varied between 5 min and 20 min because 6 of such wet FtF-bonds were prepared in series. Afterward, the plates were dried for 10 min or 20 min using an oven (*Rapid Köthen*) with a vacuum stage to make sure the excess water evaporates. The temperature for drying was around 90 °C and the pressure at about −0.9 bar. After drying, the Teflon plates were opened slowly and the FtF-bond loosened carefully with tweezers, as the fibers tend to stick to the Teflon plate (see fig. (17b)). For further processing, the FtF-bonds were transferred to a microscope slide. A typical softwood FtF-bond is shown in fig. (19) with 5x magnification and in fig. (20) with 20x magnification.

Due to the smaller size of hardwood fibers, the method explained above did not work, thus a different approach was performed. Instead of only putting two single fibers into the small droplet between two Teflon plates, more fibers were used to create a randomly oriented network. After drying, the fiber network was placed on a microscope slide and suitable FtF-bonds, i.e., the ones intersecting at an angle of approximately 90°, were cut out of the network with a scalpel. A typical hardwood FtF-bond is shown in fig. (21). Note the smaller size of the hardwood fibers compared to the softwood fibers.

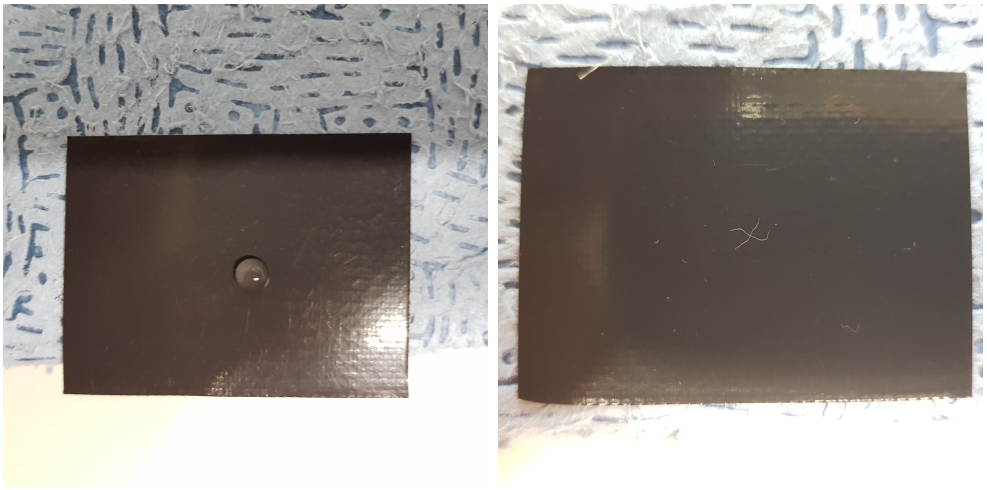

(a) Small droplet of distilled water on Teflon plate

(b) FtF-bond after drying in an oven (*Rapid Köthen*)

Fig. 17: Sample preparation process

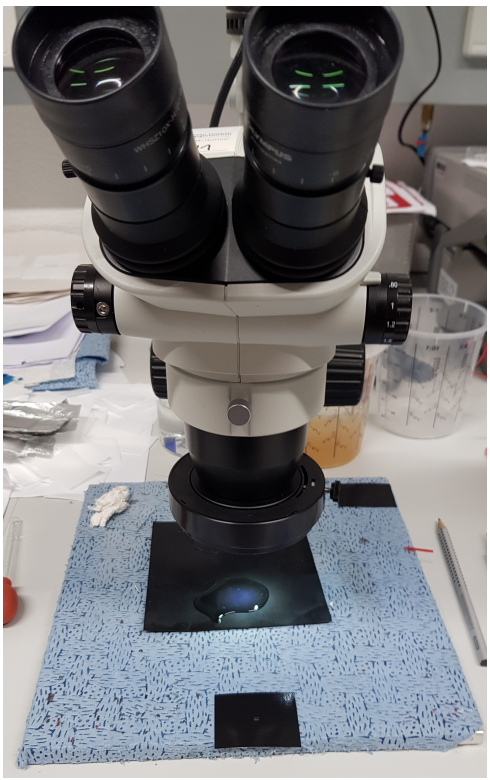

Fig. 18: Overview of sample preparation workplace

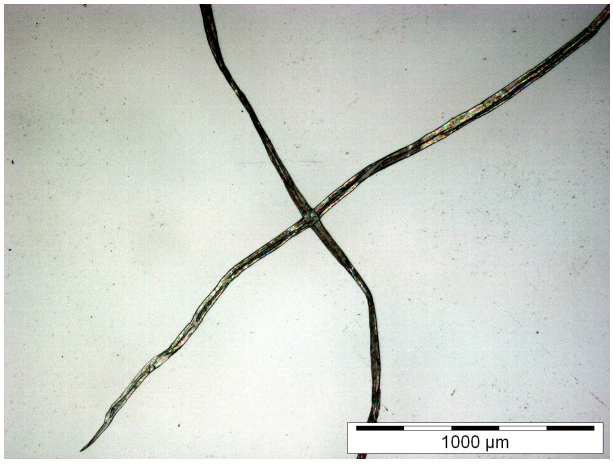

Fig. 19: Optical microscopy image of a typical softwood FtF-bond with 5x magnification

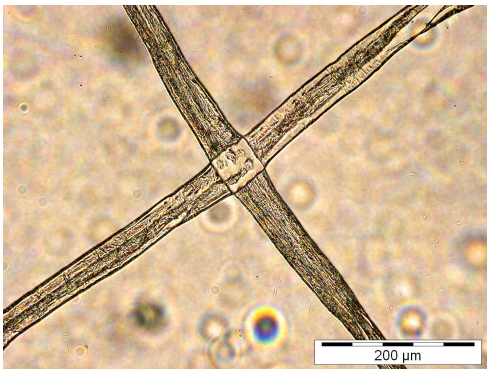

Fig. 20: Optical microscopy image of a typical softwood FtF-bond with 20x magnification

Fig. 21: Optical microscopy image of a typical hardwood FtF-bond with 20x magnification

4.3 Manual Sample Preparation

When a lot of samples are needed to obtain statistically significant measurements, a cost-efficient approach like manual sample preparation should be aimed for. Therefore, simple tools available in a standard chemistry or physics laboratory were used: standard scalpels for cutting, standard tweezers for transferring or manipulation and standard adhesives for sticking the cellulose fibers to the pin. For the latter, it has to be mentioned that when dealing with paper or cellulose fibers, the correct adhesives have to be chosen carefully. For sticking cellulose fibers, standard nail polish, cyanoacrylate adhesives or 2-component synthetic resin adhesives (2C-adhesives) may be used, since they do not penetrate the cellulose fibers and do not moisten their surface. However, using them for experiments with X-rays might be problematic, since the glue would get irradiated and potentially suffer radiation damage. Hence, a sample sitting on top of the glue would start moving, thus introducing artifacts in PXCT measurements. Eventually, a more sophisticated, glueless mounting approach was developed (see section 4.4).

4.3.1 Sample cutting

Before mounting the FtF-bond to the OMNY pin, the overlaying arms of the fibers had to be removed. This was done by using a standard scalpel with a round cutting tip. The FtF-bond was placed on a microscope slide and viewed with the optical microscope shown in fig. (18) with a maximum magnification of 4. The cutting was done stepwise. At first, about half of the overlaying fiber was removed. Then, a cut close to the edge of the overlapping area was conducted. This was done at all four sides to obtain only the overlapping part of the two fibers. As the fiber diameter is roughly around 50 µm for softwood fibers and even less for hardwood fibers, cutting it to the actual size of the FtF-bond was very challenging. Additionally, factors like hand shivering and the lack of better magnification, made cutting difficult. Fig. (22) depicts cut softwood FtF-bonds. The size of both samples is too big, as they do not meet the size criterion explained in section 4.1. The diameter of the circles drawn in fig. (22) need to be at most 100 µm to achieve a high-resolution at the PXCT measurement in a reasonable time. Another crucial point is cutting close to the edges of the FtF-bond. This cutting process may open the bond slightly with the scalpel. Also, fraying the edges of the fibers should be avoided, as the sample size would be increased compared to samples with smooth edges (see fig. (22)). The bond area of the sample depicted in fig. (22a) looks more homogeneous than the one in fig. (22b). This could mean that the fibers are not fully bonded, so a sample with both, smooth edges and a good bond area would be preferred.
Fig. (23) displays two more cut softwood FtF-bonds. Both samples have smooth edges and a good optically bonded area, but are still too big. In total, about 50 softwood samples that were prepared and cut for this Master's Thesis had a circular diameter larger than 100 µm and therefore were not suitable for the PXCT measurement. Hence, for the second PXCT experiment, hardwood fibers were used as they have a smaller fiber diameter. Fig. (24) depicts two cut hardwood FtF-bonds with a circular diameter well below 100 µm. The edges are partly frayed, but the sample size is still sufficient.

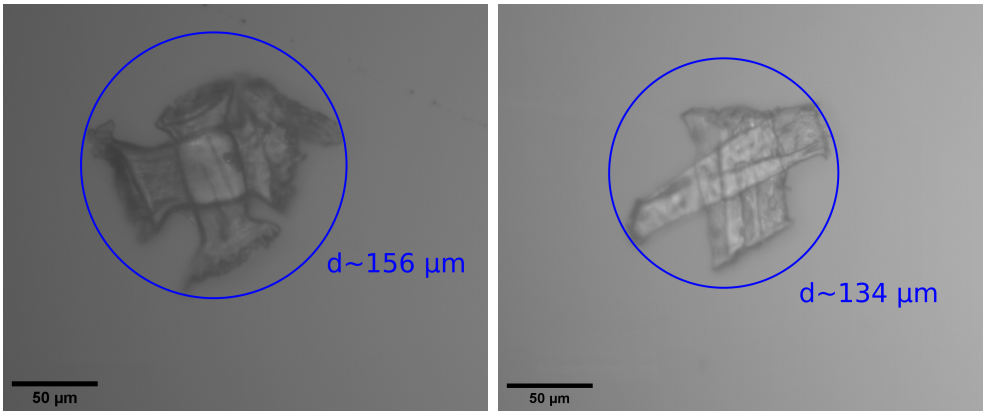

(a) Cut FtF-bond-1 (frayed edges) (b) Cut FtF-bond-2 (smooth edges)

Fig. 22: Optical microscopy images of two cut softwood FtF-bonds with 20x magnification

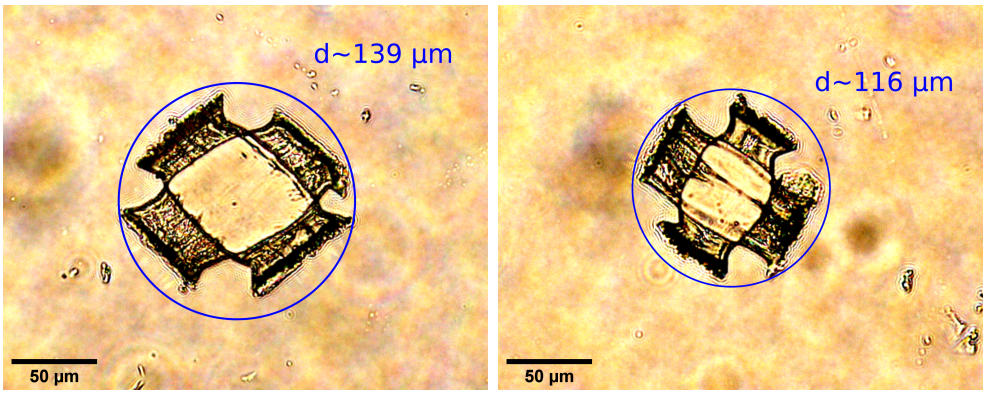

(a) Cut FtF-bond-C4 (b) Cut FtF-bond-C8

Fig. 23: Optical microscopy images of two cut softwood FtF-bonds with 20x magnification

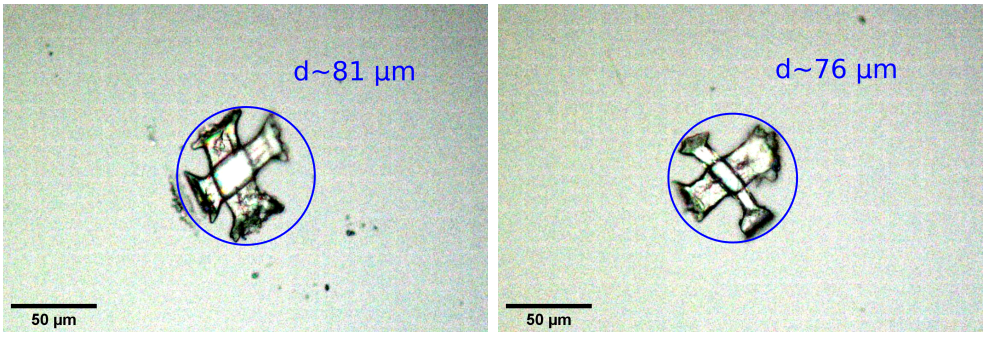

(a) Cut FtF-bond-HC1 (b) Cut FtF-bond-HC2

Fig. 24: Optical microscopy images of two cut hardwood FtF-bonds with 20x magnification

4.3.2 Mounting Method 1 - Nail Polish on flattened Pin

To examine the mounting to the OMNY pin, the FtF-bond displayed in fig. (22b) was used, despite the big size. At first, a pin (pin-1) was polished with fine grained sandpaper to flatten the tip and build a platform (see fig. (25)). To stick the sample to the pin, standard nail polish was used (*essence the gel nail polish - schwarz 46*). The pin was grabbed with tweezers at the handling area and carefully dipped into the nail polish to create a droplet. Then, the FtF-bond displayed in fig. (22b), which was lying on a microscope slide, was carefully picked up. This process was done by slowly approaching with the pin to the FtF-bond, while viewing with the microscope with 4x magnification. The drying time of the nail polish was about 30 s. The result is shown in fig. (26).

While taking the optical microscopy images the pin fell sideways on a microscope slide. As shown in fig. (27), the FtF-bond was still attached to the pin, but the nail polish got damaged. The filament, the FtF-bond was attached to, broke off. Moreover, the shape of the nail polish cap is not optimal. It should be more spherically shaped, smaller and nail polish filaments should be avoided. The formation of filaments can be explained by high viscosity of the nail polish. Furthermore, the sample is tilted and does not meet the requirements for sample mounting, described in section 4.1.

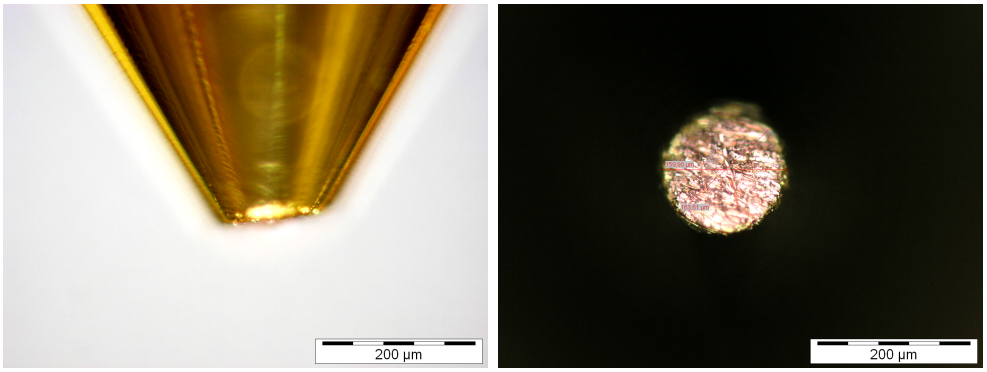

(a) Side view (b) Top view

Fig. 25: Optical microscopy images of pin-1 (flattened) with 20x magnification

To avoid nail polish filaments and get a nail polish cap with an optimal semi-spherical shape, three different types of nail polish were tested.

- NP1 - *essence the gel nail polish - schwarz 46*
- NP2 - *ASTOR 618 Blackberry smoothie*
- NP3 - *trend IT UP N°1 NAIL POLISH - 020 schwarz*

The best one turned out to be NP3 as it was the most liquid and therefore had the best-shaped nail polish caps on the pin. Furthermore, a test series showed that the nail polish on the pin should be dried with the tip pointing towards the ground to form a spherical shape and that the drying time should be about 1 min.

To prepare another sample, pin-1 was cleaned with acetone and isopropanol. Then the sample mounting procedure explained above was performed with NP3 instead of NP1. The sample used for mounting is displayed in fig. (28a) and the result of the sample

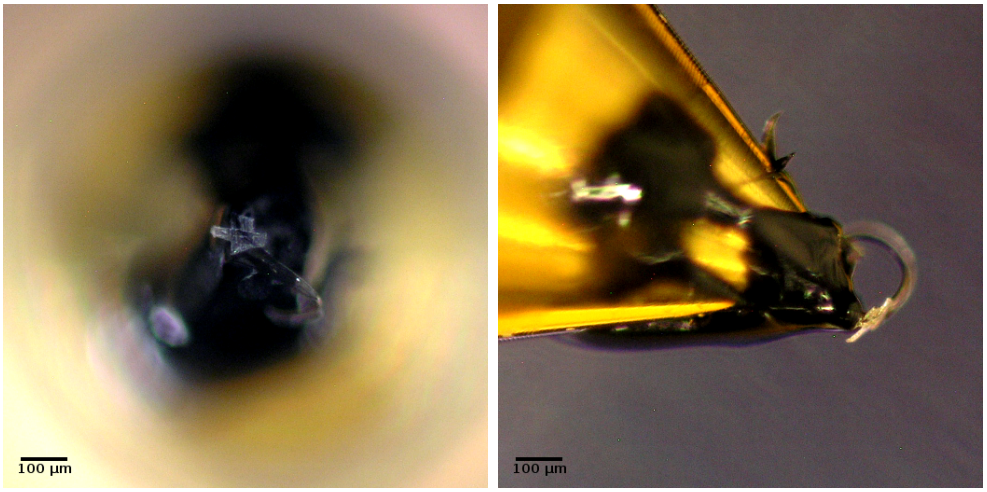

(a) Top view (b) Side view

Fig. 26: Optical microscopy images of softwood FtF-bond-2 on pin-1 with 5x magnifiaction

mounting is depicted in fig. (28b) - fig. (28d).
The result is better than the one shown in fig. (26), i.e., the nail polish cap is more uniform and drop-like, there are no filaments and it offers a flat platform. But the mounted sample is still problematic. Firstly, the FtF-bond is larger than 100 µm. Secondly, the FtF-bond is not centered to the pin axis. And finally, this off-axis position and the large size of the nail polish cap are a limitation, since PXCT is not capable of only focusing on a part of the sample. Thus, the field of view would have to be increased to fit in the nail polish cap and the sample, which would lead to a long measurement time. Hence, the mounting approach was modified to be able to create small spherically shaped nail polish droplets, as explained in section 4.3.3.

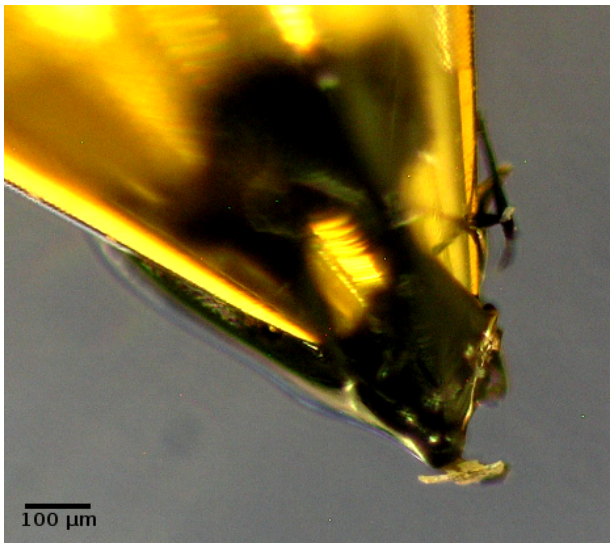

Fig. 27: Optical microscopy image of softwood FtF-bond-2 on pin-1 with 5x magnification after falling sideways on a microscope slide

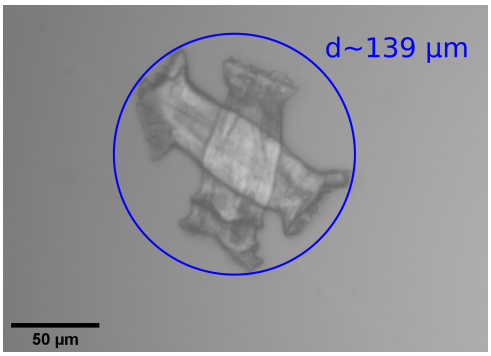

(a) FtF-bond-190816-2 (20x)

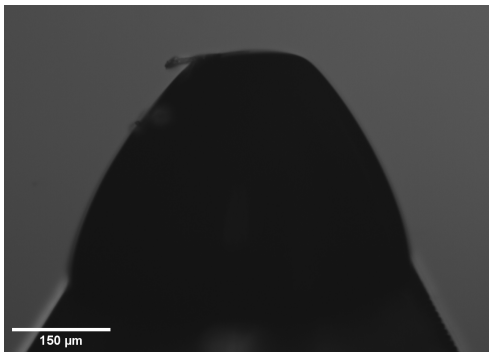

(b) Side view (10x)

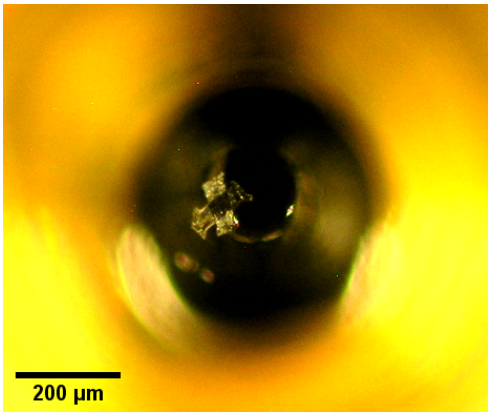

(c) Top view (5x)

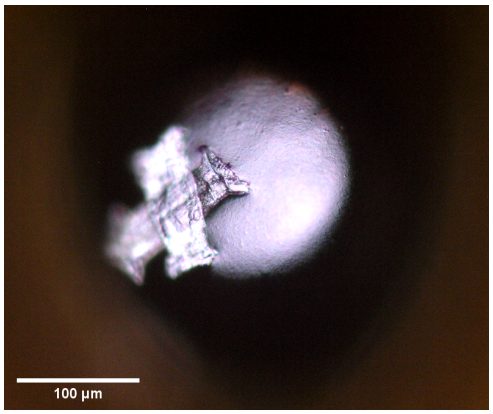

(d) Top view (20x)

Fig. 28: Optical microscopy images of softwood FtF-bond-190816-2
(b) - (d) ... FtF-bond-190816-2 on pin-1

Experiments with Liquid Nitrogen To assess the behavior of nail polish at cryogenic temperatures, some experiments with liquid nitrogen (LN_2) were performed. At standard pressure LN_2 has a temperature of about 77.4 K [58]. LN_2 is also used in the cryo PXCT measurements and thus is appropriate for testing.

The first tests were performed with a metal needle of about 10 cm length, attached to a wooden grip (see fig. (29)). The tip of the needle was dipped into the nail polish for a short time and then dried for several minutes with the tip pointing downwards. Subsequently, the needle was dipped into a Dewar vessel filled with LN_2 for a certain amount of time and then analyzed with an optical microscope. This procedure was performed for the three different types of nail polish (NP1, NP2, NP3). The timings and the results are listed in tab. (2).
Exemplary images of experiment 5, before and after the LN_2 treatment, are displayed in fig. (30). Low temperatures seem to have no impact on the nail polish droplet morphology, as even small features on the surface remain unchanged and no cracks occurred.

To also be able to make statements about the performance of nail polish on the tip of the OMNY pin with an FtF-bond attached to it, a further experiment was performed. To do so, a mount for the OMNY pin was created, as displayed in fig. (31c). The mount, including the completed sample depicted in fig. (28), was placed in the Dewar vessel and flooded with LN_2 (see fig. (31)). After about 59 min the mount, including the sample, was taken out of the Dewar vessel.
A comparison of the sample before and after the LN_2 treatment is depicted in fig. (32). The nail polish cap does not show cracks or changes in surface morphology. Additionally, the FtF-bond is still on top of the nail polish cap at the same position. The big filament present in the images is just dust and was removed carefully at a later point with tweezers. In fig. (32f) another small dust filament close to the FtF-bond is visible, but this would not be problematic for the measurements.

Tab. 2: Experiments with LN_2 and needle
Exp. ... number of experiment
Nail polish ... nail polish type
Drying time ... rough drying time of nail polish droplet on the tip of the needle
Time LN_2 ... time of needle dipped in LN_2
Visible changes ... visible changes of nail polish droplet after the experiment

Exp.	Nail polish	Drying time / min	Time LN_2	Visible changes
1	NP1	10	10 s	Filaments
2	NP1	8	15 s	No changes
3	NP2	12.5	1 min	No changes
4	NP3	11	20 min	No changes
5	NP3	16	63 min	No changes

(a) Photo of the needle in a plastic holder

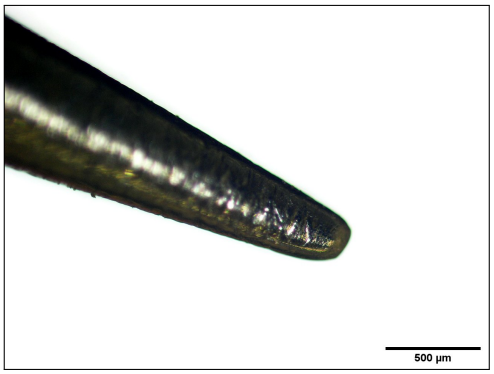

(b) Optical microscopy image of the tip of the needle (5x)

Fig. 29: Images of the metal needle used for experiments with LN_2

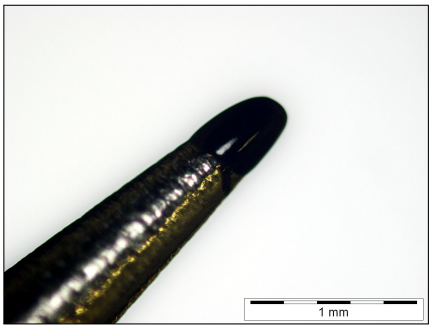

(a) Nail polish droplet before LN_2 treatment (5x)

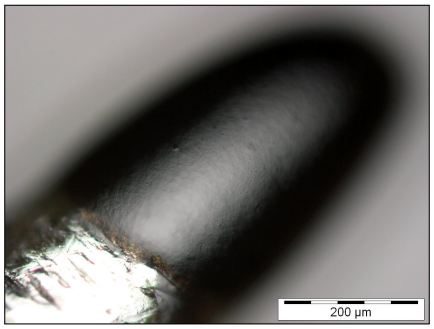

(b) Nail polish droplet before LN_2 treatment (20x)

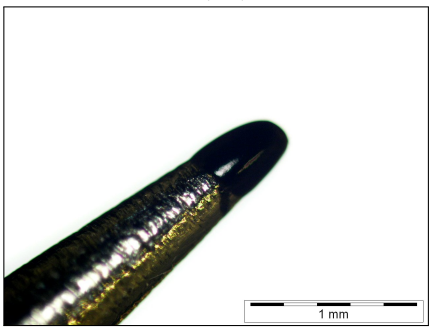

(c) Nail polish droplet after LN_2 treatment (5x)

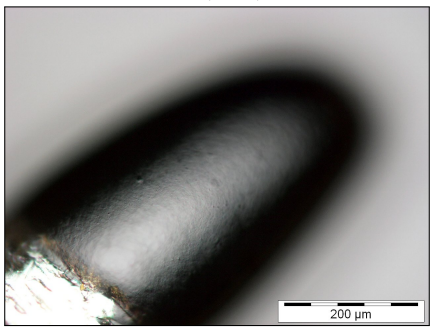

(d) Nail polish droplet after LN_2 treatment (20x)

Fig. 30: Optical microscopy images of nail polish droplet on the metal needle before and after LN_2 treatment (Experiment 5)

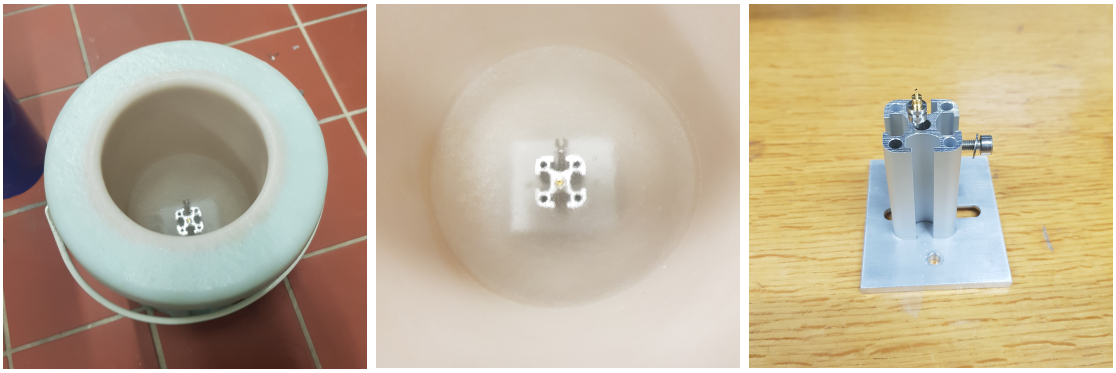

(a) Sample mount inside Dewar vessel filled with LN_2

(b) Close up of the Dewar vessel (fig. (31a))

(c) Sample mount for the OMNY pin

Fig. 31: Images of the sample mount and the Dewar vessel filled with LN_2

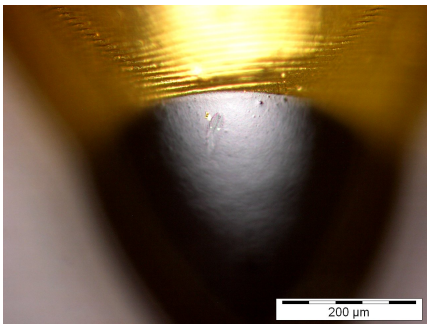

(a) Sample before LN_2 treatment (20x)

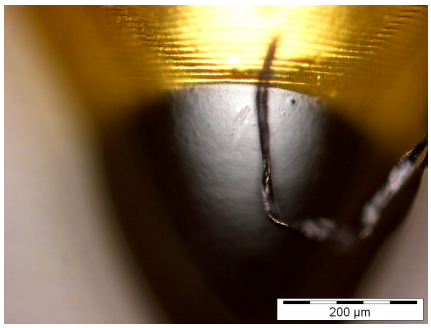

(b) Sample after LN_2 treatment (20x)

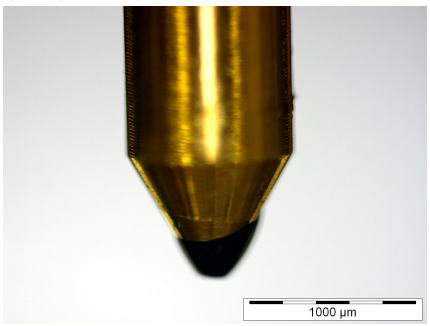

(c) Sample before LN_2 treatment (5x)

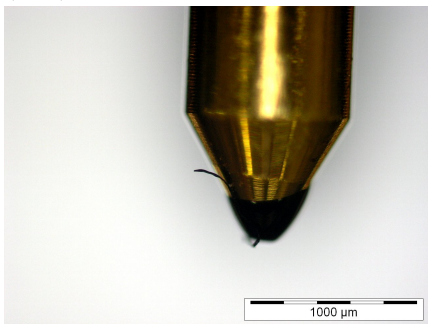

(d) Sample after LN_2 treatment (5x)

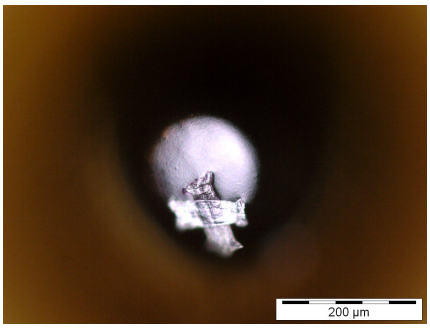

(e) Sample before LN_2 treatment (20x)

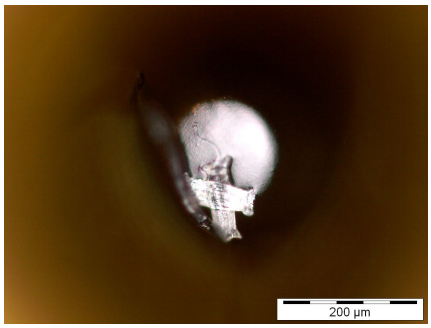

(f) Sample after LN_2 treatment (20x)

Fig. 32: Optical microscopy images of FtF-bond-190816-2 fixed with nail polish on OMNY pin-1 before and after LN_2 treatment

4.3.3 Mounting Method 2 - Nail Polish on sharp Pin

Since the measurement technique is not capable of interior tomography, the size of the nail polish cap had to be decreased. Thus, a new, not flattened OMNY pin (pin-2) displayed in fig. (33), was used. The goal was to create a spherically shaped nail polish droplet on top of the tip with a diameter smaller than the sample size. To do so, pin-2 was kept in the plastic pin holder and laid down laterally. While viewing with a microscope, the nail polish brush was brought closer to the tip of the pin slowly to then softly touch it and create a small droplet. Subsequently, an FtF-bond was grabbed with one arm of tweezers and then attached to the nail polish droplet carefully, while viewing with a microscope. The result is displayed in fig. (34).
The size of the nail polish droplet is smaller than the sample size and only touches the sample on a small spot (see fig. (34e)). The centering of the sample to the pin axis is sufficient, but the sample is slightly tilted. The tilting should be avoided, since it increases the field of view for the PXCT measurement, as displayed in fig. (34c). Another problem is that the field of view would be within the metal tip. This would introduce artifacts in the measurement and thus has to be avoided. Hence, a bigger spacing between the sample and the metal tip is needed.

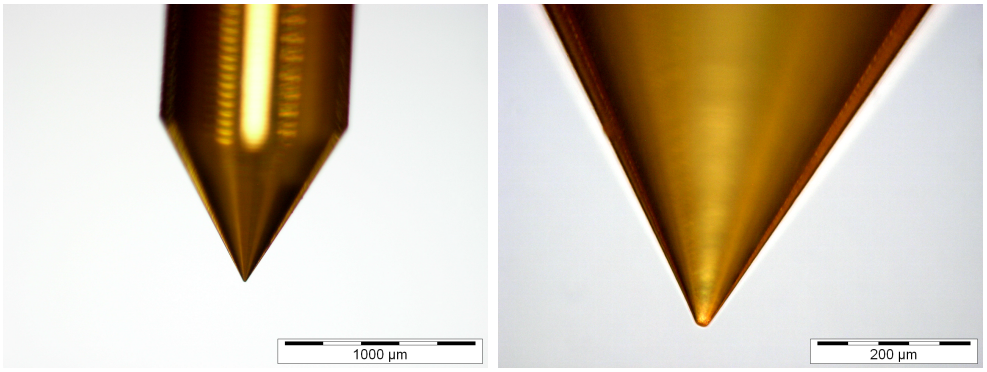

(a) Side view (5x) (b) Side view (20x)

Fig. 33: Optical microscopy images of pin2

To create a bigger spacing between the metal tip and the sample, several nail polish droplets were stacked on top of each other. Pin-2 was cleaned with acetone and isopropanol and for mounting, the same procedure as described above was performed. The FtF-bond for mounting is depicted in fig. (35a). The FtF-bond size is slightly too big, but still tolerable for measurement. Three single nail polish droplets were deposited (see fig. (35g)) with a drying time for each droplet of about 30 s. From the deposition of the last nail polish droplet to the successful transfer of the FtF-bond to the tip, about 5 min elapsed, so the nail polish had a long time for drying. Thus, the adhesive force between FtF-bond and nail polish droplet is probably weak.
The result of the sample mounting is shown in fig. (35). The centering of the sample is tolerable and it is not tilted. Moreover, there is a spacing of a few µm between the metal tip and the sample, which is sufficient for the PXCT measurement. Thus, the sample was stored for potential PXCT measurements.

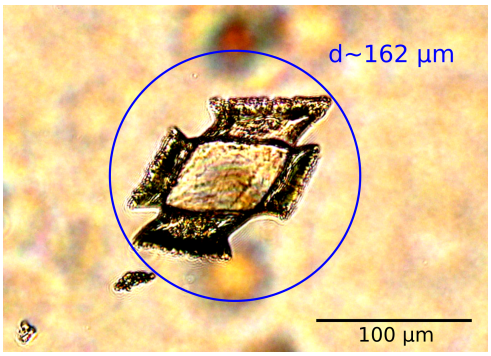

(a) FtF-bond-C2 (20x)

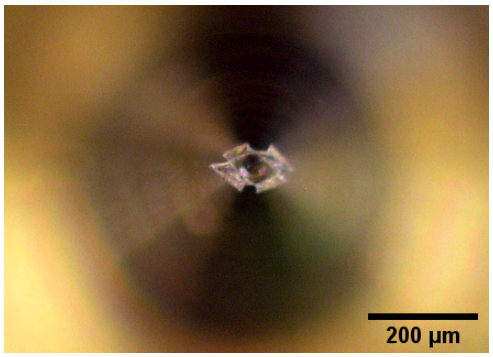

(b) Top view (5x)

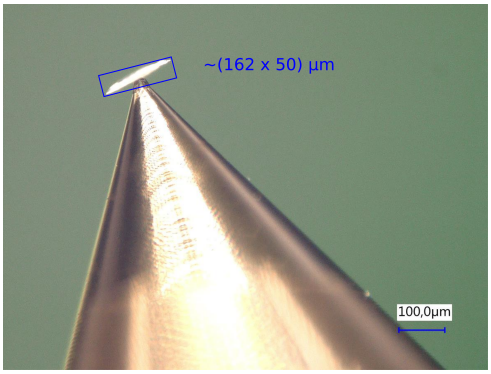

(c) Side view (25x) - field of view

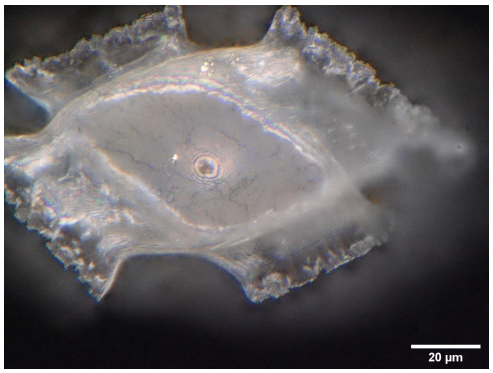

(d) Top view (250x)

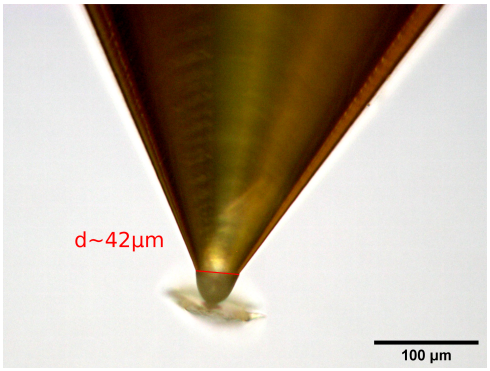

(e) Side view (5x) - nail polish droplet size

Fig. 34: Images of softwood FtF-bond-C2
(a), (b), (e) ... Optical microscopy images
(c), (d) ... Camera microscope images
(b) - (e) ... FtF-bond-C2 on pin-2

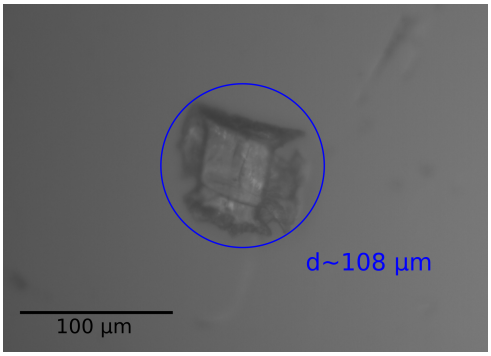

(a) FtF-bond-C10 (20x)

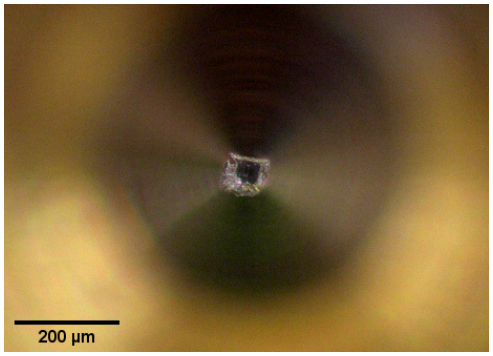

(b) Top view (5x)

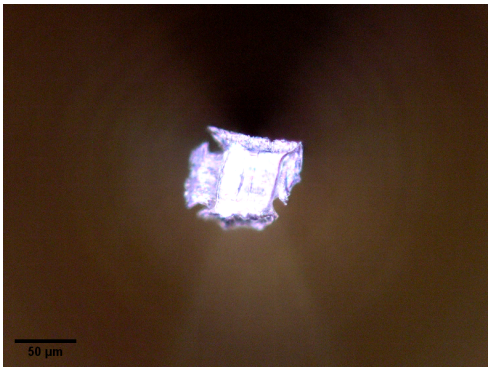

(c) Top view (20x)

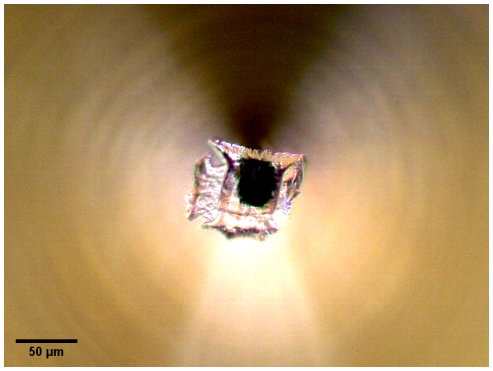

(d) Top view (20x)

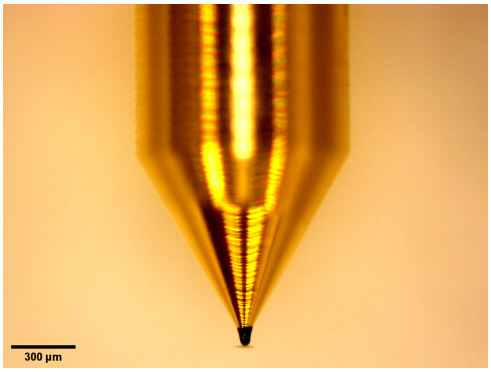

(e) Side view (5x)

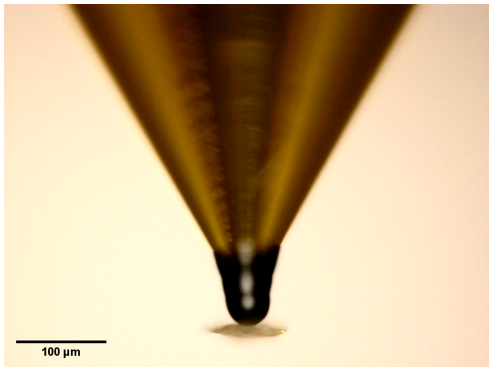

(f) Side view (20x)

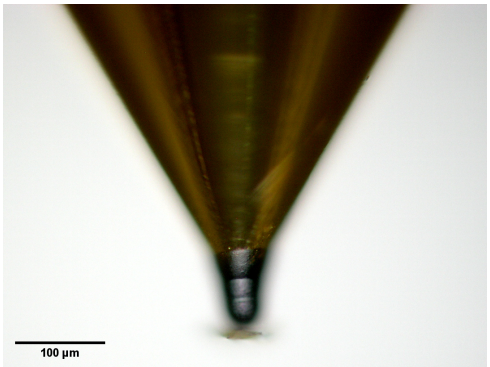

(g) Side view (20x)

Fig. 35: Optical microscopy images of softwood FtF-bond-C10
(a) ... FtF-bond-C10 before transfer
(b) - (g) ... FtF-bond-C10 on pin-2

4.3.4 Mounting Method 3 - Two-Component Adhesive on sharp Pin

Due to the unknown behavior of nail polish upon X-ray irradiation, samples using 2C-adhesive for sticking were prepared. Though, it has to be mentioned that also the behavior of 2C-adhesive upon irradiation was not known.
The 2C-adhesive used, was *Pattex - REPAIR EPOXY - Mini - Universal - 5 min* and a new, not flattened pin (pin-3) was used (see fig. (36)).
At first, some experiments concerning drying time, creating droplets on the pin and sticking FtF-bonds were performed. For this, an equal amount of both components (hardener and resin) was put on a microscope slide and mixed with tweezers. After mixing, the hardness was probed every few seconds. The hardening time turned out to be about 7 min, but it strongly depends on the ratio of both components.
To create a droplet on the tip of the pin, first, the pin was grabbed with tweezers and dipped into the 2C-mixture carefully. Subsequently, the pin was held in a reverse position to dry the adhesive. This procedure was done at several points in time, after mixing both components. It is important to notice that dipping the tip into the adhesive early after the mixing results in a non-well-shaped droplet. The reason for this is that the adhesive creeps up the pin, despite the reverse position, as it is still very liquid. Thus, for building a droplet, the adhesive must be somewhat hard and the building process must start close to the hardening time, i.e., at approximately 7 min.
The stacking of several droplets on the tip was additionally attempted, but it was hard to reproduce.
Furthermore, the precise time to pick up an FtF-bond is hard to quantify. It is worth to notice that if this process is done too early, the FtF-bond gets covered with glue or slides sideways as the adhesive is still too liquid. Thus, the FtF-bond must be picked up once the adhesive is in an advanced state of hardening.

As the stacking of droplets was hard to reproduce, a droplet of nail polish was deposited to create some separation between the tip and the sample by using the same method as described in section 4.3.3. After that, two droplets of 2C-adhesive were stacked on top of the nail polish droplet. For both droplets, the tip was dipped into the 2C-adhesive about 7 min after mixing both components. An FtF-bond was picked up about 1 min after deposition of the second 2C-adhesive droplet. The result is displayed in fig. (37).
The size of the nail polish and the 2C-adhesive would comply with the conditions of the measurements. However, the FtF-bond is not on top of the glue, but at the side. Thus, the sample is not suitable for PXCT measurements.

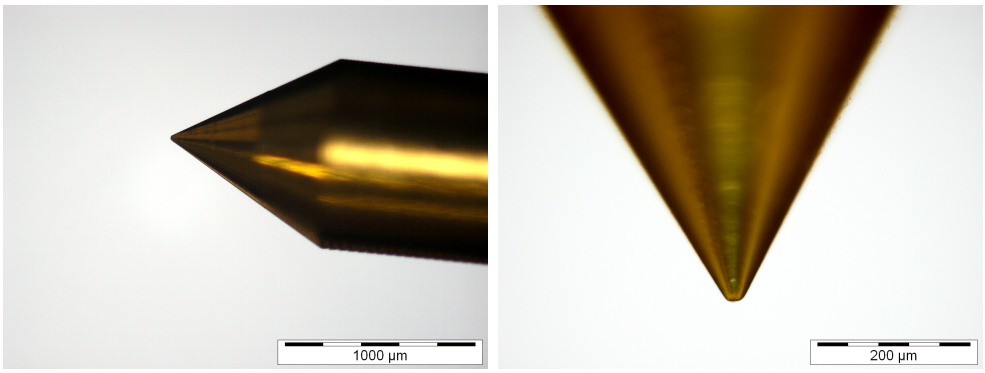

(a) Side view (5x) (b) Side view (20x)

Fig. 36: Optical microscopy images of pin-3

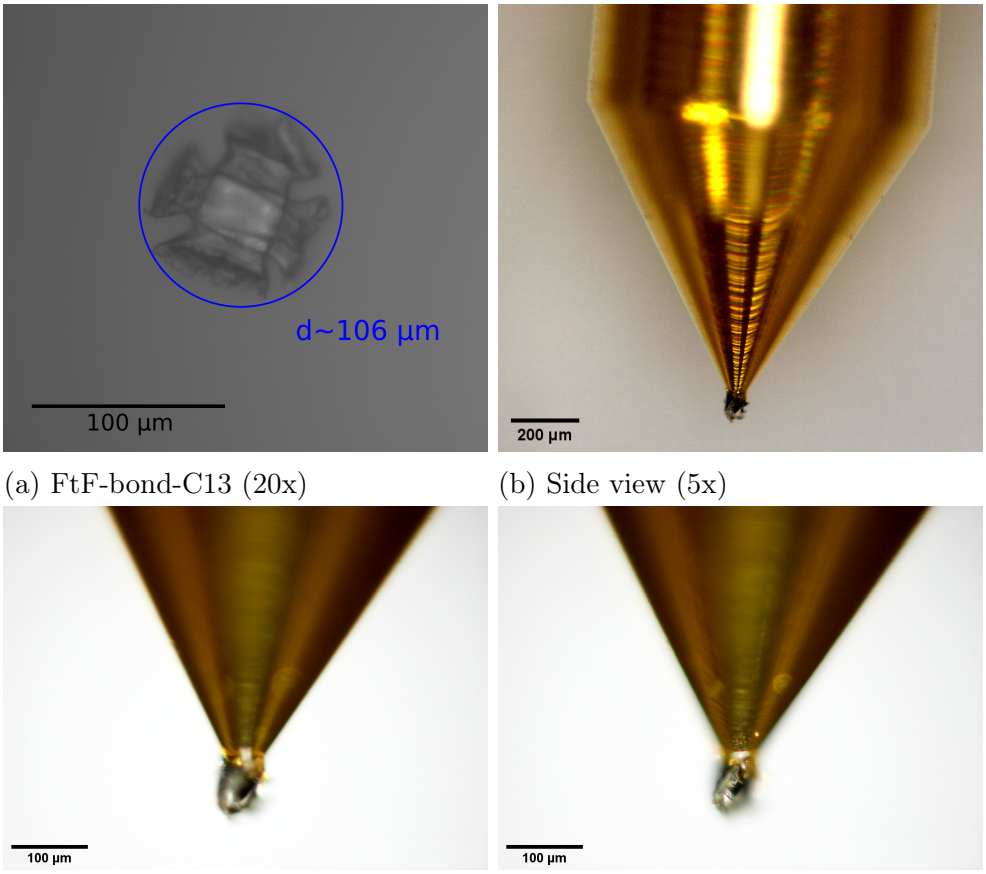

(a) FtF-bond-C13 (20x) (b) Side view (5x)

(c) Side view (20x) (d) Side view (20x)

Fig. 37: Optical microscopy images of softwood FtF-bond-C13
(a) ... FtF-bond-C13 before transfer
(b) - (d) ... FtF-bond-C13 on pin-3

4.3.5 Mounting Method 4 - Nail Polish Pillar and 2-Component Adhesive on sharp Pin

Since the droplet deposition on the pin was not reproducible with the 2C-adhesive used in the previous section, a new glue (*UHU PLUS - SOFORTFEST - 2-K-EPOXIDKLEBER - 2 min*) with a nominal drying time of two minutes was used. Besides, a new technique to create the droplets was explored with this new 2C-adhesive. The idea was to dip the pin into the adhesive, create a meniscus to the tip of the pin and then slowly pull it out. This process can not be controlled accurately by hand, thus an apparatus with micrometer-screws was used (*CAM200 Optical Contact Angle Meter - KSV INSTRUMENTS LTD*). The machine was initially designed for contact angle (CA) measurements of liquids. It offers a table that can be moved by micrometer-screws in x/y-plane and a holder where syringes can be clamped. The holder can be moved vertically (z-axis) by a micrometer-screw. In order to mount an OMNY pin in this machine, a gadget displayed in fig. (38) was created. It consists of the pin holder specially designed to fit in standard SEM's, extensions and screws. This fixture was then clamped to the holder of the CA machine. Furthermore, the CA device is equipped with a camera to see the droplets on the table from a side view. The whole setup is depicted in fig. (39).

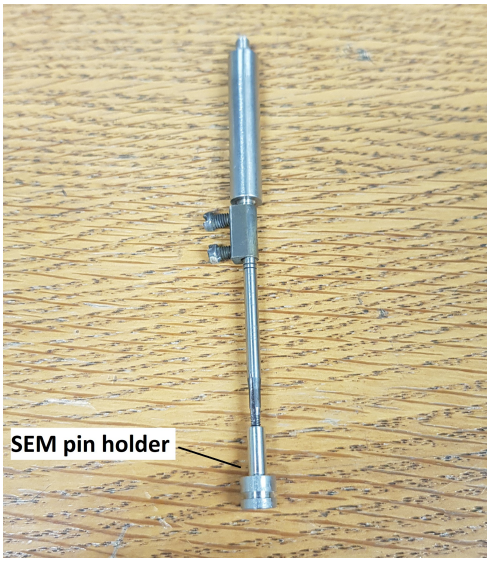

Fig. 38: Fixture for sample preparation with the CA device

For the experiment, a new pin (pin-6), displayed in fig. (40), was used. The tip happened to be flat because the pin fell out of the pin holder from a height of about 10 cm and landed on it's tip. At first, a nail polish pillar was created on the tip with the method described in section 4.3.3. This pillar was slightly flattened by putting the pin into the CA device and then softly pushing it against a microscope slide using the z-micrometer-screw. Then, the same amount of both components of the 2C-adhesive was mixed on a microscope slide and the time was measured from the point after mixing. After a certain amount of time (specified in the next paragraph), the pin was dipped into the mixture by using the z-micrometer-screw and then pulled back slightly to create a meniscus. After some more time (specified in the next paragraph), the pin was slowly pulled out of the mixture to form a droplet on the tip. The procedure was repeated several times to obtain a stack of droplets whenever the spacing between the droplet and the nail polish pillar was too

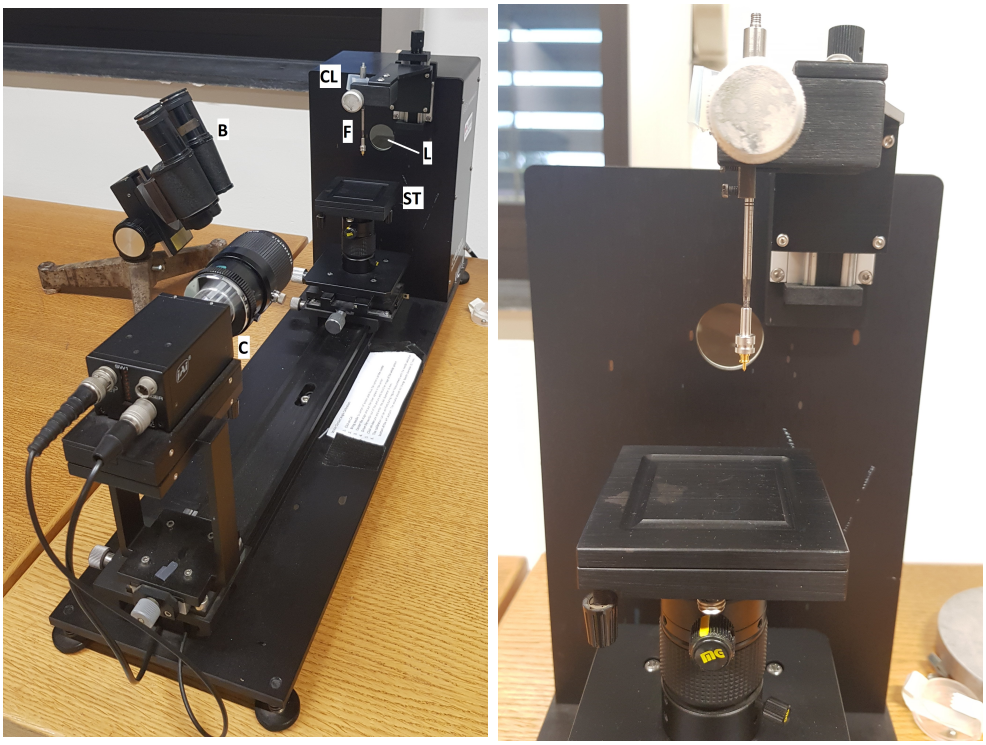

(a) CA device (b) Close up of (a)

Fig. 39: Optical Contact Angle Meter
B ... binocular, C ... camera, ST ... movable sample table, L ... tunable light source with aperture, F ... fixture for OMNY pin, CL ... clamp

small. After deposition of every droplet, the pin was imaged with an optical microscope. Once the droplet was sufficient, an FtF-bond was transferred to the tip. For this transfer process, a microscope slide with an FtF-bond was put on the CA machine table. The FtF-bond was coarsely centered to the pin axis with the x/y-micrometer-screws. Then, the pin was brought close to the FtF-bond by using the z-micrometer-screw. Subsequently, a fine alignment of the FtF-bond to the center of the pin was done with the x/y-micrometer-screws. This alignment was done with the help of the camera and a binocular which was located perpendicular to the camera. After the fine alignment, the pin was slowly lowered towards the FtF-bond up to the touching point and then brought back up.

Again, finding the times, when to dip the pin into the 2C-adhesive mixture and when to pull it out again, was difficult. Thus, reproducibility of the 2C-adhesive droplets was difficult, most likely because it was not possible to use exactly the same amount of both 2C-adhesive components for mixing. Hence, the time of drying varied a lot. Despite those difficulties, eventually two proper samples were prepared. The best droplets were created, when dipping the tip into the 2C-adhesive mixture 30 s after mixing, pulling it out 4 min after mixing and then keeping the pin hanging in the fixture for 2 min. After 2 min of hanging, the result was imaged with an optical microscope.

Fig. (41a) shows the flattened nail polish pillar and fig. (41b) shows the 2C-adhesive droplet on top of the nail polish pillar. For this sample only one 2C-adhesive droplet was created. To create the droplet the timings from above were used. The FtF-bond was transferred to the tip 21 min after mixing. The transfer of the FtF-bond was successful,

though it was not centered to the pin axis (see fig. (42)). Thus the sample was not suitable for measurements, so the pin was cleaned using acetone and isopropanol.

For the second sample, three 2C-adhesive droplets were created using the same timings as above. Eventually, the last droplet was so big, that it surrounded the other ones (see fig. (43)). The droplet has a decent size and the spacing between the nail polish pillar and the 2C-adhesive droplet surface is sufficient to avoid radiation damage to the nail polish. The FtF-bond was transferred successfully 22 min after mixing the 2C-adhesive components. The result is depicted in fig. (44). The FtF-bond has a proper size, it is centered to the axis of the pin sufficiently and the tilting is also within the limits. Thus, the sample was stored for potential measurements.

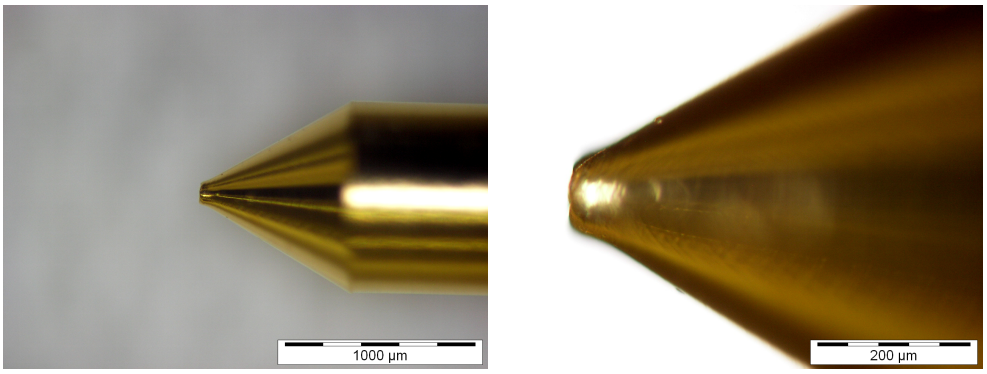

(a) Side view (5x) (b) Side view (20x)

Fig. 40: Optical microscopy images of pin-6

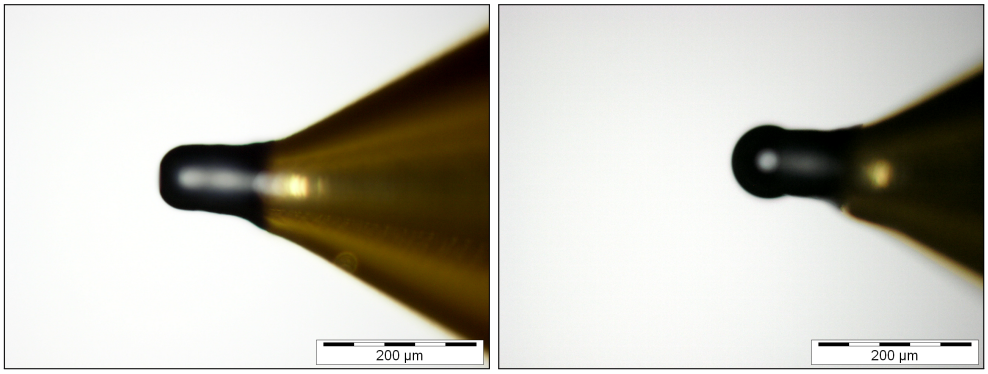

(a) Nail polish pillar (5x) (b) 2C-adhesive droplet (5x)

Fig. 41: Optical microscopy images of the nail polish pillar and the 2C-adhesive droplet

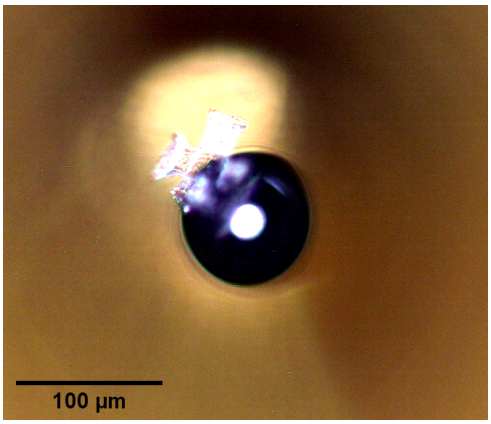

(a) Top view (20x)

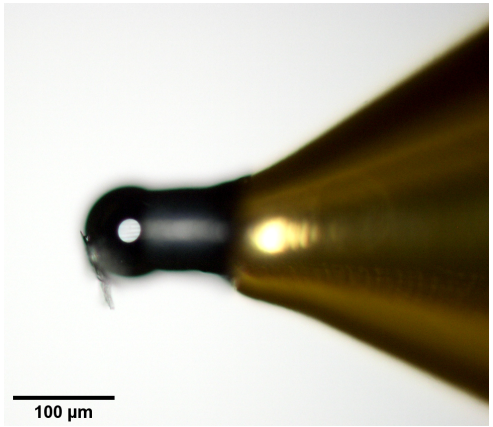

(b) Side view (20x)

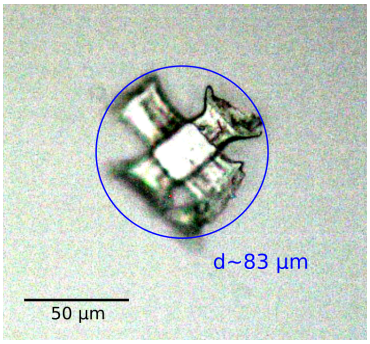

(c) FtF-bond-HC5 (20x)

Fig. 42: Optical microscopy images of hardwood FtF-bond-HC5
(a) - (b) ... FtF-bond-HC5 on pin-6
(c) ... FtF-bond-HC5 before transfer

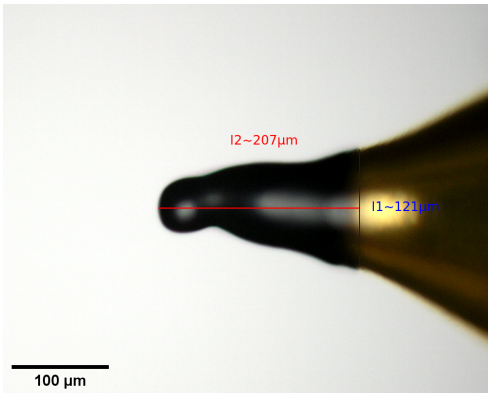

(a) Nail polish pillar (5x)

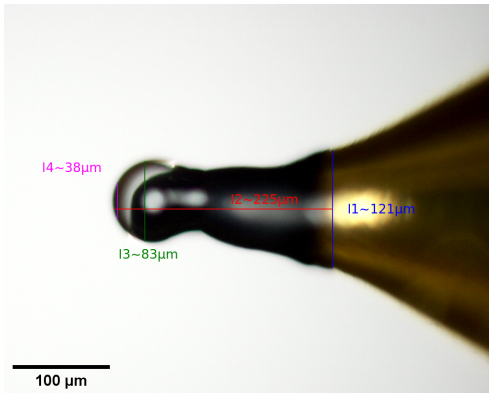

(b) 2C-adhesive droplets (5x)

Fig. 43: Optical microscopy images of the nail polish pillar and the 2C-adhesive droplets

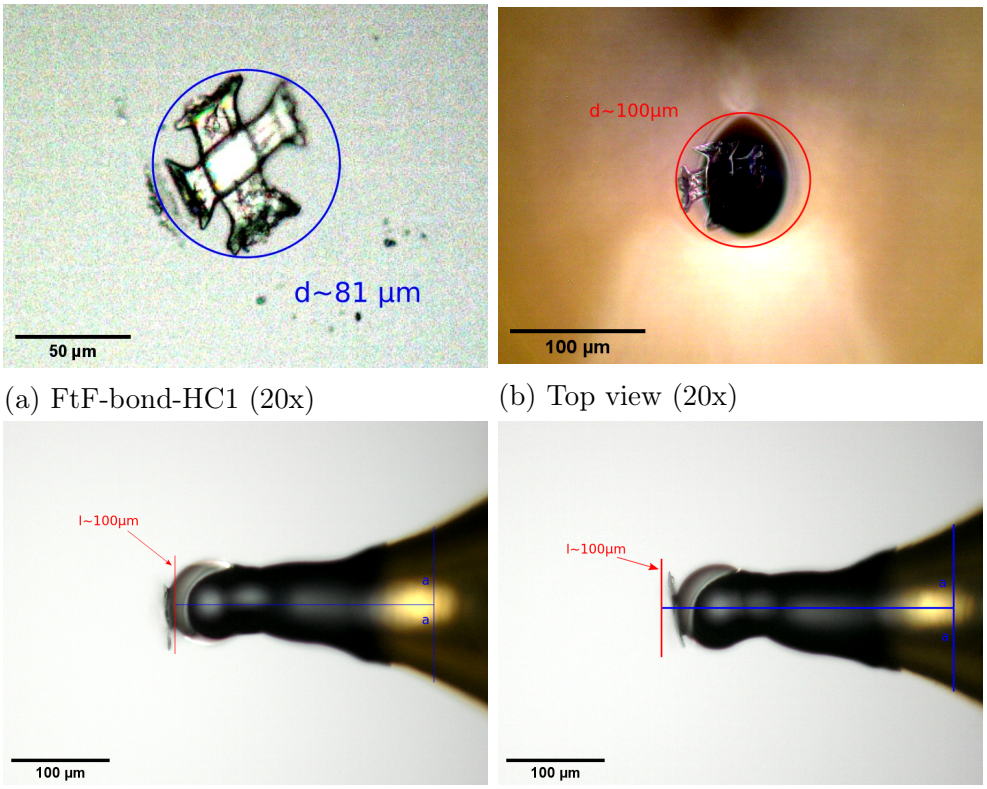

(a) FtF-bond-HC1 (20x)

(b) Top view (20x)

(c) Side view (20x)

(d) Side view (20x)

Fig. 44: Optical microscopy images of hardwood FtF-bond-HC1
(a) ... FtF-bond-HC1 before transfer
(b) - (d) ... FtF-bond-HC1 on pin-6

4.3.6 Mounting Method 5 - Upright Samples on Nail Polish on sharp Pin

To avoid irradiation of the glue, a mounting approach where the FtF-bond stands upright (see fig. (46b) & fig. (47b)), was developed. The advantage is, that the bond area is some µm away from the nail polish, so radiation damage must not be considered. Nevertheless, this method has two major downsides a priori. First of all, the stability of the sample is bad, as it is only fixed at one or two points, i.e., the arms of the fibers. Thus, the sample might start vibrating and bending during measurement, which could cause artifacts and bad ptychographic reconstructions. Secondly, the volume to measure would be increased, since the height of the scanned cylinder would be increased at about the same diameter as the flat lying sample.

To prepare the samples, pin-3 was cleaned with acetone and isopropanol and additionally, a new, not flattened pin (pin-4, see fig. (45)) was used. The pin was kept in the plastic pin holder and laid down laterally. While viewing with a microscope, the nail polish brush was brought closer to the tip of the pin and a droplet was deposited. As quickly as possible, an uncut FtF-bond was grabbed at one arm of the fiber with tweezers and then carefully pushed into to nail polish droplet. With this procedure, two samples were prepared, as depicted in fig. (46) and fig. (47).

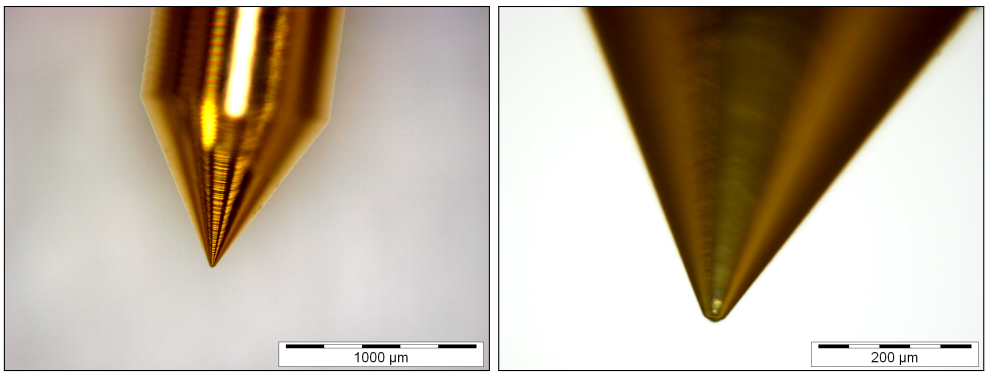

(a) Side view (5x) (b) Side view (20x)

Fig. 45: Optical microscopy images of pin-4

The FtF-bond shown in fig. (46) is attached to the nail polish droplet at two points and the bond area has a spacing of about 100 µm to the nail polish cap, so radiation damage to the nail polish would not be a problem. Furthermore, the sample shows some degree of off-centering, which could be problematic in a measurement (see fig. (46d)). Although, the main problem is the large field of view, displayed in fig. (46c). The overlaying arm of the fiber is bending downwards and thus increases the field of view for measurement, as horizontally, the whole sample has to be measured. Hence, the sample is not suitable for PXCT measurements.

For the second mounting, an FtF-bond consisting of three fibers with two separate bond areas was used (see fig. (47a)). The sample is only attached to the nail polish droplet with one fiber, making it less stable. The spacing between the bonded areas and the nail polish droplet is enough to avoid radiation damage to the nail polish (see fig. (47c)). Both bond areas are not centered to the pin axis. Again, the main problem is the increased field of view, due to the overlaying arms being nearly horizontal. Thus, also this sample

is not suitable for PXCT measurements.

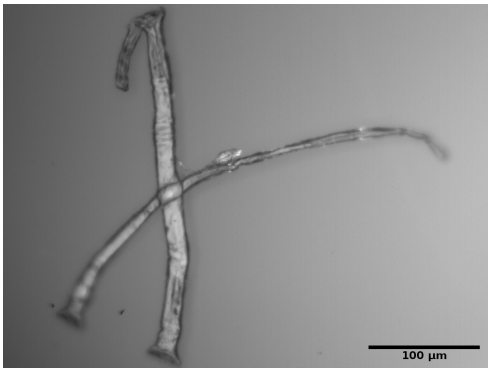

(a) FtF-bond-HW12 (20x)

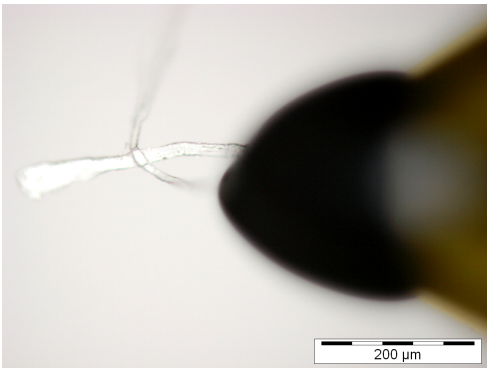

(b) Side view (20x)

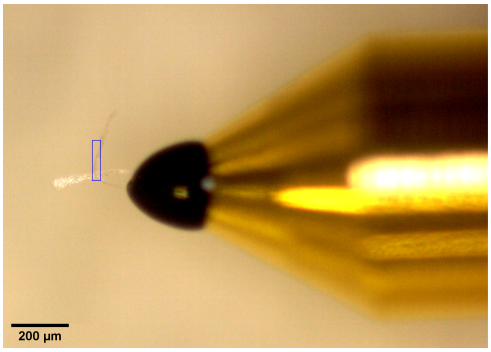

(c) Side view (5x) - Field of view

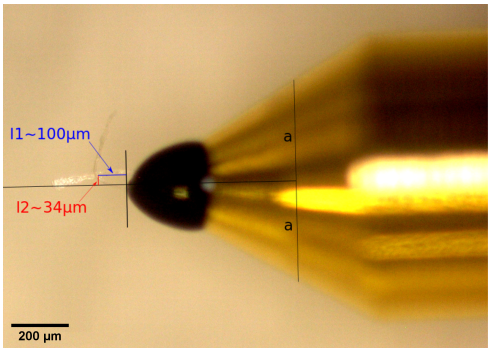

(d) Side view (5x)

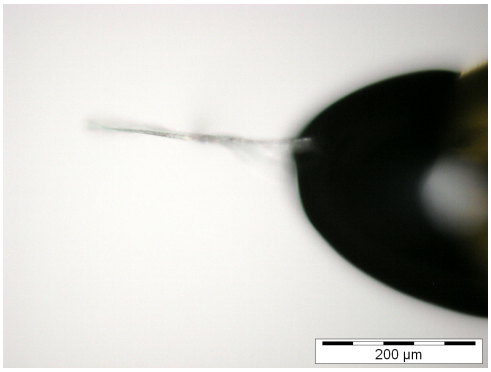

(e) Side view (20x)

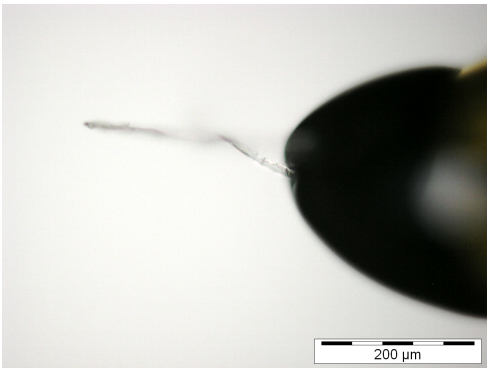

(f) Side view (20x)

Fig. 46: Optical microscopy images of hardwood FtF-bond-HW12
(a) ... FtF-bond-HW12 before transfer
(b) - (d) ... FtF-bond-HW12 on pin-3
(e) - (f) ... FtF-bond-HW12 on pin-3 imaged from an angle 90° rotated

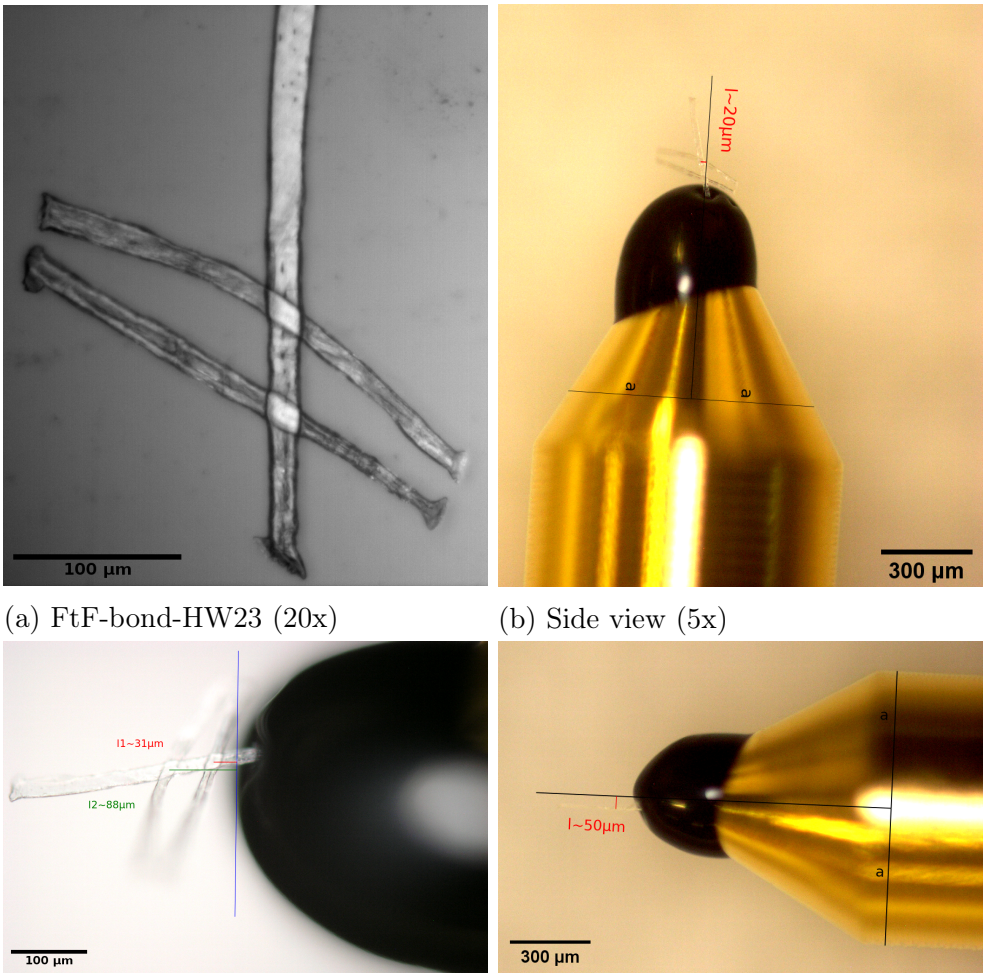

(a) FtF-bond-HW23 (20x)

(b) Side view (5x)

(c) Side view (20x)

(d) Side view (5x)

Fig. 47: Optical microscopy images of hardwood FtF-bond-HW23
(a) ... FtF-bond-HW23 before transfer
(b), (c) ... FtF-bond-HW23 on pin-4
(d) ... FtF-bond-HW23 on pin-4 imaged from an angle 90° rotated

4.4 Sample Preparation by FIB/SEM

Due to the lack of knowledge about radiation damage to nail polish and 2C-adhesive and limited measurement time, a more sophisticated sample preparation approach using FIB and SEM was performed. With those devices and a micromanipulator the preparation process may be controlled more accurately compared to the manual approach. For this approach, both soft- and hardwood fibers and two different pin types were used and in total three samples were prepared.

The first sample was prepared using a softwood FtF-bond displayed in fig. (48) and the standard OMNY pin, following subsequent procedure.

In a first step, the sample was glued to a microscope slide with silver paint using a sharpened tooth pick while viewing through a binocular. This was done by putting a droplet of silver paint on the microscope slide far away from the sample and then pulling the paint towards the sample with the tooth pick until it reached the fiber arms of the

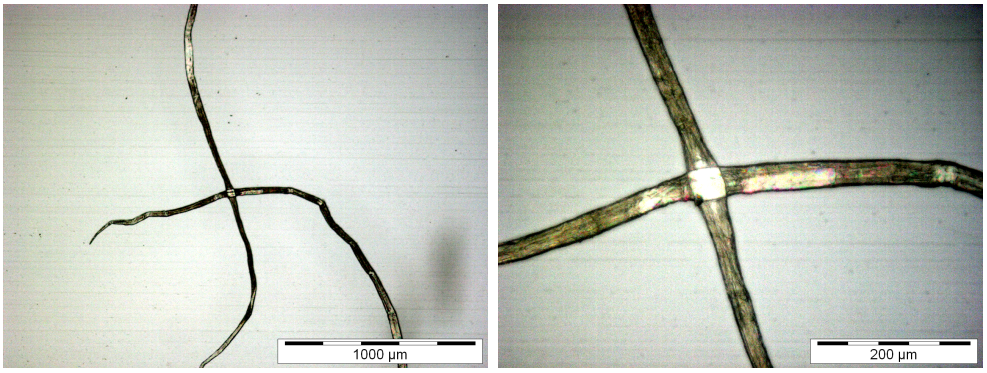

(a) FtF-bond-S12 (5x) (b) FtF-bond-S12 (20x)

Fig. 48: Optical microscopy images of softwood FtF-bond-S12

sample (see fig. (49a)). Subsequently, the paint was dried for several minutes. In the next step, the sample was coated with a carbon layer of roughly 10 nm to 30 nm thickness to prevent charging effects. After this, the microscope slide with the sample on top was transferred to the SEM chamber and oriented such that the bottom fiber lay vertically and the upper fiber lay horizontally (see fig. (49b)). In the next step, the OMNY pin was flattened with the FIB and three pillars were created on the flat surface by carbon deposition (see fig. (49c)). Subsequently, three of the four overlaying arms of the fibers were cut close to the FtF-bond edges (see fig. (49d)) and the micromanipulator was attached to the FtF-bond with carbon deposition (see fig. (49e)). The FIB gas nozzle was inserted and then the sample was transferred to the carbon pillars. To do so, the sample was slowly brought closer to the pillars until the sample was in contact with the pillars and then brought back up slightly to release stress and pressure. To fix the sample in place, carbon was deposited at different spots (see fig. (49f)). Then the micromanipulator was released and the last overlaying arm of the fiber was cut with the FIB.

The final result of the cut sample, fixed on the flattened pin, is displayed in fig. (50). The size of the cut FtF-bond is much smaller than the sizes achieved by cutting manually with a scalpel, which is advantageous in terms of scanning time. Additionally, the positioning is much more accurate and the FtF-bond is centered to the pin axis very well. Furthermore, the use of carbon instead of nail polish or glue reduces the risk of motion artifacts due to radiation damage to the nail polish or glue. The only problem that occurred is that the FtF-bond is tilted towards the flattened surface of the pin, as can be seen in fig. (50b). Hence, the spacing between the FtF-bond and the metal pin is rather small and has to be taken care of when determining the field of view for the measurement.
What was additionally observed is that some bubbles on the FtF-bond surface occurred, as evident by comparison of fig. (49b) and fig. (49d) with fig. (50). This could be due to the electrons from the SEM penetrating the FtF-bond surface, creating free radicals and in addition chemical reactions with the cellulose molecules taking place, leading to the formation of gas.

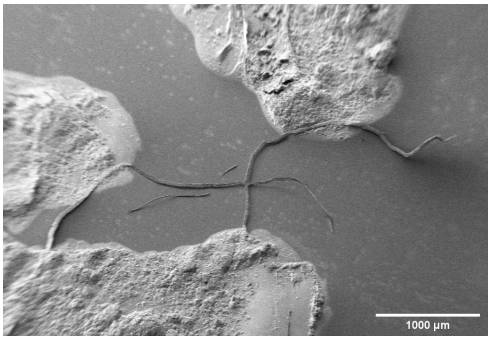

(a) FtF-bond-S12 on microscope slide, fixed with silver paint

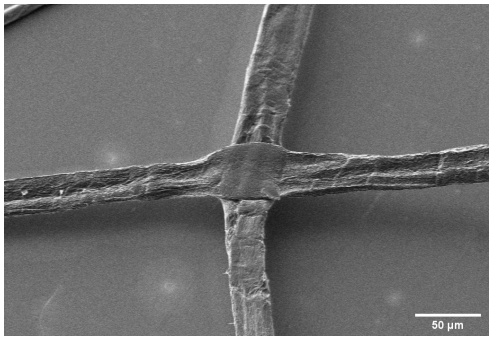

(b) Orientation of FtF-bond-S12 in the SEM

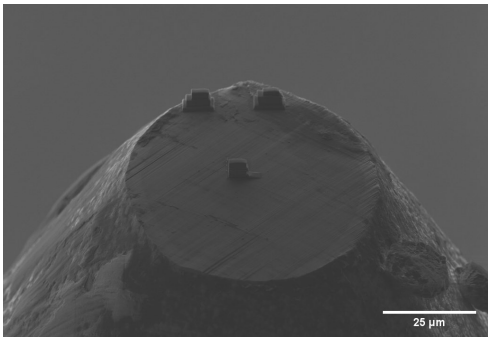

(c) Flattened OMNY pin with 3 carbon pillars

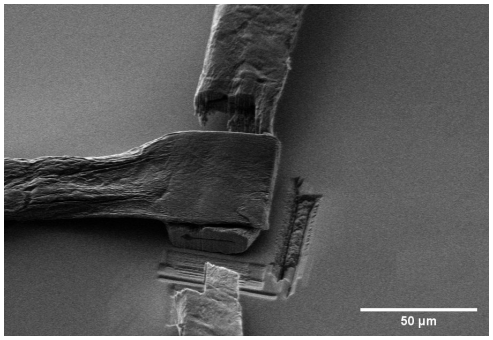

(d) FtF-bond-S12 cut with FIB at 3 sides

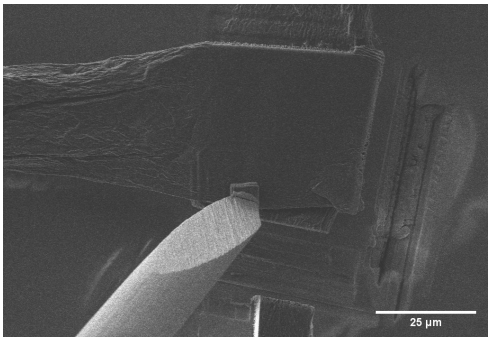

(e) Micromanipulator attached to FtF-bond-S12

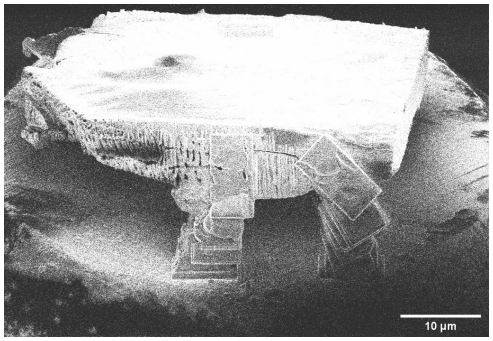

(f) FtF-bond-S12 fixed with carbon deposition

Fig. 49: Images of sample preparation process for softwood FtF-bond-S12
(a) - (e) ... SEM images
(b) ... FIB image

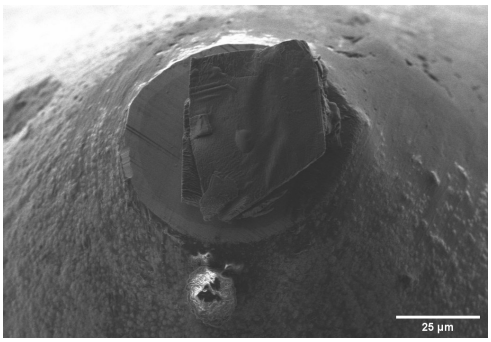

(a) FtF-bond-S12 on flattened OMNY pin

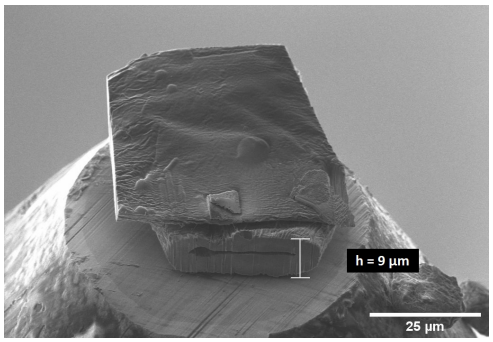

(b) FtF-bond-S12 on flattened OMNY pin

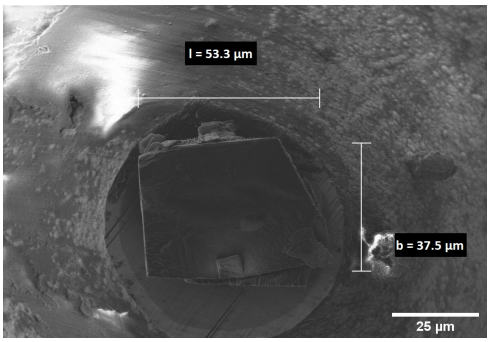

(c) FtF-bond-S12 on flattened OMNY pin

Fig. 50: SEM images of softwood FtF-bond-S12 fixed on flattened OMNY pin with carbon deposition

Two more samples were prepared for the cryo experiment. The preparation procedure was basically the same as described above, but with slight adaptions. First of all, hardwood fibers were used instead of softwood fibers due to their smaller size. Secondly, a new graphite pin was created to provide a good heat conduction from the pin to the sample, as the cooling in the cryo setup is done by cooling the pin. Additionally, the graphite does not introduce artifacts in the measurements upon X-ray irradiation, thus the sample may be mounted directly on the graphite. To create the pin, the standard OMNY pin was modified. The upper part, i.e., the tip of the pin, was removed and replaced by a piece of a graphite rod (company *Goodfellow*) with the same diameter as the OMNY pin. In the subsequent step, a high precision sample trimmer was used to create a sharp tip. One of the two graphite pins is displayed in fig. (53c) and the flattened tip is shown in fig. (51c). And finally, the micromanipulator was not attached directly on the overlapping region of the two fibers, but rather a little bit outside on the last overlaying fiber (see fig. (51e)).

The outcome of the sample preparation is displayed in fig. (52) and fig. (54) for both hardwood samples, respectively.

Sample H17 is attached to the graphite pin only at one side (see fig. (52c)), thus being probably less stable during the measurements, leading to potential artifacts and also affecting the heat conduction negatively. More contact to the pin would be beneficial for heat conduction and cooling of the sample. By comparison of fig. (51d) and fig. (52c) it stands out that again some bubbles on the surface of the FtF-bond occurred. Again, this is probably due to surface reactions between the sample and the electrons of the SEM. Apart from that, the sample is not tilted towards the pin surface, leading to a small measurement volume.

Fig. (54) shows sample H19 mounted on the tip of a graphite pin. As the surface is not flattened perfectly horizontal, the sample is tilted slightly, thus the measurement field of view would be increased. In comparison to sample H17, sample H19 lies directly on the flattened graphite surface and is attached to the pin at two sides with carbon deposition, leading to an increased heat conduction and better cooling of the sample. Furthermore, this sample does not show surface bubbles compared to sample H17. This could be due to a quicker preparation time and thus a decreased exposure to the electrons from the SEM or a thicker carbon coating as it seems to be the case when inspecting fig. (54d).

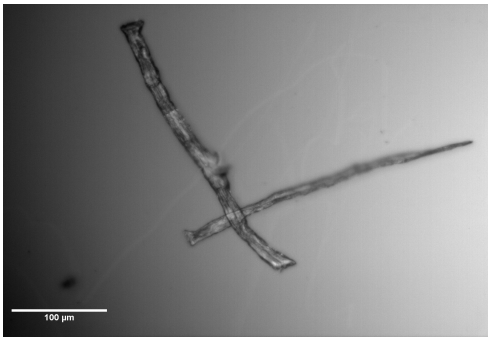

(a) FtF-bond-H17 on microscope slide (20x)

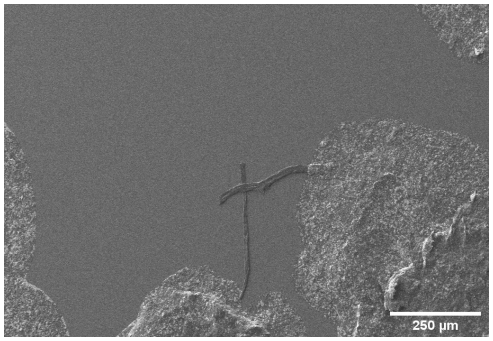

(b) FtF-bond-H17 on microscope slide, fixed with silver paint

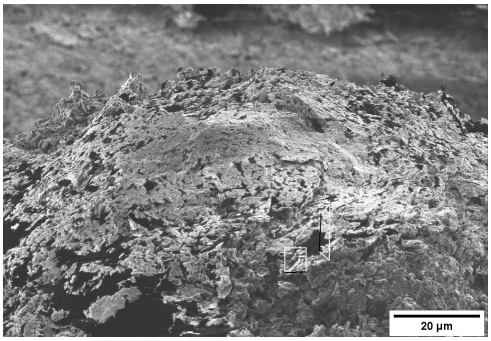

(c) Tip of graphite pin flattened with FIB

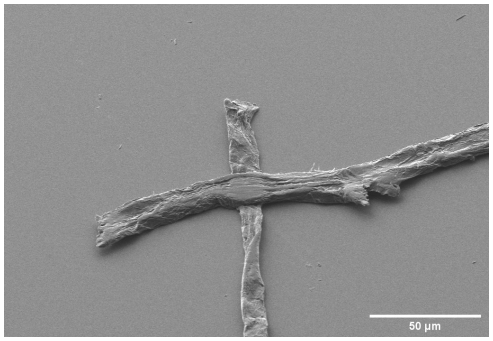

(d) Orientation of FtF-bond-H17 in the SEM

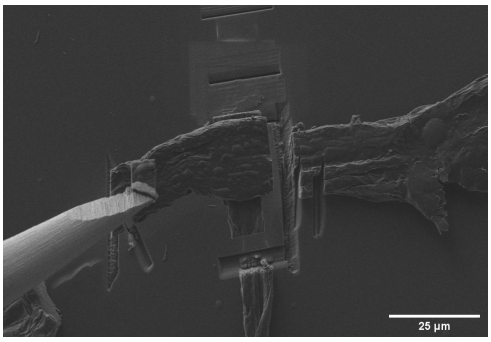

(e) Micromanipulator attached to FtF-bond-H17

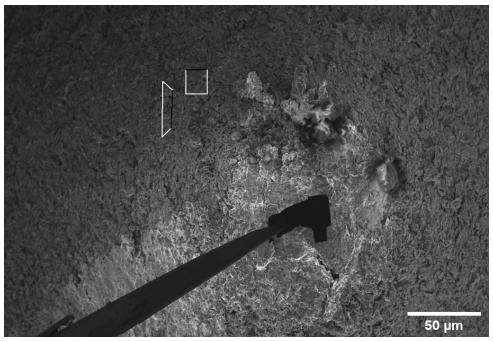

(f) FtF-bond-H17 on tip before fixation with carbon

Fig. 51: Images of sample preparation process for hardwood FtF-bond-H17
(a) ... Optical microscopy image
(b), (d) - (f) ... SEM images
(c) ... FIB image

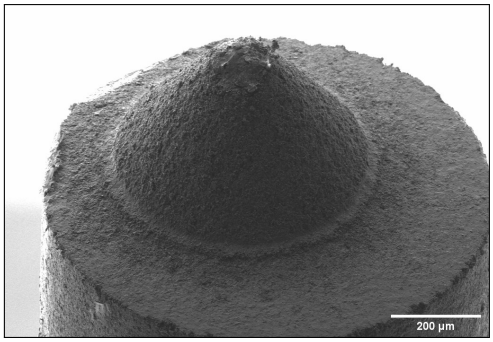

(a) FtF-bond-H17 on flattened graphite pin

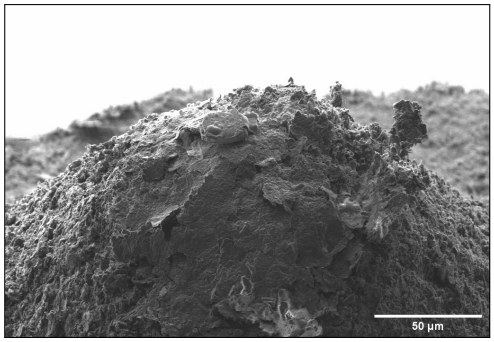

(b) FtF-bond-H17 on flattened graphite pin

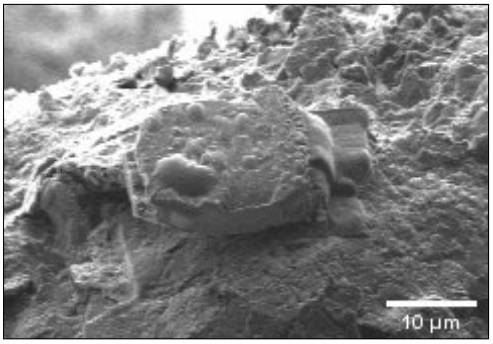

(c) FtF-bond-H17 on flattened graphite pin (close up of fig. (52b))

Fig. 52: SEM images of hardwood FtF-bond-H17 on flattened graphite pin

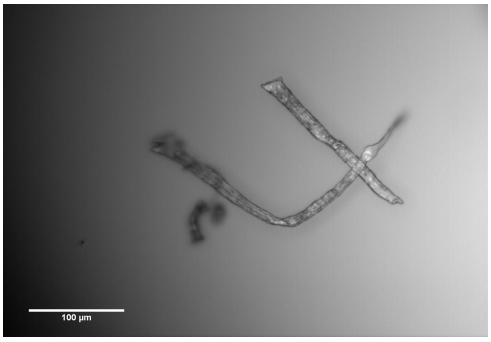

(a) FtF-bond-H19 on microscope slide (20x)

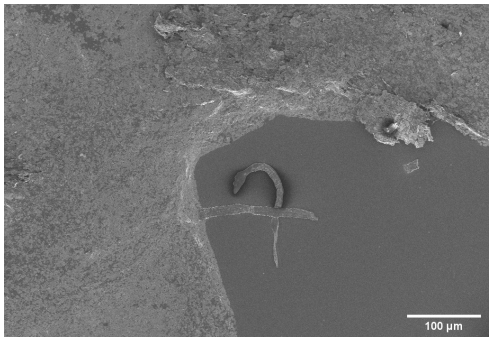

(b) FtF-bond-H19 on microscope slide, fixed with silver paint

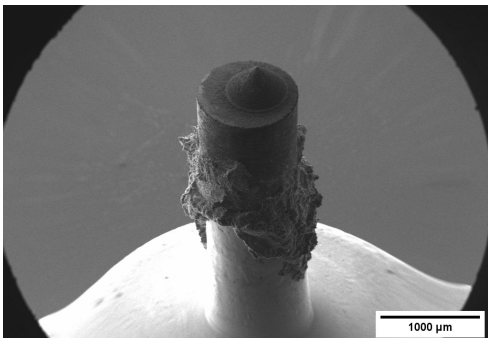

(c) Sharpened and flattened graphite pin

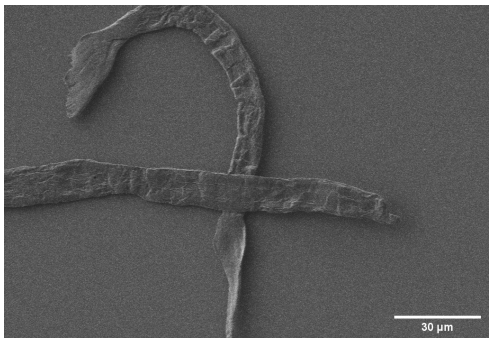

(d) Orientation of FtF-bond-H19 in the SEM

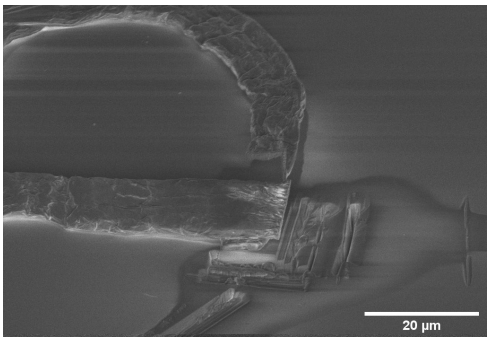

(e) FtF-bond-H19 cut with FIB at 3 sides

Fig. 53: Images of sample preparation process of hardwood FtF-bond-H19
(a) ... Optical microscopy image
(b) - (e) ... SEM images

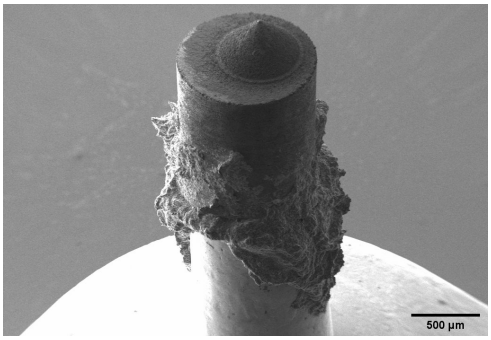

(a) FtF-bond-H19 on flattened graphite pin

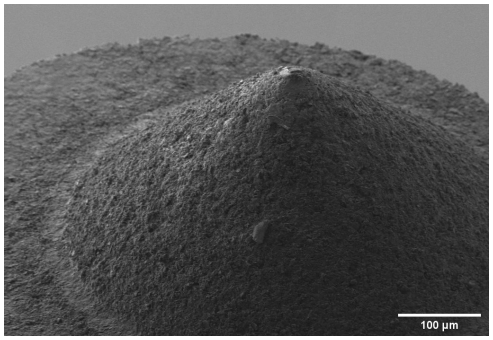

(b) FtF-bond-H19 on flattened graphite pin

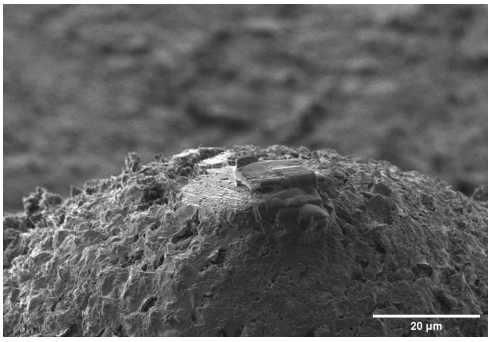

(c) FtF-bond-H19 on flattened graphite pin

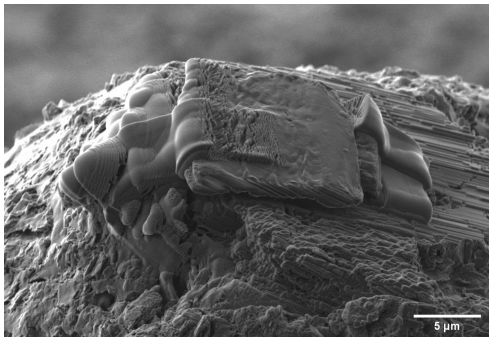

(d) FtF-bond-H19 on flattened graphite pin

Fig. 54: SEM images of hardwood FtF-bond-H19 on flattened graphite pin

5 Analysis, Results and Discussion

The main goal of this thesis is to find out whether PXCT is a suitable measurement technique for measuring FtF-bonds with high-resolution, i.e., to determine the contact area between two cellulose fibers with high accuracy. To do so, three different samples were measured at the cSAXS beamline at the SLS with two different measurement setups, one operating at ambient conditions and one operating at cryogenic conditions.

5.1 Execution of the Experiments

flOMNI Experiment The first experiment, referred to as experiment A, was performed with the flOMNI setup, operating at ambient conditions, i.e., room temperature and atmospheric pressure, using the softwood sample S12 displayed in fig. (50).

The first step was to mount the sample in the sample stage and bring it to measurement position with an automatic sample gripper. Subsequently, some test projections using an X-ray eye were made, to determine the field of view (FOV) and adjust the alignment for the rotation stage. As the sample was tilted towards the metal surface of the pin, the FOV was chosen to be smaller than the sample, to avoid X-rays passing through the metal pin. Eventually a rectangular FOV of 65 µm x 15 µm was chosen. Fig. (55b) shows the phase information of a ptychographic reconstruction from a test projection with the FOV being marked as red rectangle. The scanning points for this test projection are displayed in fig. (55a) and follow a Fermat spiral.

Since the impact of the X-rays to the FtF-bond was not known at this point, standard measurement parameters, leading to a high photon flux and radiation dose, were used. The parameters contained standard undulator settings, a photon energy of 6.2003 keV, a slit 0 size of 20 µm (see fig. (13)), an exposure time of 0.1 s for every scanning point and a step size of 2 µm between the scanning points, totalling about 240 scanning points per projection.
The detector used for the experiment was an in-vacuum single photon counting *500k Eiger* detector at a distance of about 5270 mm from the sample downstream the X-ray beam. Most of the flight path downstream the sample was evacuated to a pressure of about 10^{-4} mbar. To focus the X-ray beam, a FZP with a diameter of 170 µm, an outermost zone width of 60 nm and a focal distance of 51 mm, positioned 1.5 mm from the sample upstream the X-ray beam, was used. The resulting photon flux was about $4.2 \cdot 10^8$ photons s^{-1}.

In total 1455 projections were measured within a time of about 17 h. The first 1100 projections were performed as 8 subtomogram measurements with an angular step within the subtomograms of about 1.31°, leading to about 137 projections per subtomogram. The last 355 projections were performed as golden ratio measurements with every projection being measured from a random angle.

For every projection, a 2D ptychographic reconstruction was computed with the algorithm described in section 2.2.4 by using 500x500 detector pixels centered around the direct beam. The ptychographic reconstructions contain information about the refractive index of everything within the FOV. The real and imaginary part of the ptychographic reconstructions were saved as a matrix in a *.mat*-file. The real parts of the ptychographic

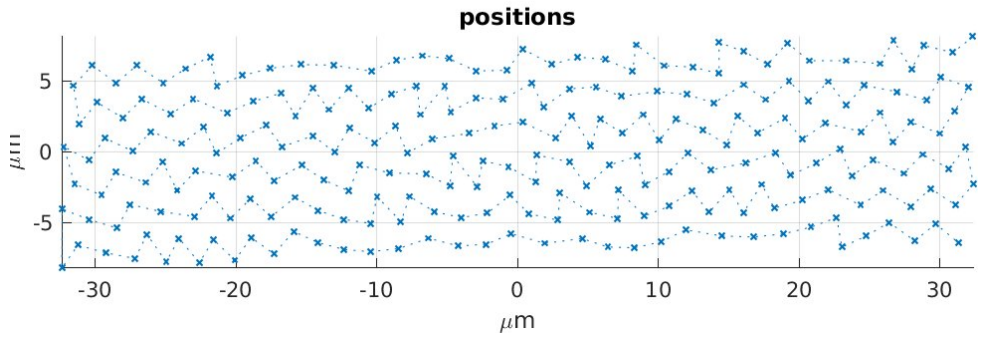

(a) Scan positions

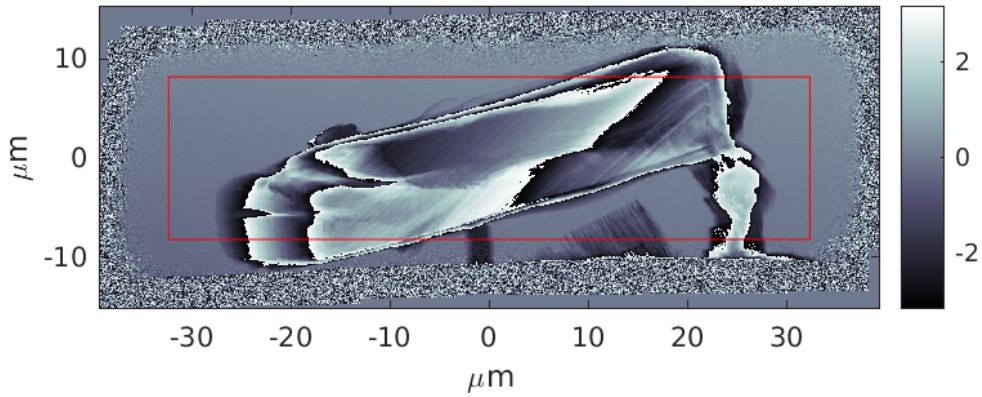

(b) Phase information of ptychographic reconstruction without phase unwrapping

Fig. 55: Scan positions and ptychographic reconstruction of a test projection of sample S12

reconstructions were used to compute 9 subtomograms with a resulting voxel size of 28.1 nm. The algorithm used for tomography was modified filtered back-projection with a Hanning filter, as described in section 2.2.5. The projection numbers, also referred to as scan numbers, used for the computation of the subtomograms, are listed in tab. (3). The subtomograms were saved as a matrix in a *.mat*-file with every entry containing the δ-part of the refractive index. Additionally, a stack of *.tiff*-files was saved with every pixel having a value proportional to the δ-part of the refractive index.

Due to the presence of radiation damage to the sample, a full tomogram containing all 2D projections was not computed, as it would have a bad resolution and contain a lot of artifacts. A detailed analysis on radiation damage may be found in section 5.3.

Tab. 3: Projections used for the computation of the subtomograms
Subtomogram ... number of subtomogram
Scan number ... scan numbers of the 2D projections used for the computation of the subtomogram
Total projections ... total number of 2D projections used for the computation of the subtomogram

Subtomogram	Scan number	Total projections
1	37 - 173	136
2	175 - 312	137
3	314 - 452	138
4	453 - 589	136
5	591 - 728	137
6	729 - 865	136
7	866 - 1003	137
8	1004 - 1140	136
9	1144 - 1492	348

OMNY Experiment Using the OMNY setup operating at a temperature of about 90 K and a pressure of about $2 \cdot 10^{-8}$ mbar, two hardwood samples were measured. The first sample was hardwood sample H17, displayed in fig. (52) and the second one was hardwood sample H19 depicted in fig. (54).

The first step was to mount both samples in the sample holder which allows for transfer into the UHV system without opening it up to atmosphere. Using an automatic sample gripper, the samples can be brought to measurement position.

For both samples, the subsequent procedure was performed. At first, some test projections using an X-ray eye were made, to determine the FOV and adjust the alignment for the rotation stage. Since horizontally, the whole sample has to be within the FOV from every angle, the FOV was chosen bigger than the sample, to be on the safe side. For the first sample (H17) a rectangular FOV of 38 µm x 6 µm was chosen and for the second sample (H19) a rectangular FOV of 36 µm x 13 µm was chosen. Fig. (56) and fig. (57) show the phase information of ptychographic reconstructions from test projections, with the FOV being marked as red rectangle for both samples. The figures also show the scanning points, following a Fermat spiral, for the test projections for both samples.

A photon energy of 6.2003 keV was used for every measurement. The detector used for all experiments was an in-vacuum single photon counting *500k Eiger* detector at a distance of about 7221 mm from the sample downstream the X-ray beam. The flight path downstream the sample was evacuated to a pressure of about 10^{-4} mbar. To focus the X-ray beam, a FZP with a diameter of 220 µm, an outermost zone width of 60 nm and a focal distance of 66 mm, positioned 3.2 mm from the sample upstream the X-ray beam, was used.

Due to the presence of radiation damage to the sample in the flOMNI experiment, the parameters for the OMNY experiments were modified to decrease the photon flux and the radiation dose. These modifications included detuning the undulator, decreasing the exposure time per scanning point, changing the amount of scanning points (step size) and decreasing the width of slit 0 in the pathway of the X-ray beam (see fig. (13)). Different settings of those parameters were examined in 4 experiments (2 experiments for every sample) to determine the optimal settings and the maximum radiation dose a sample can

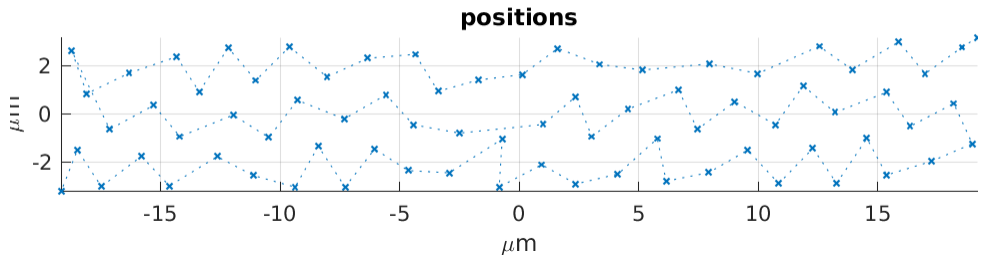

(a) Scan positions

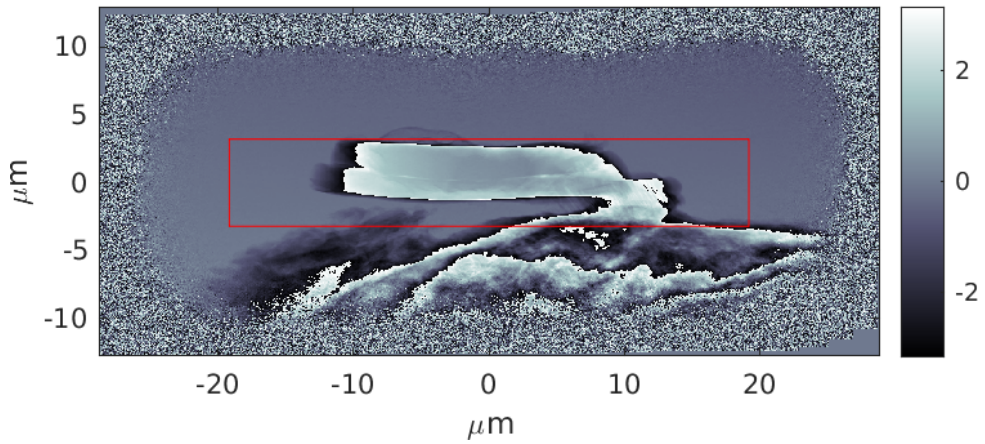

(b) Phase information of ptychographic reconstruction without phase unwrapping

Fig. 56: Scan positions and ptychographic reconstruction of a test projection of sample H17

bear. The settings are listed in tab. (4).

For every projection a 2D ptychographic reconstruction was computed with the algorithm described in section 2.2.4 by using 512x512 detector pixels centered around the direct beam. The real parts of the ptychographic reconstructions were used to compute 2 subtomograms and one full tomogram for every experiment, with a resulting voxel size of 37.6 nm. The algorithm for tomography was modified filtered back-projection, as described in section 2.2.5, with a Hanning filter for experiment C_1 and a Ram-Lak filter for experiment C_2, C_3 and C_4. Like in the flOMNI experiment, the ptychographic reconstructions were saved as *.mat*-files and the tomograms as both *.mat*- and *.tiff*-files.

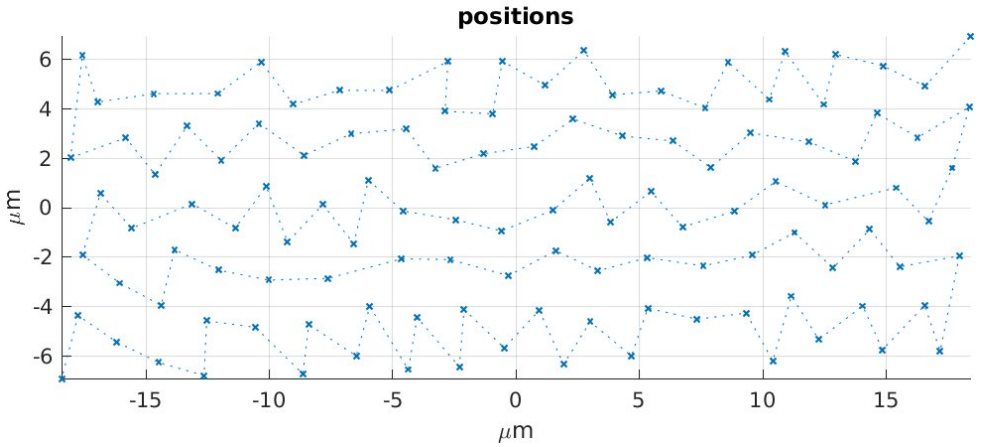

(a) Scan positions

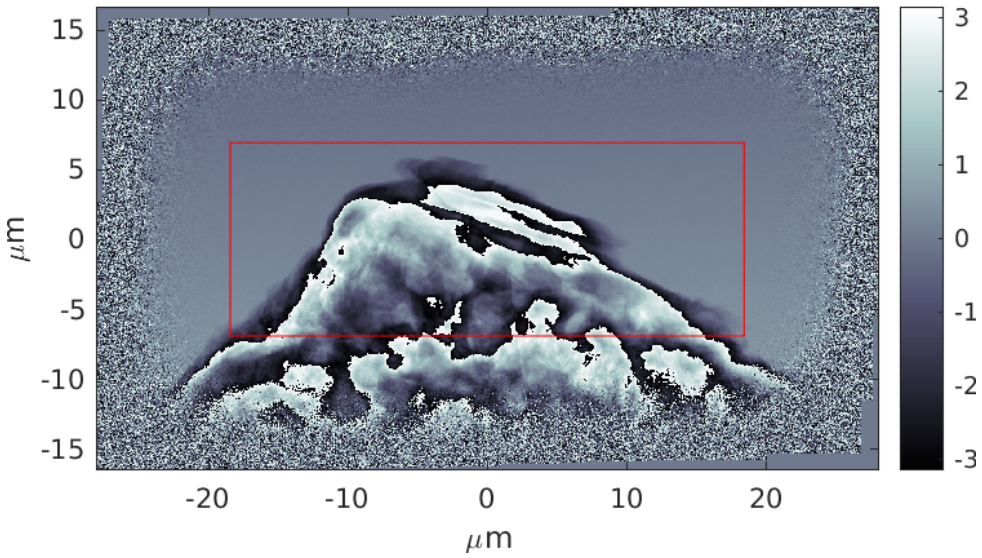

(b) Phase information of ptychographic reconstruction without phase unwrapping

Fig. 57: Scan positions and ptychographic reconstruction of a test projection of sample H19

Tab. 4: Parameters for the OMNY experiments
Exp. ... experiment identification
Sample ... sample number
Undulator ... undulator setting
S_0 ... width of slit 0 / µm
t ... exposure time per scanning point / s
d ... distance between the scanning points (step size) / µm
n_p. ... total number of 2D projections measured / -
n_{SP} ... approximate number of scanning points per projection / -
Φ ... approximate photon flux / photons s^{-1}
θ ... angular step within subtomogram / °

Exp.	Sample	Undulator	S_0 / µm	t / s	d / µm	n_p	n_{SP}	Φ / 10^8 photons s^{-1}	θ / °
C_1	H17	Detuned	10	0.025	2.0	400	60	1.7	0.90
C_2	H17	Normal	20	0.025	1.8	691	70	5.3	0.53
C_3	H19	Detuned	10	0.025	2.0	811	118	1.8	0.45
C_4	H19	Normal	10	0.025	2.0	799	118	4.1	0.45

5.2 General/Qualitative Analysis

flOMNI Experiment All the subtomograms show motion-, edge- and streak artifacts. 2D cross-sections of subtomogram 1 and subtomogram 9 are displayed in fig. (58) and fig. (59). Additionally, some bubbles formed inside the cellulose fibers, which got bigger with increasing measurement time. Furthermore, the surface bubbles, which occurred during FIB/SEM sample preparation, got bigger. All of these features indicate radiation damage and lead to bad image resolution. A further analysis on radiation damage is given in section 5.3.

Due to the artifacts and the bad resolution in the subtomograms, an RCA analysis was not conducted.

Furthermore, every subtomogram shows a connected region inside the cellulose fiber with an electron density higher than cellulose and carbon, as can be seen at the bottom of fig. (58) in black. This could be due to salt sedimentation like lime ($CaCO_3$) during the preparation process.

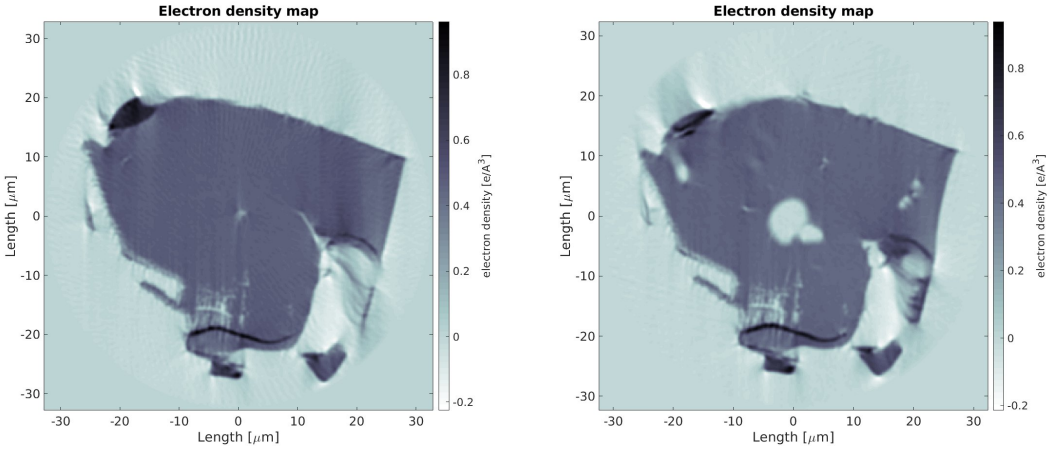

(a) Subtomogram 1 (b) Subtomogram 9

Fig. 58: Electron density maps - 2D cross-sections of the 3D subtomograms of experiment A (top view)

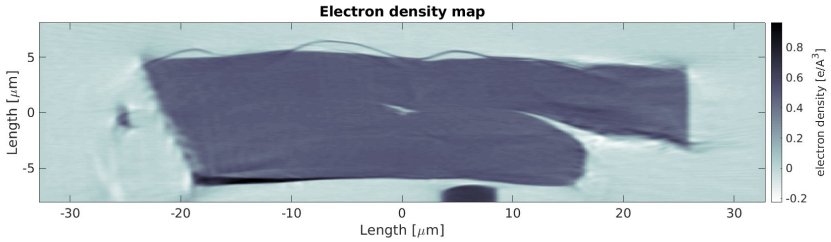

(a) Subtomogram 1

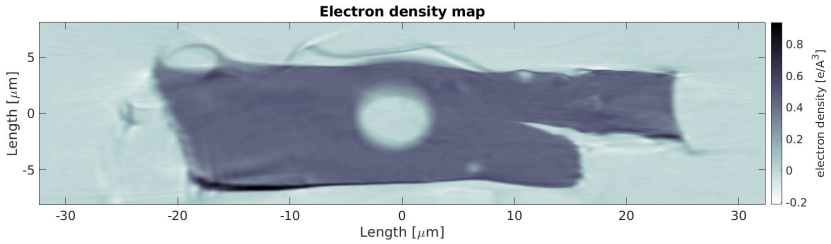

(b) Subtomogram 9

Fig. 59: Electron density maps - 2D cross-sections of the 3D subtomograms of experiment A (side view)

OMNY Experiment All the tomograms show a good resolution without artifacts, except for the tomogram of experiment C_2 (see fig. (61)). In this tomogram, edge artifacts are present, indicating radiation damage. A further analysis on radiation damage is given in section 5.3.

In the tomograms of experiment C_1, C_3 and C_4 the cellulose, the graphite and the carbon are distinguishable very well and also the contact region allows for an analysis of the RCA, which is given in section 5.5.

Taking into account that the tomogram of experiment C_4 provides a good resolution without artifacts, means that even further projections could have been measured with these settings to improve the resolution. This could be considered for future experiments.

Both samples show connected regions with high electron density within the fiber. This could again be due to salt sedimentation during the preparation process. Additionally, the tomograms of experiment C_3 and C_4 reveal some damage of one of the cellulose fibers (see fig. (60)). The edge seems to be skew compared to the rest of the fiber. This could be due to damage during the sample preparation process or the fiber being pre-damaged.

3D rendering

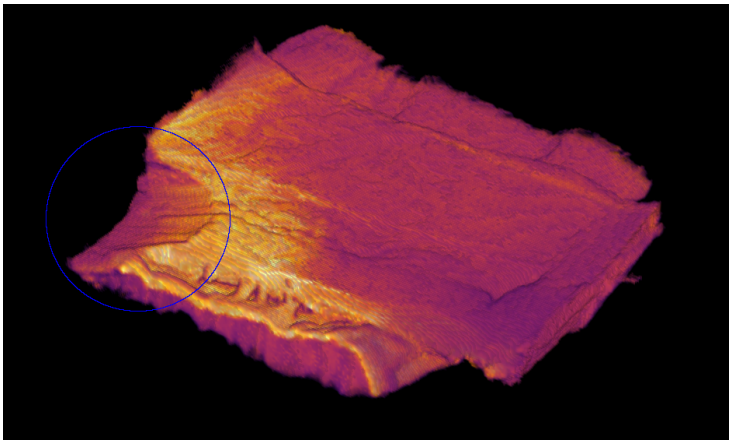

Fig. 60: 3D rendering of the tomogram of experiment C_3, showing the damaged fiber on the left side (blue circle) (pixel size 37.6 nm)

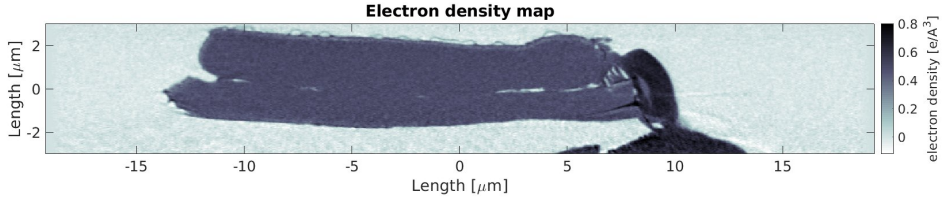

(a) Experiment C_1

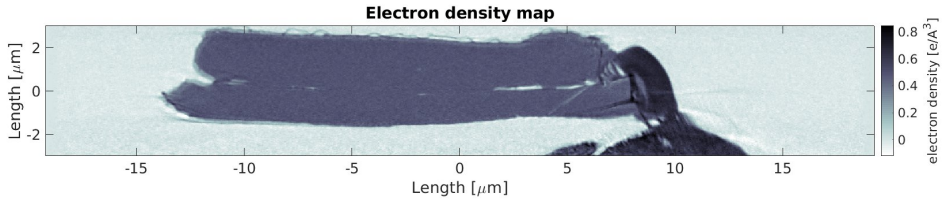

(b) Experiment C_2

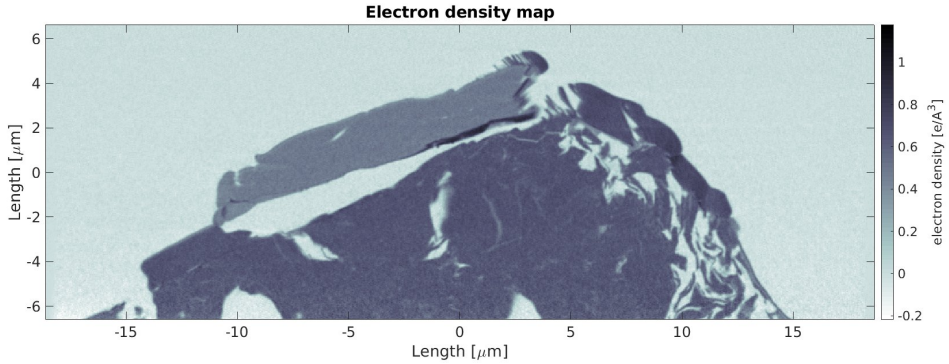

(c) Experiment C_3

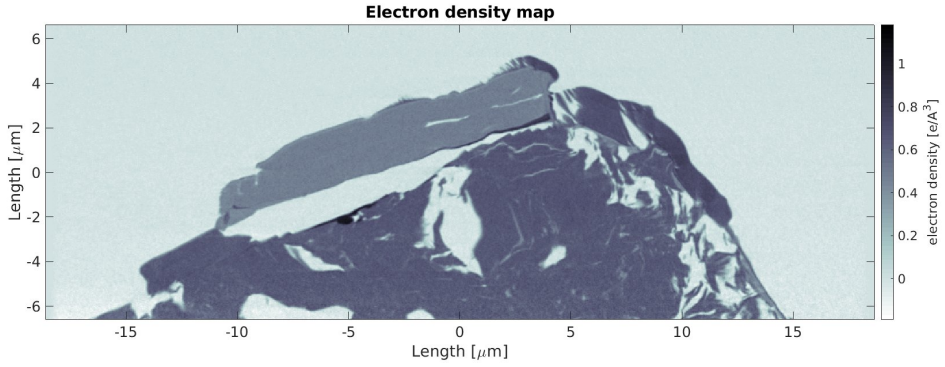

(d) Experiment C_4

Fig. 61: Electron density maps - 2D cross-sections of the 3D tomograms of the cryogenic experiments (side view)

5.3 Radiation Damage

In order to analyze the experiments concerning radiation damage, the absorbed dose in units of Gy was estimated for every tomogram and subtomogram according to eq. (41) [59]. A mass density of $\rho = 1500\,\mathrm{kg\,m^{-3}}$ and an attenuation length of 401 µm was used. The calculation of the attenuation length was done by using a web application [60] which is based on tabulated values by Henke et al. [61]. For the calculation, the chemical structure $C_{12}H_{20}O_{10}$, a mass density of $1.5\,\mathrm{g\,cm^{-3}}$ and an X-ray incidence angle of 90° was used. The absorbed doses are listed in tab. (5).

$$D = \frac{\mu \cdot I \cdot h\nu \cdot n_\mathrm{p}}{\rho} \tag{41}$$

D ... absorbed dose
μ ... linear attenuation coefficient
I ... number of incident photons per area
h ... Planck constant
ν ... X-ray frequency
n_p ... total number of 2D projections

Tab. 5: Estimation of the absorbed radiation dose by the samples
Exp. ... experiment identification
Total dose ... total dose for whole measurement in MGy
Dose subtomo ... dose per subtomogram in MGy
Dose g.r. ... dose per golden ratio subtomogram in MGy

Exp.	Total dose / MGy	Dose subtomo / MGy	Dose g.r. / MGy
A	22.00	2.09	5.30
C_1	0.43	0.22	-
C_2	3.48	1.89	-
C_3	1.19	0.60	-
C_4	3.94	1.97	-

The subtomograms of experiment A reveal, that the cellulose sample suffered a lot of radiation damage. Even the first subtomogram shows edge artifacts and streak artifacts (see fig. (58)), indicating changes in sample morphology. These changes are most probably due to radiation damage. Additionally, bubbles occurred within the fibers, which are an indication for dissociation of the cellulose molecules and the formation of certain gases. The gas bubbles are shown in fig. (62). To generate these images, the subtomograms were processed using an image processing software called *FIJI - ImageJ* [43]. Every subtomogram was segmented into two classes, using Otsu's method [42]. Class one corresponds to the background (air) and class two corresponds to cellulose and carbon. The values 0 (black) and 255 (white) were assigned to pixels belonging to class one and class two, respectively. After the segmentation, a sum projection along the z-axis was conducted, so the values of all pixels stacked on top of each other were summed. The outcome is similar to an optical microscopy image and makes the gas bubbles within the fibers clearly visible.
An explanation for the formation of gas bubbles within the fibers is that the X-ray irradiation causes the photoelectric effect and charging effects and thus, the formation of free

electrons and reactive free radicals. These free radicals can react with cellulose molecules and a depolymerization takes place [62]. Furthermore, molecular dynamics simulations by Polvi et. al. [63] suggest that in cellulose the main reactions upon ionizing radiation are chain scission (broken glucose rings) and cross linking, primarily leading to the formation of molecular hydrogen and the radicals COH_x and OH_x.

Another way to visualize the radiation damage is by inspecting a plot, gathered from the alignment process of the 2D projections for tomography. Such plots are displayed in fig. (63) for all 5 experiments. As explained in section 2.2.5, the alignment is performed with a method called vertical mass fluctuation (VMF), which assumes sample rotation around the vertical axis, parallel beam geometry and the FOV capturing the whole sample along the horizontal axis in each projection [64]. As the vertical mass distribution is independent of the rotation angle, the vertical lines in the plot should look the same for every projection, i.e., scan number, if the sample morphology does not change. Hence, all the features in the plot should stay constant over scan number. But the plot in fig. (63e) clearly shows some changes of the features, indicating changes in sample morphology and thus radiation damage.

The features in the alignment plots of experiment C_1, C_3 and C_4 are fairly constant over scan number, indicating little or no radiation damage. However, hardwood sample H17 suffered radiation damage in experiment C_2. The tomographic reconstruction shows edge artifacts, implying that the sample was not able to bear a dose of 3.48 MGy. Also, when inspecting the alignment plot in fig. (63b), slight changes of the features with increasing scan number stand out. The problem is that the sample was in contact with the pin only in a small area leading to bad heat conduction, which is disadvantageous for cooling. Nevertheless, the changes of the features are less pronounced than in the plot of experiment A, indicating that the cryogenic conditions are indeed advantageous for preventing radiation damage. This effect is called cryo-protection. It is based on the fact that the produced heat by the X-rays gets conducted away and that the produced free radicals can not diffuse to reaction partners so easily at low temperatures and thus the reaction time is much slower.
Furthermore, a comparison between the alignment plots of experiment C_2 and C_4 reveals that a bigger contact area between the pin and the sample, leading to a better heat conduction and better cooling, is beneficial for protection against radiation damage. The absorbed dose is even higher in experiment C_4, but the features in the plot in fig. (63d) stay constant, compared to the plot in fig. (63b).

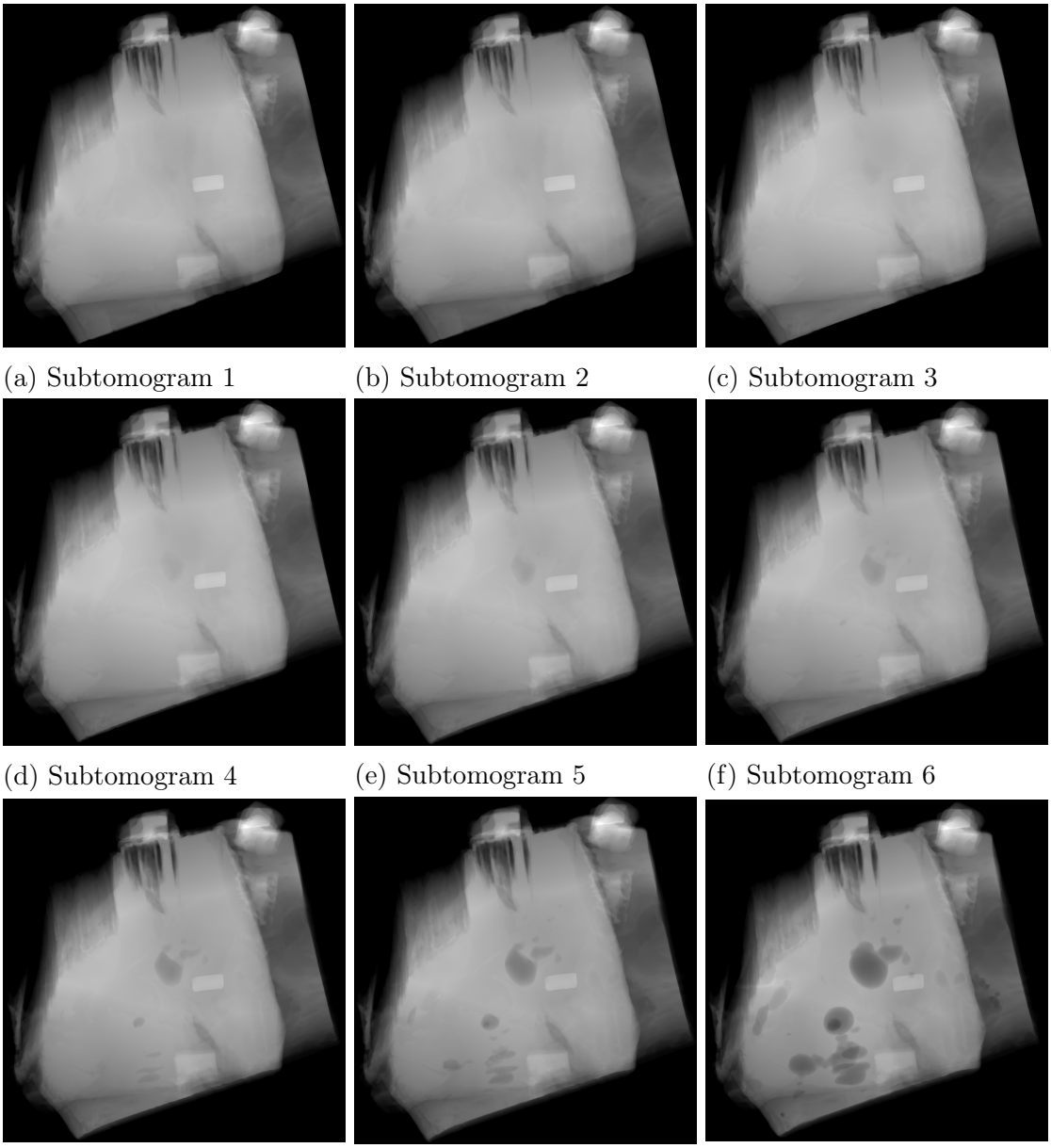

(a) Subtomogram 1 (b) Subtomogram 2 (c) Subtomogram 3

(d) Subtomogram 4 (e) Subtomogram 5 (f) Subtomogram 6

(g) Subtomogram 7 (h) Subtomogram 8 (i) Subtomogram 9

Fig. 62: Analysis of the radiation damage of softwood sample S12 in experiment A
Every subtomogram was segmented using Otsu's method [42] and then a sum projection along the z-axis was conducted

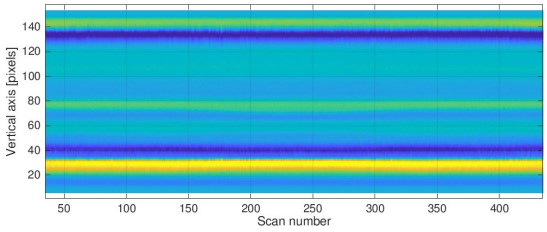

(a) Experiment C_1 (full tomogram) - 0.43 MGy

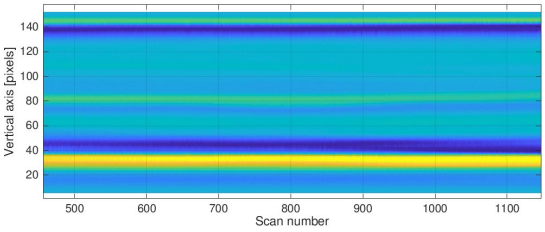

(b) Experiment C_2 (full tomogram) - 3.48 MGy

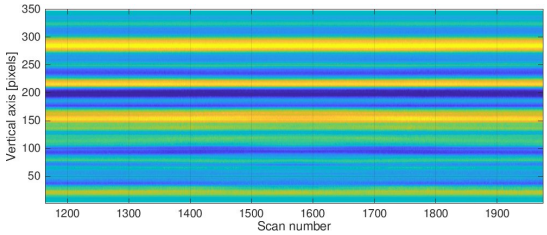

(c) Experiment C_3 (full tomogram) - 1.19 MGy

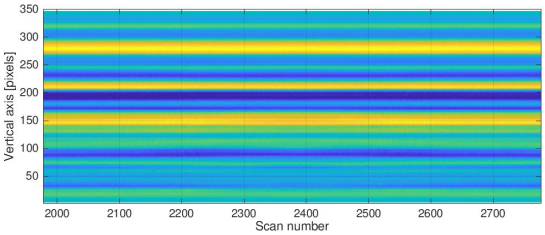

(d) Experiment C_4 (full tomogram) - 3.94 MGy

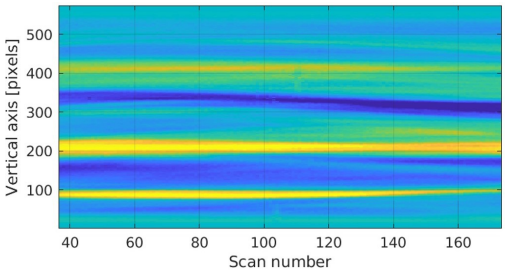

(e) Experiment A (subtomogram 1) - 2.09 MGy

Fig. 63: Plot of VMF based alignment for all experiments

5.4 Resolution Estimation

In order to be able to make statements about the quality of the tomograms, the resolution was estimated using two different methods. The first method is Fourier shell correlation (FSC) [65] and the second method is based on the edge response (ER) 10 % - 90 % criterion [66].

The FSC is a 3D generalization of the 2D Fourier ring correlation (FRC), independently introduced by Saxton and Baumeister [67], and van Heel et al. [68] in 1982. It is a measure to evaluate the similarity of two reconstructions from separate data sets that show the same object. At first, the Fourier transforms of both reconstructions, or certain parts of them, are calculated. Subsequently, these Fourier transforms are conjugate multiplied and summed over spherical shells in Fourier space. Then, the sums per shell are normalized. The FSC function is a real valued function and reads [65]:

$$\mathrm{FSC}(S) = \frac{\sum_{R=S} F_1(R) F_2^*(R)}{(\sum_{R=S} |F_1(R)|^2 \sum_{R=S} |F_2(R)|^2)^{1/2}} \tag{42}$$

S ... radius of a shell in Fourier space
$F_1(R)$ ... Fourier transform of the reconstruction with data set 1
$F_2(R)$ ... Fourier transform of the reconstruction with data set 2

The resolution may then be obtained by the intersection of the FSC function with a threshold curve $T(R)$. Van Heel and Schatz [69] proposed the 1/2-bit information threshold curve as a standard. It offers the possibility to determine at which spatial frequency a sufficient amount of information is collected in Fourier space to be able to reliably interpret the data. It is based on the signal to noise ratio (SNR) necessary to obtain a minimum of 1/2-bit information content per voxel. The 1/2-bit treshold curve reads:

$$T(R) = \frac{\mathrm{SNR} + 2/\sqrt{n(R)} \cdot \sqrt{\mathrm{SNR}} + 1/\sqrt{n(R)}}{\mathrm{SNR} + 2/\sqrt{n(R)} \cdot \sqrt{\mathrm{SNR}} + 1} \tag{43}$$

$n(R)$ ... number of voxels in the Fourier shell

$$1/2\mathrm{bit} = \log_2 \sqrt{2} = \log_2(1 + \mathrm{SNR}_{1/2\mathrm{bit}}) \tag{44}$$

$$\mathrm{SNR}_{1/2\mathrm{bit}} = \sqrt{2} - 1 \approx 0.4142 \tag{45}$$

The FSC resolution estimation was built in the *MATLAB* code for the tomographic reconstruction by the beamline scientists. The resolution estimates are listed in tab. (6) only for the tomograms without artifacts. The FSC function with the corresponding 1/2-bit threshold curve is displayed in fig. (64) exemplary for the tomogram of experiment C_1.

To additionally have a second estimate for the resolution, an ER analysis was performed. The ER criterion basically uses the length it takes for the profile of an edge to rise from 10 % to 90 % as a measure for the resolution. For this, a line profile perpendicular to an

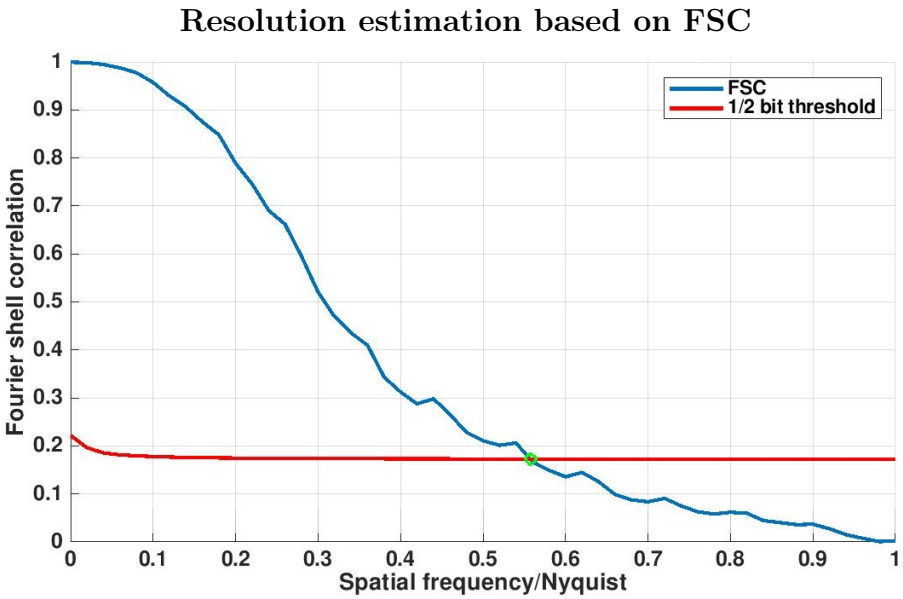

Fig. 64: Resolution estimation based on FSC for the tomogram of experiment C_1

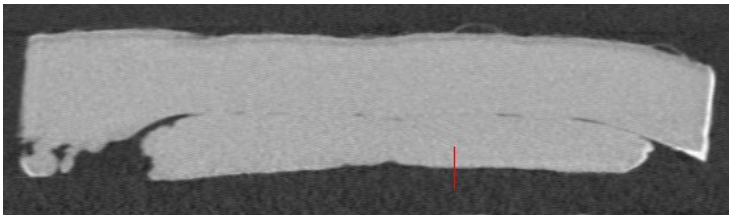

Fig. 65: 2D cross-section of tomogram C_1 (Slice 554)
The pixels where the line profile was taken are marked in red

edge of a cellulose fiber was plotted (see fig. (65)). To find the upper and lower value of the edge, the averages of 2-9 lower and 2-9 upper values close to the edge were taken, respectively (see fig. (66a)). Subsequently, the x-distance from the 10 % edge value to the 90 % edge value was calculated (see fig. (66b)), which is a measure for the resolution. The line profiles were obtained in *FIJI - ImageJ* [43] from the unprocessed reconstruction stacks, the data was saved and further calculation was performed with *MATLAB*. To have decimal values, a linear interpolation between the values of the line profile was performed (see fig. (66a)). For the tomogram of experiment C_1, 11 line profiles were taken from different x- and y-cross-sections, respectively, totaling 22 estimates for the resolution. For the tomograms of experiment C_3 and C_4, 20 line profiles were taken (10 of different x- and y-cross-sections, respectively), resulting in 20 estimates for the resolution, respectively. The averages are listed in tab. (6). The analysis was not performed for the tomograms with artifacts.

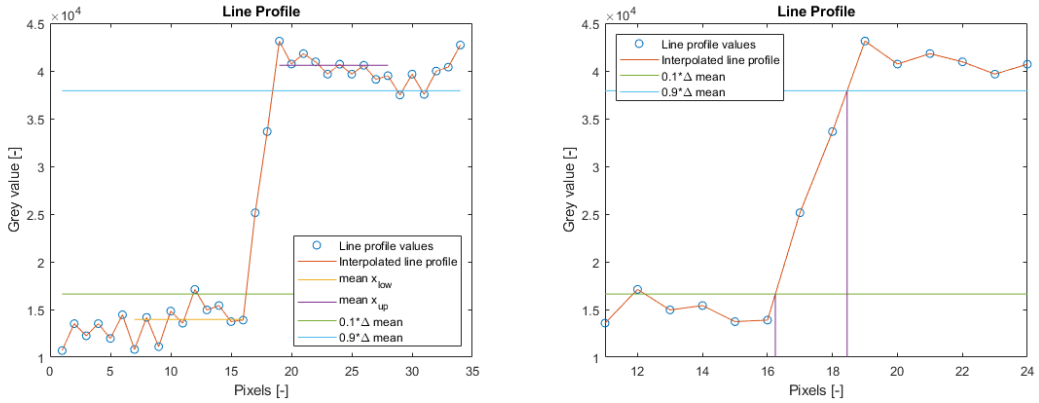

(a) Line profile and analysis (b) Smaller section of line profile

Fig. 66: Line profile of fig. (65) for the resolution estimation based on edge response criterion - the resolution estimate for this line profile is about 2.2 pixels or 83 nm

Tab. 6: Resolution estimation for the tomograms of experiment C_1, C_3 and C_4
Exp. ... experiment identification
FSC ... resolution estimation based on Fourier shell correlation / nm
ER ... resolution estimation based on the edge response 10 % to 90 % criterion / nm

Exp.	FSC / nm	ER / nm
C_1	68	77
C_3	65	89
C_4	56	81

5.5 Relative Contact Area Estimation

An estimation of the RCA was conducted for both hardwood samples using the tomographic reconstructions gathered from experiment C_1, C_3 and C_4. Image processing was done with *FIJI - ImageJ* [43] and further calculations were done with *MATLAB*. The analysis was performed similar to the procedure described in the Master's Thesis of Sormunen [15] to be able to quantitatively compare the results.

The first step for image processing was to align the fibers as shown in fig. (67). To do so, the original stack was opened in *FIJI - ImageJ* and rotated about certain axes to align the fibers. The rotation was performed by using the plugin *TranformJ Rotate* with the setting *Quintic B-Spline* for interpolation. This rotation algorithm turned out to work best, as it keeps good image quality while preserving the pixel size. Furthermore, the image stacks were cropped to the size of the cellulose fibers, to reduce the background and partly cut the carbon attachments, as only the cellulose is of interest.

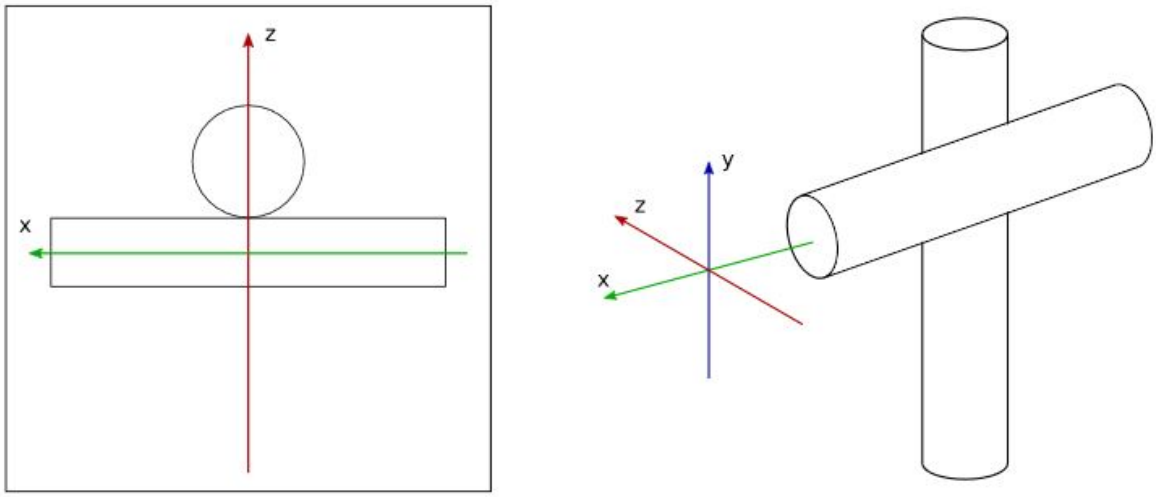

Fig. 67: Illustration of the desired coordinate system - from [15]
Left: 2D cross-section of xz-plane, later referred to y-cross-sections
Right: 3D representation of the system

Experiment C_1 As mentioned above, the first step was to rotate and crop the image stack. The result is shown in fig. (68a) for one y-cross-section.
Since only the cellulose fibers are of interest, a mask was created to get rid of the carbon attachment. To do so, a simple threshold segmentation was conducted with a threshold value of 43000. This resulted in stack cross-sections with pixel values of 255 for the background and cellulose and 0 for carbon, but as it is a simple method, some pixels were misclassified. Those pixels were set back to 255 manually. Next, the holes within the carbon clamp were filled, using the *Fill Holes* feature. The mask is depicted in fig. (68b). This mask was divided by 255 and then multiplied with the edited stack from above (see fig. (68c)). The result was cropped again to further cut the carbon attachment. Since the simple threshold segmentation did not detect all of the carbon, the remaining carbon was filled with black manually to gather a stack that only contains cellulose, background and black (see fig. (68d)).

The plugin *Trainable Weka Segmentation 3D* [41], later referred to as *Weka*-segmentation, was used to segment the stack into two classes, namely cellulose and background. The slices 330-430 of the edited image stack were partly classified manually and used as training input. In total 11096 pixels were selected as background and 10103 pixels as cellulose. The training features "Median, Hessian, Laplacian, Edges, Minimum, Mean, Variance" with a minimum sigma of 1.0 and a maximum sigma of 8.0 were used, as they turned out to show reasonable results. The classifier for the machine learning was a fast random forest with following settings: "batch size: 100, compute importances: false, debug: false, do not check capabilities: false, max depth: 0, num decimal places: 2, num features: 7, num threads: 4, num trees: 400, seed: -1687178107". The segmented image stack contains pixels with value 255 for cellulose and 0 for background (see fig. (68e)).

In order to estimate the optically overlapping area, the segmented stack was resliced to z-cross-sections. Subsequently, a sum projection was conducted, so the values of all pixels stacked on top of each other were summed. The result depicts the thickness of the fibers

and is similar to an optical microscopy image. From this image the intersection area of the two fibers was estimated, as sketched in fig. (69). This region was selected in the stack, the outside area filled with white and the stack was resliced to y-cross-sections (see fig. (71a)). From this stack, the background and holes within the fibers, not belonging to the bonded region, were removed, i.e., filled with white (see fig. (71b)). The outcome is an image stack only containing the openings in the bonded area. The whole stack was then divided by 255 and multiplied with the unsegmented stack for evaluation of accuracy (see fig. (71c)). Subsequently, the stack containing the holes in the contact region was resliced to z-cross-sections, inverted and a sum projection was conducted. The sum projection was saved for further analysis and visualization using *MATLAB*.
The sum projection was loaded in *MATLAB*, divided by 255 and multiplied with the pixel size. Hence, the value of every pixel equals the thickness of the gaps between the two fibers. This map is called the opening thickness map [15] with values zero corresponding to contact and non-zero values to non-contact. The map is displayed in fig. (72). For better visualization, the highest value was set to 20*pixel size. The intersection area of the two fibers is $(264 \pm 9)\,\mu m^2$ and the contact area is $(169.2 \pm 2.7)\,\mu m^2$. Consequently, the RCA is $(64 \pm 4)\,\%$. For verification reasons, the intersection area was also estimated using a SEM image from sample preparation (see fig. (70a)) and an optical microscopy image of the FtF-bond (see fig. (70b)). The analysis yields an intersection area of roughly $270\,\mu m^2$ for the SEM image and $210\,\mu m^2$ for the optical microscopy image. The SEM-intersection area is well within the uncertainty range of the analysis of the tomographic reconstruction, but the optical microscopy-intersection area is lower. The resolution of the optical microscopy image is not good, it seems to be out-of-focus. This could be the reason for the discrepancies.

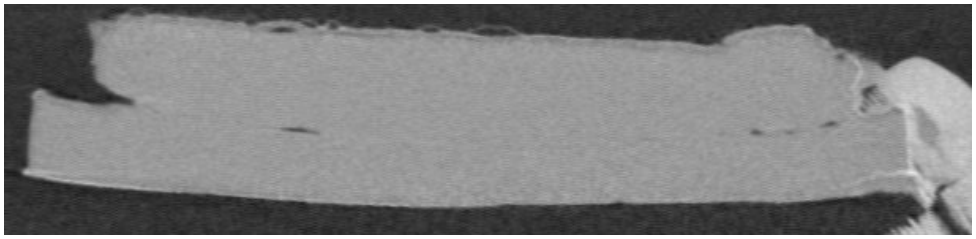

(a) 2D cross-section after rotation and cropping

(b) Carbon mask

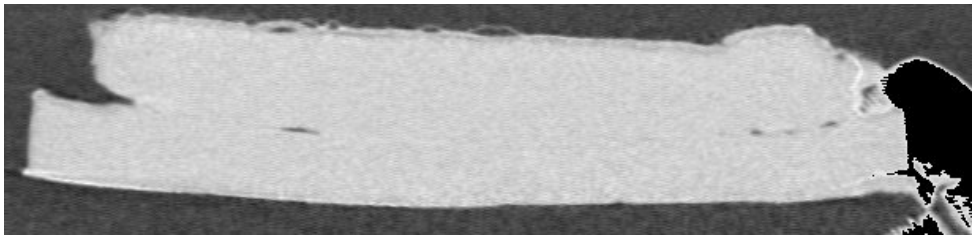

(c) Image (a) multiplied with (b)

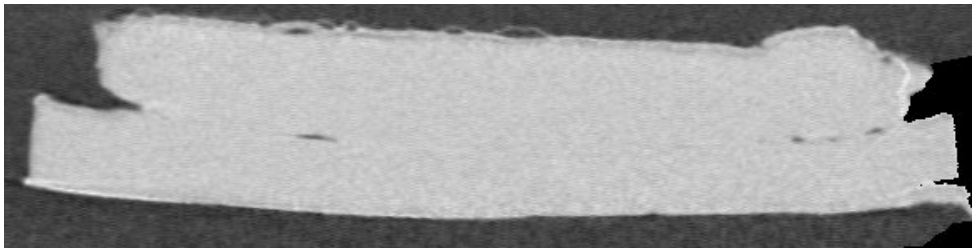

(d) Manual removal of carbon leftovers and cropping

(e) Image (d) after *Weka*-segmentation

Fig. 68: Carbon removal and result of *Weka*-segmentation illustrated for slice 233 of experiment C_1

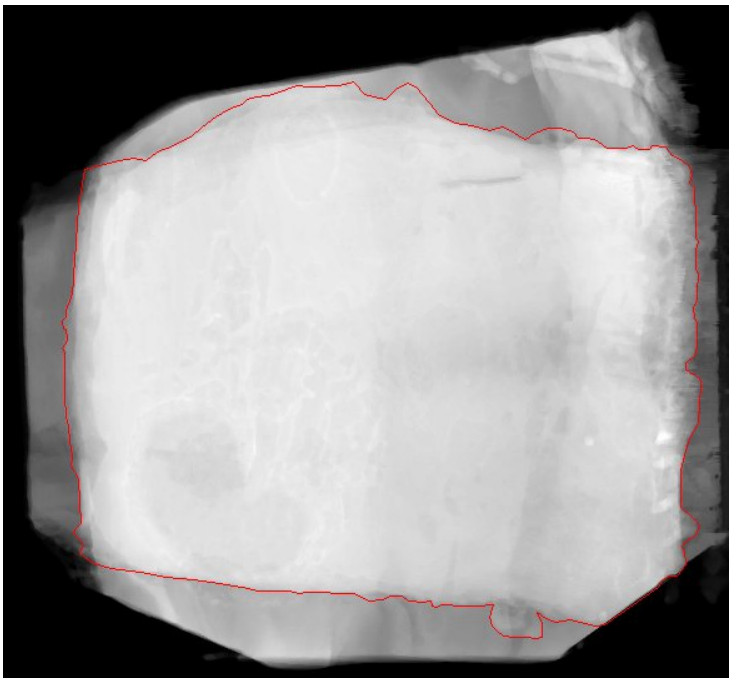

Fig. 69: Thickness image of hardwood sample H17 gathered from experiment C_1 - the overlapping area of the two fibers is marked in red

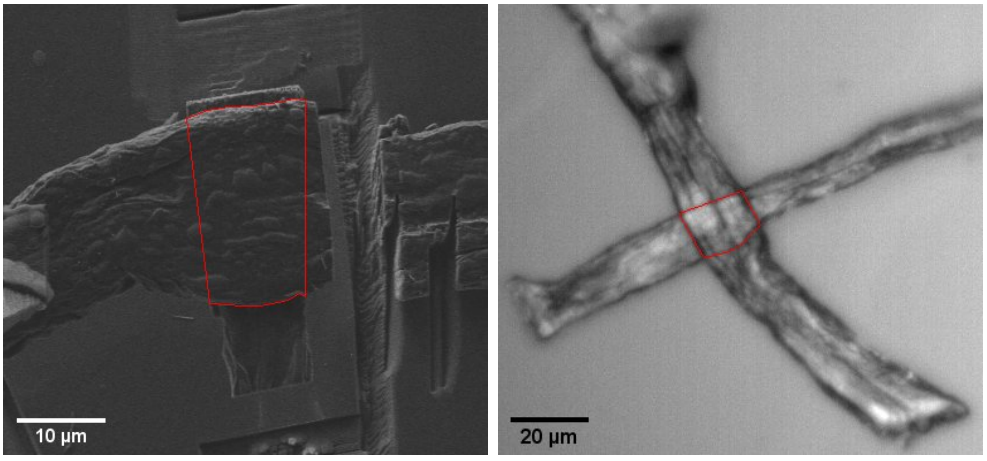

(a) SEM image (b) Optical microscopy image

Fig. 70: Verification of the overlapping area of the two fibers for experiment C_1
(a) ... SEM image of FtF-bond-H17 taken during sample preparation process with intersection area marked in red - the intersection area is approximately 270 µm^2
(b) ... Optical microscopy image of FtF-bond-H17 taken after bond preparation with intersection area marked in red - the intersection area is approximately 210 µm^2

(a) Sides filled with white

(b) Removal of background

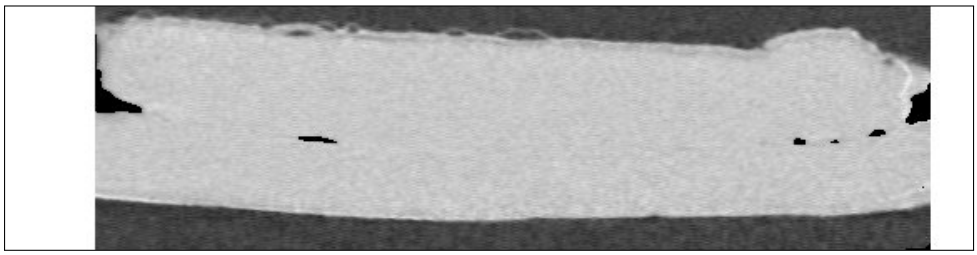

(c) Verification of accuracy

Fig. 71: Background removal and accuracy verification illustrated for slice 233 of experiment C_1

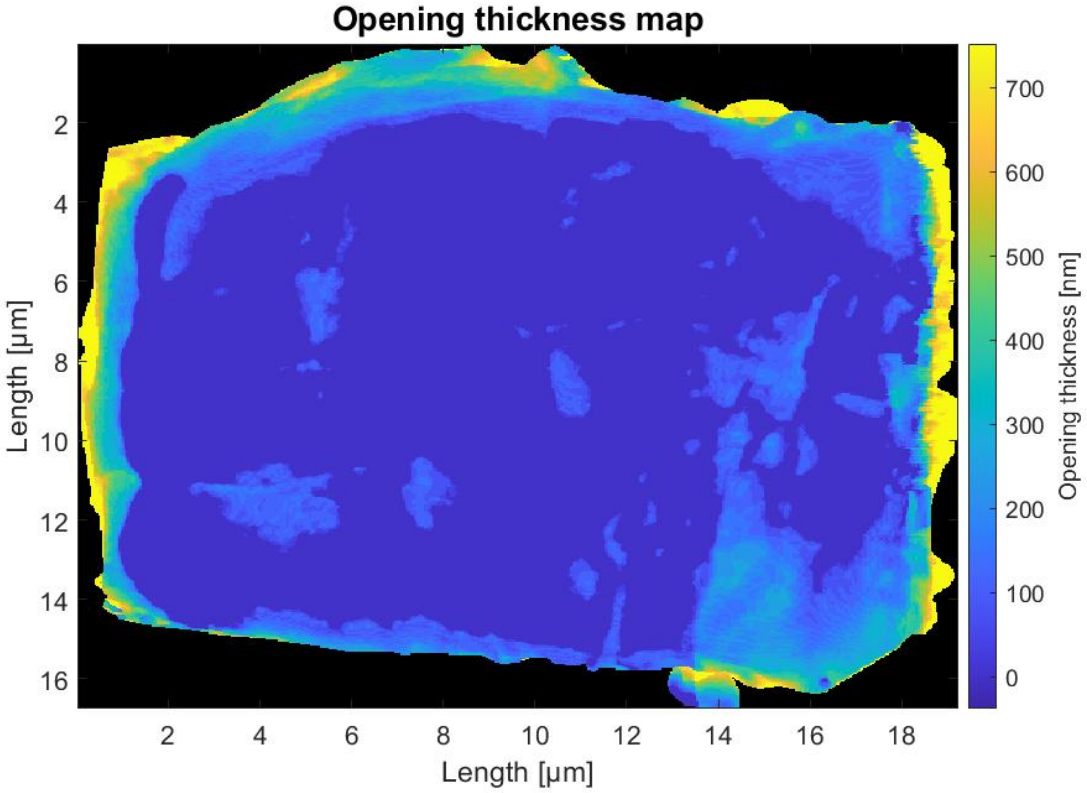

Fig. 72: Opening thickness map of hardwood sample H17 gathered from experiment C_1
The uncertainty of the opening thickness is ±6 %

Experiment C_3 For the analysis, basically the same procedure as above was conducted. The only differences were the way of carbon removal and the settings for the *Weka*-segmentation [41] for detecting the holes in the contact region.

The carbon removal was not done by simple threshold segmentation, but by *Weka*-segmentation. To do so, two classifier models were created for the left and the right carbon clamp, respectively. Those classifiers were then used to segment the particular side of the image. Again manual adjustments had to be done to reset misclassified pixels and remove the carbon leftovers.

The differences in the *Weka*-segmentation, to detect the non-contact regions between the two fibers, were as follows: Instead of two, the segmentation included three classes, namely cellulose, background and salt sedimentation. The training was done on a small, representative sub-volume of the whole stack. In total 753 pixels were selected as background, 680 pixels as cellulose and 848 pixels as salt sedimentation. The standard training features "Mean" and "Variance" with a minimum sigma of 1.0 and a maximum sigma of 8.0 were used, as they also turned out to show reasonable results. The classifier for the machine learning was again a fast random forest, but with slightly different settings: "batch size: 100, compute importances: false, debug: false, do not check capabilities: false, max depth: 0, num decimal places: 2, num features: 2, num threads: 4, num trees: 200". The seed was not documented.

The thickness image, i.e., the sum projection along the z-axis of the segmented stack, and the corresponding opening thickness map are shown in fig. (73) and fig. (75), respectively. As stated in section 5.2 and depicted in fig. (60), the FtF-bond was partly damaged in one corner. This is also visible in the thickness image. Thus, the upper right part of the FtF-bond was excluded from the overlapping area and the RCA calculation. The analysis yields an intersection area of $(109 \pm 6)\,\mu m^2$ and a contact area of $(71.9 \pm 2.0)\,\mu m^2$, resulting in a RCA of $(66 \pm 6)\,\%$. Again, for verification of the intersection area, a SEM image from sample preparation and an optical microscopy image of FtF-bond H19 were analyzed (see fig. (74)). The resulting intersection area for both images is $115\,\mu m^2$ which is within the uncertainty range of the intersection area analysis using the tomographic reconstruction. The higher value is reasonable, since a part of a corner (damaged fiber) was excluded from the analysis.

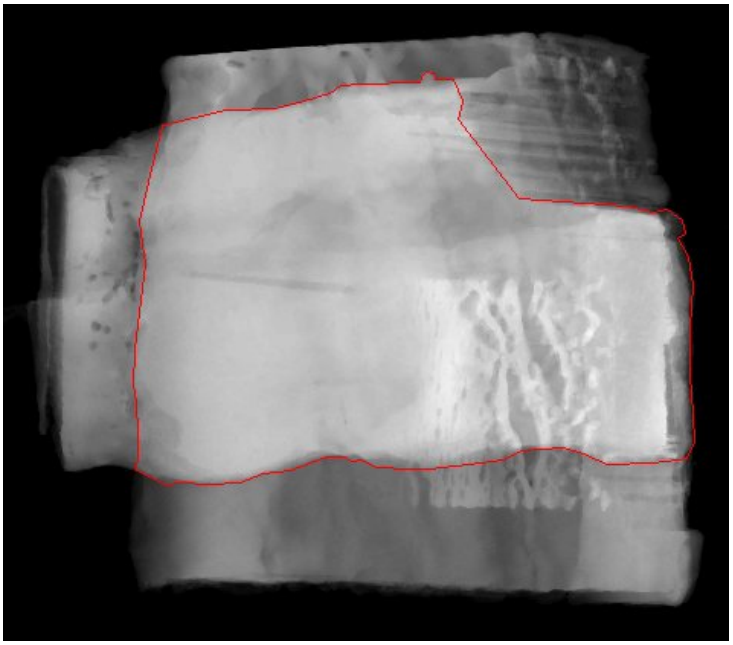

Fig. 73: Thickness image of hardwood sample H19 gathered from experiment C_3 - the overlapping area of the two fibers is marked in red
The upper right part of the FtF-bond was excluded due to a damaged fiber

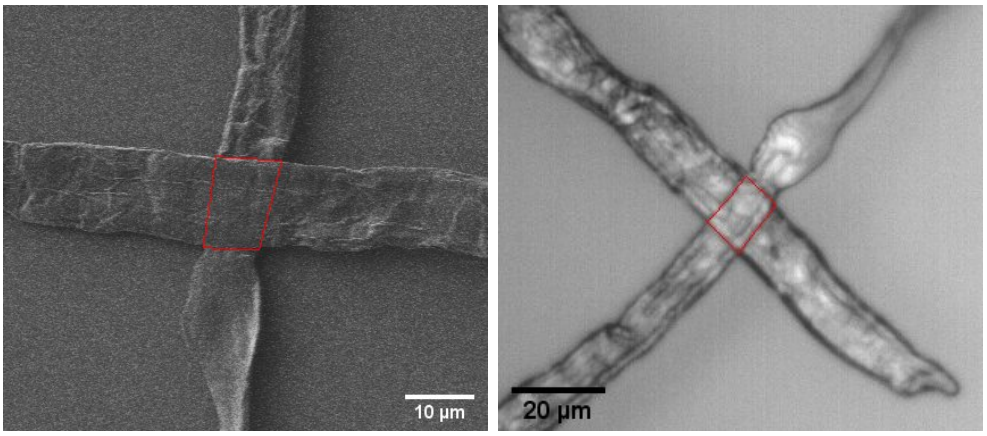

(a) SEM image (b) Optical microscopy image

Fig. 74: Verification of the overlapping area of the two fibers for experiment C_3
(a) ... SEM image of FtF-bond-H19 taken during sample preparation process with intersection area marked in red - the intersection area is approximately 115 µm^2
(b) ... Optical microscopy image of FtF-bond-H19 taken after bond preparation with intersection area marked in red - the intersection area is approximately 115 µm^2

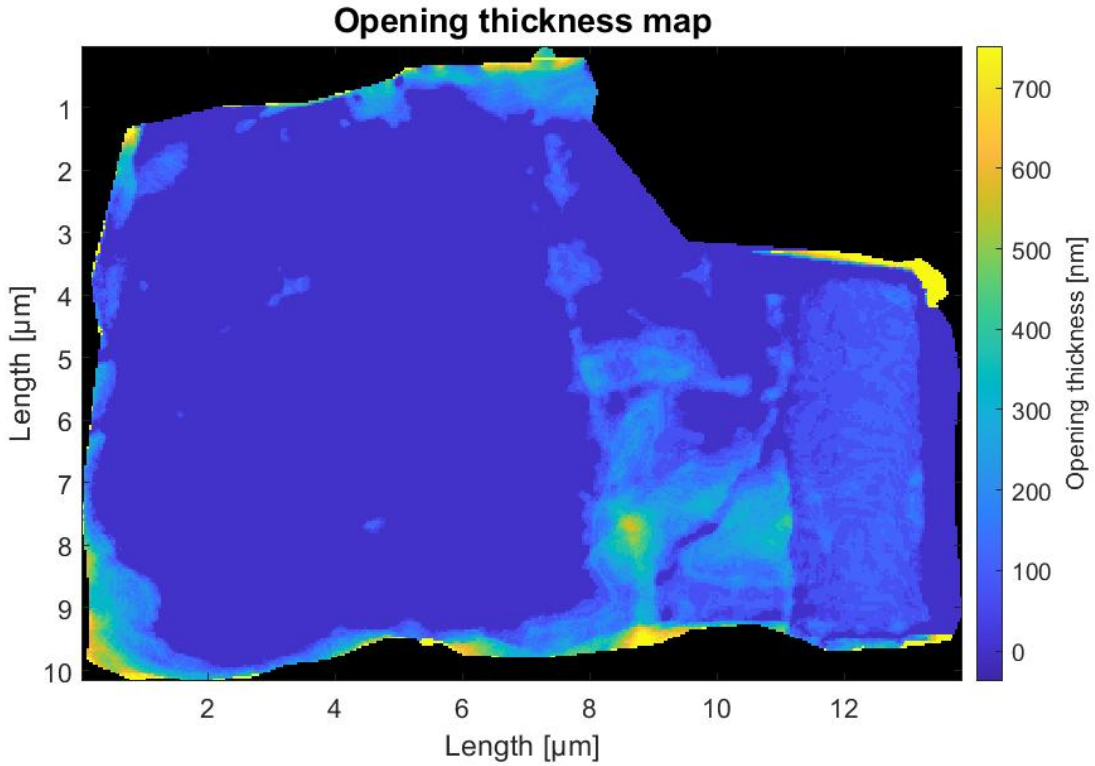

Fig. 75: Opening thickness map of hardwood sample H19 gathered from experiment C_3
The uncertainty of the opening thickness is ±8 %

Experiment C_4 Again, the analysis was performed in a similar fashion as described for experiment C_1 with the only difference in the procedure of carbon removal.

This time, the *Weka*-segmentation [41] was conducted only once, with one classifier model for the whole system that detects the small non-contact regions between the fibers as well as the carbon attachments. To do so, the slices 146-225 were partly classified manually with the classes cellulose, background and carbon. In total, 16138 pixels were selected as cellulose, 18108 pixels as background and 16737 pixels as carbon. The same training features, as for experiment C_1, were used. Also, the same settings were used for the classifier, except for the seed which was -1369382577. The outcome is shown in fig. (76b) with cellulose in red, background in green and carbon in pink. In order to obtain a thickness image, the carbon and the background were set to black and the cellulose to white (see fig. (76c)). Additionally, the carbon leftovers were set to black manually (see fig. (76d)). The thickness image was then obtained by a sum projection along the z-axis and is displayed in fig. (77). The overlapping area was copied to the segmented stack and only the openings in the bonded region were left. The opening thickness map was then created in the same way as explained for experiment C_1 and is depicted in fig. (78). The resulting intersection area is $(105 \pm 6)\,\mu m^2$ and the contact area is $(68.6 \pm 1.8)\,\mu m^2$. Consequently, the RCA is $(65 \pm 6)\,\%$. The intersection area is a little bit lower than in experiment C_3, but within the uncertainty range. Also the contact area is a little bit lower, which can be explained by the fact that the tomogram-resolution of experiment C_4 is better than C_3 and thus, smaller gaps between the fibers may be resolved, leading to potential changes in contact area and RCA. Nevertheless, the RCA is almost the same as

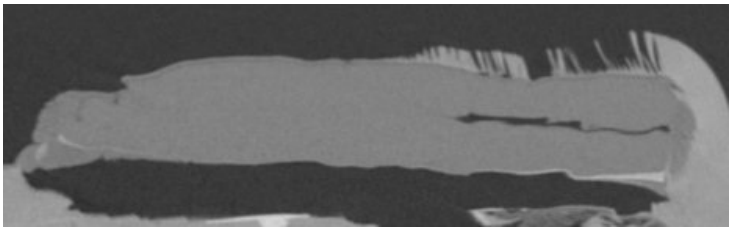

(a) 2D cross-section after rotation and cropping

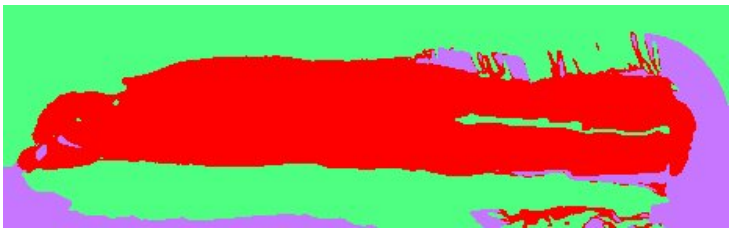

(b) 2D cross-section after segmentation

(c) Removal of carbon

(d) Manual removal of carbon leftovers

Fig. 76: Carbon removal and result of *Weka*-segmentation illustrated for slice 228 of experiment C_4

in experiment C_3, which indicates that the result is reliable, as the segmentations were done independently with different data-sets and different settings.

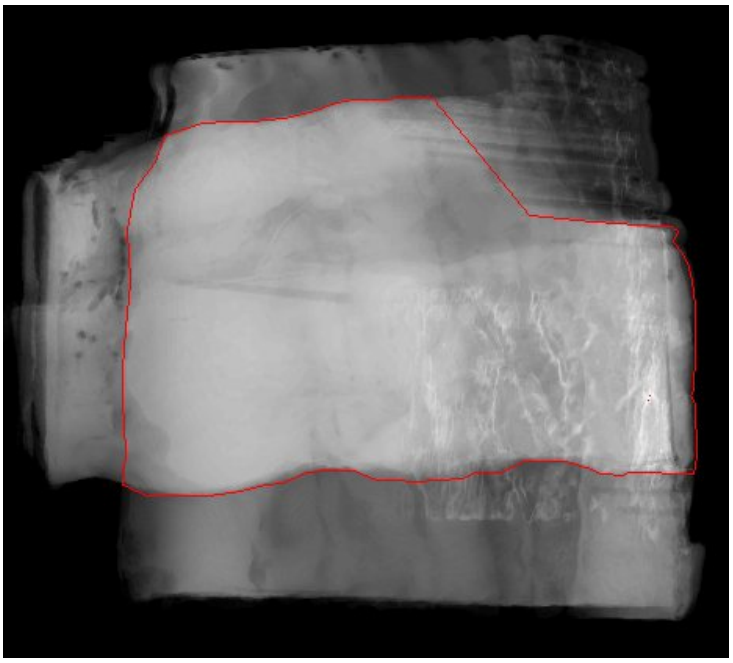

Fig. 77: Thickness image of hardwood sample H19 gathered from experiment C_4 - the overlapping area of the two fibers is marked in red
The upper right part of the FtF-bond was excluded due to a damaged fiber

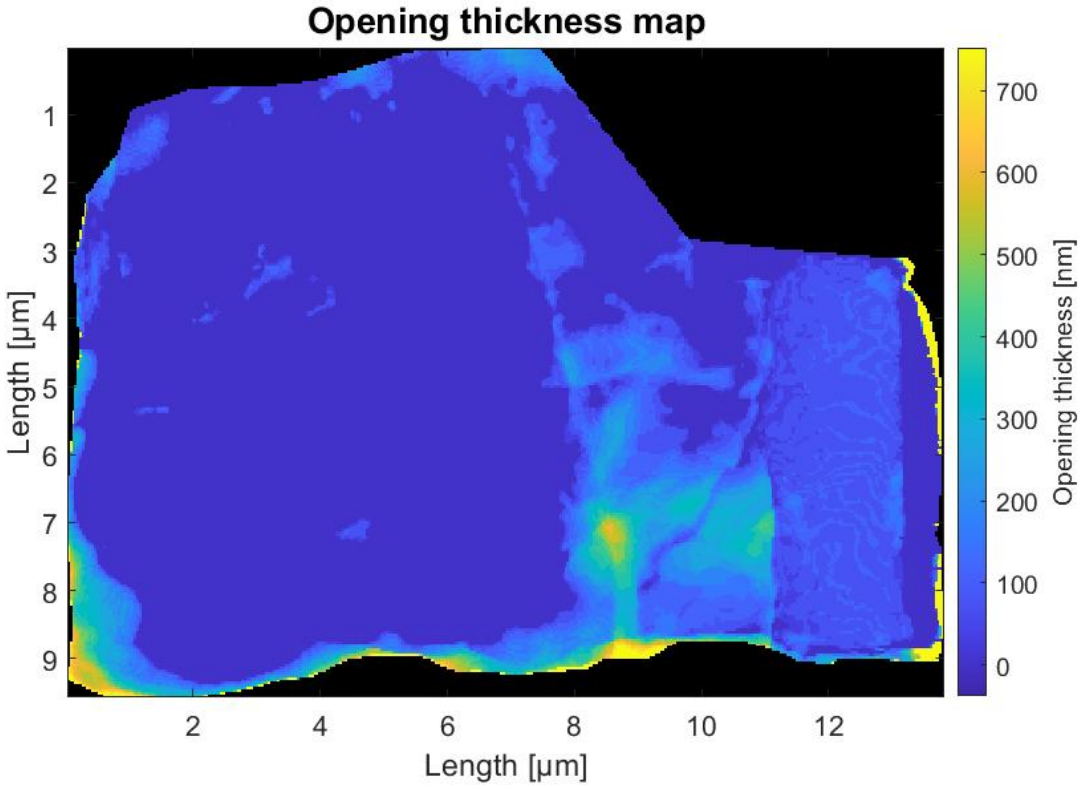

Fig. 78: Opening thickness map of hardwood sample H19 gathered from experiment C_4
The uncertainty of the opening thickness is ±6 %

Uncertainties The RCA is the ratio of two quantities, namely the intersection area of the two fibers and the contact area between the two fibers. Both of these quantities are erroneous, but an exact quantification of the errors is difficult, as the analysis is based on visual evaluation and image segmentation. For the uncertainty of the intersection area, a simple min-max method, like in the work of Sormunen [15], was performed. This method accounts for inaccuracies in manual determination of the overlapping area and errors in determination of the boundary between the carbon and the cellulose. For this, a mask was created from the overlapping area image, which was then separately eroded and dilated three times. The areas of the eroded and dilated masks were calculated and the highest difference to the original overlapping area was taken as uncertainty. The procedure is sketched in fig. (79).
The error source for the evaluation of the contact area are falsely classified pixels. The classification models created from the machine learning segmentation do not classify the images 100 % correctly, thus a model error has to be estimated. This was done by manually classifying 10 representative 2D cross-sections (5 x- and 5 y-cross-sections) for every tomogram and comparing them to the output of the *Weka*-segmentation [41]. In detail, the difference between the contact lengths of the two 2D images was calculated in percent and averaged. Taking only the ratio of falsely classified pixels to total pixels would not be representative, as it highly depends on the total number of pixels and would result in too low uncertainties. The uncertainties for the opening thickness maps, i.e., the gaps between the fibers, were calculated in a similar fashion. For the manually classified and the *Weka*-classified 2D cross-sections, the 1D opening thickness (the opening thickness for a single slice) was calculated. Then, for every pixel, the difference between these two images was calculated in percent, averaged and taken as uncertainty. The uncertainties for the different tomograms are listed in tab. (7).

The uncertainty of the RCA was calculated with the total differential and yields an upper and lower bound.

$$\Delta RCA(A_\mathrm{C}, A_\mathrm{I}) = \left|\frac{\partial RCA(A_\mathrm{C}, A_\mathrm{I})}{\partial A_\mathrm{C}}\right|\Delta A_\mathrm{C} + \left|\frac{\partial RCA(A_\mathrm{C}, A_\mathrm{I})}{\partial A_\mathrm{I}}\right|\Delta A_\mathrm{I} = \frac{\Delta A_\mathrm{C}}{A_\mathrm{I}} + \frac{A_\mathrm{C}\Delta A_\mathrm{I}}{A_\mathrm{I}^2} \quad (46)$$

RCA ... relative contact area
A_C ... contact area
A_I ... intersection area

Comparison to Literature A thorough literature research yields that the so far best resolution on measurements of FtF-bonds was reported by Sormunen et al. [7]. As explained in section 2.1.3, they utilized X-ray nanotomography which resulted in 3D reconstructions with a voxel size of 65 nm. The device was empirically determined to have a resolution of 128 nm, though this does not take into account the sample type and the 3D reconstructions. Hence, the resolution of the 3D reconstructions is probably worse. Another problem regarding the reconstructions was the low contrast and the rather poor signal to noise ratio. In contrast, PXCT does away with these problems, since the main source of contrast for weakly scattering samples like cellulose is usually the phase [70]. Furthermore, the PXCT reconstructions provided an isotropic image resolution below 100 nm for

Tab. 7: Estimation of the uncertainties of the intersection area, contact area and gap thickness
Exp. ... experiment identification
Unc. A_I ... uncertainty of intersection area / µm^2
FCP ... falsely classified pixels - ratio of falsely classified pixels to overall classified pixels / %
Unc. A_C ... uncertainty of contact area / %
Unc. GT ... uncertainty of thickness of gap between the two fibers / %

Exp.	Unc. A_I / µm^2	FCP / %	Unc. A_C / %	Unc. GT / %
C_1	9	0.6	1.6	6
C_3	6	0.9	2.8	8
C_4	6	0.7	2.6	6

the measurements where radiation damage was not observed, proving the advantages of this method. Sormunen et al. successfully imaged and analyzed 26 FtF-bonds made of bleached softwood kraft pulp, revealing an average RCA of $(57.7 \pm 0.8)\,\%$. The results of this Master's Thesis are similar with $(64 \pm 4)\,\%$, $(66 \pm 6)\,\%$ and $(65 \pm 6)\,\%$, though the results are not statistically significant.
Furthermore, the opening thickness maps show a similar characteristic to the ones in Sormunen's Master's Thesis [15]. Often, the edges show non-contact characteristics between the fibers. This can be explained on the one hand by the analysis procedure, where the overlapping region is determined visually. If the overlapping area is chosen too big, the air outside the intersection area would show non-contact regions at the edges of the opening thickness map. Though, this is considered in the uncertainty calculation of the intersection area. On the other hand, the edges of the fibers are usually rounded, which makes it obvious that the fibers cannot be in contact in such regions.

5.6 Mass Density Estimation

With the knowledge of the chemical composition of the cellulose fibers, it was also possible to estimate the mass density $\rho(\vec{r})$ of the samples, as ptychography provides quantitative electron density maps. The mass density can be obtained from the electron density $n_e(\vec{r})$ by following equation [9]:

$$\rho(\vec{r}) = \frac{n_e(\vec{r})A}{N_A Z} \tag{47}$$

A ... molar mass
Z ... total number of electrons in the molecule
N_A ... Avogadro constant

The hardwood fibers, used for the experiments, consisted of 77 % cellulose and 23 % hemicellulose. Since the exact composition of the hemicellulose was not known, it was treated as cellulose for the calculation. Thus, the chemical structure $C_{12}H_{20}O_{10}$ was used, resulting in a molar mass of $324.28\,\mathrm{g\,mol^{-1}}$ and a total number of 172 electrons per molecule. The mass density calculation was not performed for the softwood fiber due to the presence of radiation damage and artifacts in the tomographic reconstructions.

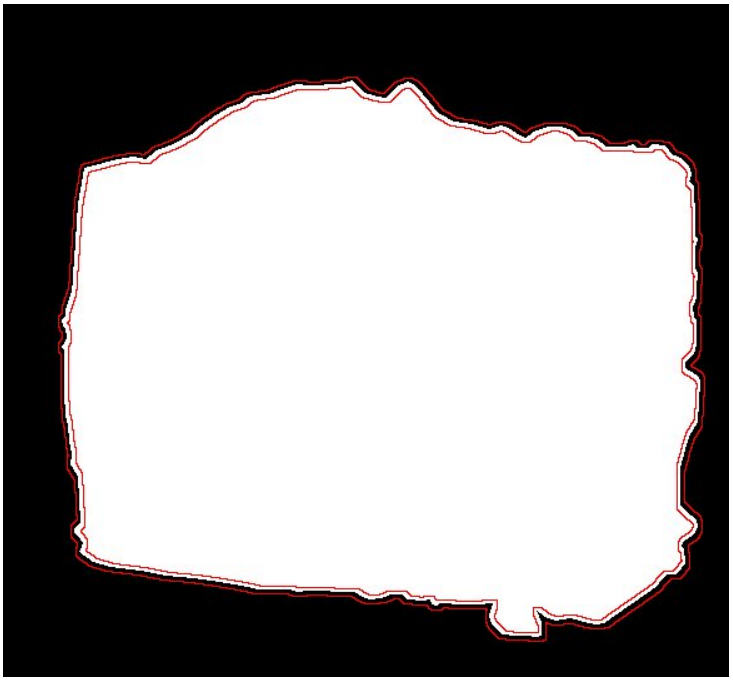

Fig. 79: Illustration of the uncertainty evaluation of the intersection area
The mask was separately eroded and dilated 3 times. The highest difference in area to the original mask was taken as uncertainty. The perimeters are highlighted in red.

For the analysis, a certain sub-volume, only containing cellulose, was selected in the electron density stack, as shown exemplary in fig. (80) for the tomogram of experiment C_1. Then, a histogram of the electron density values was created, which fitted very well a Gaussian distribution indicated by a line (see fig.(81)). The center of the distribution and the standard deviation were used to calculate the mass density according to eq. (47) and its error. To confirm the homogeneity of the chosen region, the standard deviation of a volume with similar size within a region in air was calculated [9]. It fits with the standard deviation of the area within the cellulose fibers, confirming the homogeneity. The resulting values are listed in tab. (8).

When comparing with literature, the obtained density values seem reasonable. The density of crystalline cellulose for the phases I_α and I_β, which are the most common in nature, are $1.582\,\mathrm{g\,cm^{-3}}$ and $1.599\,\mathrm{g\,cm^{-3}}$, respectively [71]. Thus, the density of pulp cellulose should be less, as it is not completely crystalline. Furthermore, a recent study by Daicho et al. [72] reports a value of $1.57\,\mathrm{g\,cm^{-3}}$ for bleached kraft pulp softwood cellulose. The fiber type is different, but the processing is similar, thus a comparison is justified. However, it has to be mentioned, that the obtained values are only estimates, as the exact composition of the hemicelluloses was not known.

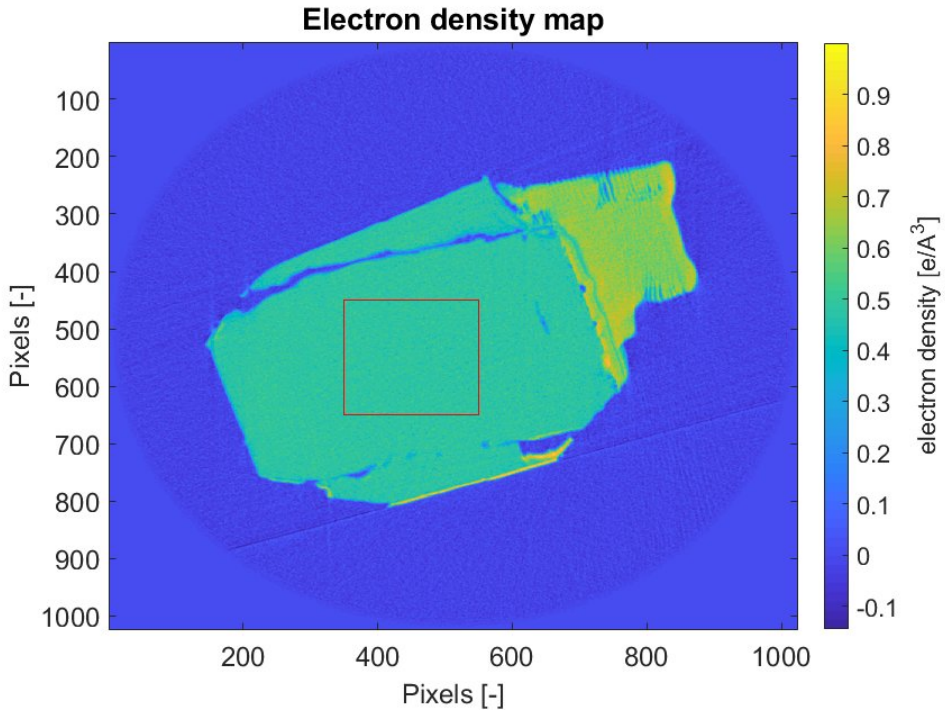

Fig. 80: 2D cross-section of tomogram C_1 (Slice 65) displaying electron density
The region indicated by a red square was used for the estimation of mass density

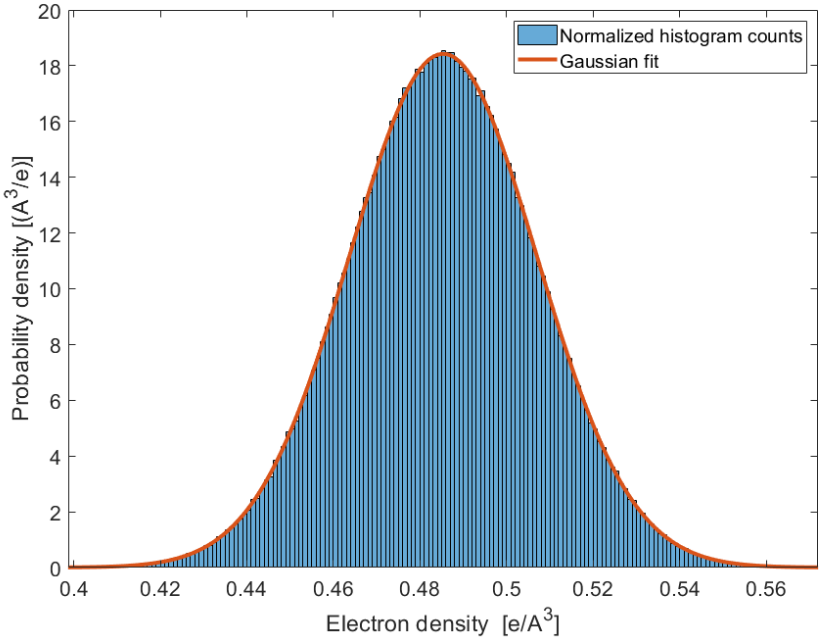

Fig. 81: Histogram with Gaussian fit of a region in the sample marked in fig. (80)

Tab. 8: Estimation of the mass density
Exp. ... experiment identification
Vol. ... volume for mass density calculation / µm^3
μ_e ... mean of Gaussian fit of electron density values within cellulose / Å^{-3}
σ_c ... standard deviation of Gaussian fit of electron density values within cellulose / Å^{-3}
σ_{air} ... standard deviation of electron density values within air / Å^{-3}
ρ ... estimation of mass density / g cm^{-3}

Exp.	Vol. / µm^3	μ_e / Å^{-3}	σ_c / Å^{-3}	σ_{air} / Å^{-3}	ρ / g cm^{-3}
C_1	34.4	0.4853	0.0216	0.0192	1.52 ± 0.07
C_2	34.4	0.4827	0.0179	0.0160	1.51 ± 0.06
C_3	1.5	0.4909	0.0201	0.0190	1.54 ± 0.07
C_4	1.5	0.4877	0.0140	0.0130	1.53 ± 0.05

6 Conclusions and Outlook

This work demonstrated that PXCT is a valuable tool for the characterization of cellulosic materials, if the right parameters and setup are used. PXCT not only offers high-resolution 3D reconstructions of the sample morphology, but also quantitative values of the sample's refractive index, thus allowing for 3D maps of the electron density and the calculation of the average mass density. Utilizing this technique, in total three FtF-bonds were measured at the cSAXS beamline at the Swiss Light Source synchrotron facility. Two FtF-bonds formed from bleached hardwood kraft pulp were measured at cryogenic temperatures and ultra-high vacuum and one FtF-bond consisting of unbleached softwood kraft pulp fibers was measured at ambient conditions. These samples were prepared by using a scanning electron microscope and focused ion beam milling and fixing the samples via carbon deposition. In addition, several samples were prepared manually. Though this turned out to be rather challenging, as the length scale of FtF-bonds is in the regime of tens of micrometers. Furthermore, these samples were fixed with glue or nail polish instead of carbon deposition and the behavior of glue and nail polish upon X-ray irradiation is not known, thus these samples were not measured. However, measuring such samples would be interesting for future experiments, as the preparation is more cost-efficient compared to the sophisticated approach using SEM and FIB.

The softwood sample was measured with parameters leading to a high radiation dose. Accordingly, the sample suffered immense radiation damage, resulting in artifacts in the reconstructions and bad image resolution. To counteract the radiation damage, the two hardwood samples were measured with parameters leading to a lower radiation dose imparted to the sample. This resulted in reconstructions with a resolution in the range of $50 - 90\,\mathrm{nm}$ and hardly any artifacts. Hence, within the framework of this thesis, the optimal parameters for such measurements were found. In general, a rather low photon flux should be used and low temperatures and a good cooling of the sample should be ensured.

The 3D reconstructions were processed via image segmentation and additional image processing steps. However, image segmentation was challenging due to the carbon from the fixations and difficulties in the detection of small non-contact regions between the two fibers. An improvement for future experiments would be to leave the overlaying arms of the cellulose fibers slightly bigger and fix the sample with carbon in this area. Thus, the carbon would be further away from the intersection area, making image segmentation easier.
Nevertheless, the segmentation was performed successfully using a machine learning approach. The relative contact area was estimated for both hardwood samples. The estimate for the first sample is $(64 \pm 4)\,\%$. For the second sample two estimates were calculated from two different measurements. The result is $(66 \pm 6)\,\%$ and $(65 \pm 6)\,\%$, respectively. Since only two samples were measured, these values are not statistically significant, but they are in agreement with the results of a recent study by Sormunen et al. [7], who found a value of $(57.7 \pm 0.8)\,\%$ with a sample size of 26. Though it has to be mentioned, that the resolution and the overall image quality of the 3D reconstructions in this Master's Thesis is better, showing the advantage of PXCT over other techniques.

Additionally, the 3D reconstructions allowed for an estimation of the mass density. For

both hardwood samples two estimates were obtained, respectively, yielding values of $(1.52 \pm 0.07)\,\mathrm{g\,cm^{-3}}$ and $(1.51 \pm 0.06)\,\mathrm{g\,cm^{-3}}$ for one sample, $(1.54 \pm 0.07)\,\mathrm{g\,cm^{-3}}$ and $(1.53 \pm 0.05)\,\mathrm{g\,cm^{-3}}$ for the other sample.

In conclusion, this work has proven that **PXCT is a promising technique** for the characterization of cellulosic materials. Furthermore, it was shown that **radiation damage to cellulose is relevant** and has to be considered, in measurements with ionizing radiation. Moreover, the **optimal parameters** for measurements with this technique to prevent radiation damage, were determined. A further finding was that **manual sample preparation is challenging**, due to the small length scales in the micrometer regime and the unknown behaviour of glues upon X-ray irradiation. In addition the **relative contact area** between two bonded cellulose fibers was estimated from 3D reconstructions with a resolution in the range from 50 to 90 nm and a voxel size of 37.6 nm. A thorough search of the relevant literature yields that this is the so far best resolution reported on measurements of cellulose fiber to fiber bonds. Furthermore, the 3D reconstructions allowed for an **estimation of the mass density**.

This Master's Thesis is a proof of principle, that PXCT is a measurement technique that is capable of finally resolving FtF-bonds with a resolution down to 30 nm, where intermolecular bonding mechanisms start to play a role. Hence, the findings of this work could serve as a basis for future experiments.

References

[1] A. Breitkopf, "Papier- und pappeverbrauch in europa nach sektoren in den jahren 2009 bis 2018." `https://bit.ly/30fhGyB`. Last accessed: 2020-06-04.

[2] G. Thompson, J. Swain, M. Kay, and C. Forster, "The treatment of pulp and paper mill effluent: a review," *Bioresource Technology*, vol. 77, pp. 275–286, May 2001.

[3] D. Page, "A theory for the tensile strength of paper," *Tappi*, vol. 52, pp. 674–681, Apr. 1969.

[4] H. Li, H. Zhang, F. Zhang, X. Li, S. Legere, and Y. Ni, "Determination of interfiber bonded area based on the confocal laser scanning microscopy technique," *Industrial & Engineering Chemistry Research*, vol. 57, pp. 6153–6160, Apr. 2018.

[5] L. Kappel, U. Hirn, W. Bauer, and R. Schennach, "A novel method for the determination of bonded area of individual fiber-fiber bonds," *Nordic Pulp & Paper Research Journal*, vol. 24, pp. 199–205, May 2009.

[6] L. Kappel, U. Hirn, W. Bauer, E. Gilli, and R. Schennach, "Revisiting polarized light microscopy for fiber-fiber bond area measurement - part II: Proving the applicability," *Nordic Pulp & Paper Research Journal*, vol. 25, pp. 71–75, Jan. 2010.

[7] T. Sormunen, A. Ketola, A. Miettinen, J. Parkkonen, and E. Retulainen, "X-ray nanotomography of individual pulp fibre bonds reveals the effect of wall thickness on contact area," *Scientific Reports*, vol. 9, Mar. 2019.

[8] M. Holler, A. Diaz, M. Guizar-Sicairos, P. Karvinen, E. Färm, E. Härkönen, M. Ritala, A. Menzel, J. Raabe, and O. Bunk, "X-ray ptychographic computed tomography at 16 nm isotropic 3d resolution," *Scientific Reports*, vol. 4, Jan. 2014.

[9] A. Diaz, P. Trtik, M. Guizar-Sicairos, A. Menzel, P. Thibault, and O. Bunk, "Quantitative x-ray phase nanotomography," *Physical Review B*, vol. 85, Jan. 2012.

[10] U. Schmitt, G. Koch, and R. Lehnen, *Wood (in Ullmann's Encyclopedia of Industrial Chemistry)*. Wiley, 2014.

[11] D. Fengel and G. Wegener, *Wood: chemistry, ultrastructure, reactions*. De Gruyter Berlin New York, 1984.

[12] E. Brännvall, *Pulp and Paper Chemistry and Technology: Pulping Chemistry and Technology - Chapter 1*. De Gruyter, Jan. 2009.

[13] A. C. O'SULLIVAN, "Cellulose: the structure slowly unravels," *Cellulose*, vol. 4, no. 3, pp. 173–207, 1997.

[14] W. Stelte and A. R. Sanadi, "Preparation and characterization of cellulose nanofibers from two commercial hardwood and softwood pulps," *Industrial & Engineering Chemistry Research*, vol. 48, pp. 11211–11219, Dec. 2009.

[15] T. Sormunen, *Measuring the contact area in cellulose fibre bonds using X-ray nanotomography*. MSc Thesis, University of Jyväskylä, Mar. 2018.

[16] M. Hubbe, "Bonding between cellulosic fibers in the absence and presence of dry-strength agents - a review," *BioResources*, vol. 1, pp. 281–318, Nov. 2006.

[17] U. Hirn and R. Schennach, "Comprehensive analysis of individual pulp fiber bonds quantifies the mechanisms of fiber bonding in paper," *Scientific Reports*, vol. 5, May 2015.

[18] T. Lindström, L. Wågberg, and T. O. Larsson, "On the nature of joint strength in paper - a review of dry and wet strength resins in paper manufacturing," *Advances in Paper Science and Technology, 13th Fund. Res. Symp. Cambridge*, pp. 457–562, Sept. 2005.

[19] C. Ganser, U. Hirn, S. Rohm, R. Schennach, and C. Teichert, "AFM nanoindentation of pulp fibers and thin cellulose films at varying relative humidity," *Holzforschung*, vol. 68, pp. 53–60, Jan. 2014.

[20] R. Pelton, "A model of the external surface of wood pulp fibers," *Nordic Pulp & Paper Research Journal*, vol. 8, pp. 113–119, Jan. 1993.

[21] U. Hirn, R. Schennach, C. Ganser, M. Magnusson, C. Teichert, and S. Ostlund, "The area in molecular contact in fiber-fiber bonds," *Advances in Paper Research, 15th Fund. Res. Symp. Cambridge*, pp. 201–223, Sept. 2013.

[22] B. N. J. Persson, "Capillary adhesion between elastic solids with randomly rough surfaces," *Journal of Physics: Condensed Matter*, vol. 20, p. 315007, June 2008.

[23] W. Haselton, "Gas adsorption by wood, pulp and paper," *Tappi*, vol. 37, pp. 404–412, Jan. 1954.

[24] A. Torgnysdotter, A. Kulachenko, P. Gradin, and L. Wågberg, "The link between the fiber contact zone and the physical properties of paper: A way to control paper properties," *Journal of Composite Materials*, vol. 41, pp. 1619–1633, July 2007.

[25] G. Urstöger, M. G. Simoes, A. Steinegger, R. Schennach, and U. Hirn, "Evaluating the degree of molecular contact between cellulose fiber surfaces using FRET microscopy," *Cellulose*, vol. 26, pp. 7037–7050, June 2019.

[26] L. Kappel, *Development and Application of a Method for Fiber-Fiber Bonded Area Measurement*. PhD Thesis, Graz University of Technology, Feb. 2010.

[27] M. Dierolf, *Ptychographic X-ray Microscopy and Tomography*. Technical University of Munich, Mar. 2015.

[28] W. Demtröder, *Experimentalphysik 2*. Springer Berlin Heidelberg, 2013.

[29] R. Hegerl and W. Hoppe, "Dynamische theorie der kristallstrukturanalyse durch elektronenbeugung im inhomogenen primärstrahlwellenfeld," *Berichte der Bunsengesellschaft für physikalische Chemie*, vol. 74, pp. 1148–1154, Nov. 1970.

[30] W. Hoppe, "Beugung im inhomogenen primärstrahlwellenfeld. i. prinzip einer phasenmessung von elektronenbeugungsinterferenzen," *Acta Crystallographica Section A*, vol. 25, pp. 495–501, July 1969.

[31] J. Rodenburg, "Ptychography and related diffractive imaging methods," in *Advances in Imaging and Electron Physics*, pp. 87–184, Elsevier, 2008.

[32] F. van der Veen and F. Pfeiffer, "Coherent x-ray scattering," *Journal of Physics: Condensed Matter*, vol. 16, pp. 5003–5030, July 2004.

[33] R. Bates and J. Rodenburg, "Sub-ångström transmission microscopy: A fourier transform algorithm for microdiffraction plane intensity information," *Ultramicroscopy*, vol. 31, pp. 303–307, Nov. 1989.

[34] H. M. L. Faulkner and J. M. Rodenburg, "Movable aperture lensless transmission microscopy: A novel phase retrieval algorithm," *Physical Review Letters*, vol. 93, July 2004.

[35] P. Thibault, M. Dierolf, O. Bunk, A. Menzel, and F. Pfeiffer, "Probe retrieval in ptychographic coherent diffractive imaging," *Ultramicroscopy*, vol. 109, pp. 338–343, Mar. 2009.

[36] V. Elser, "Phase retrieval by iterated projections," *Journal of the Optical Society of America A*, vol. 20, p. 40, Jan. 2003.

[37] V. Elser, "Random projections and the optimization of an algorithm for phase retrieval," *Journal of Physics A: Mathematical and General*, vol. 36, pp. 2995–3007, Mar. 2003.

[38] M. Guizar-Sicairos, A. Diaz, M. Holler, M. S. Lucas, A. Menzel, R. A. Wepf, and O. Bunk, "Phase tomography from x-ray coherent diffractive imaging projections," *Optics Express*, vol. 19, p. 21345, Oct. 2011.

[39] X. Huang, H. Yan, R. Harder, Y. Hwu, I. K. Robinson, and Y. S. Chu, "Optimization of overlap uniformness for ptychography," *Optics Express*, vol. 22, p. 12634, May 2014.

[40] P. Thibault and M. Guizar-Sicairos, "Maximum-likelihood refinement for coherent diffractive imaging," *New Journal of Physics*, vol. 14, p. 063004, June 2012.

[41] I. Arganda-Carreras, V. Kaynig, C. Rueden, K. W. Eliceiri, J. Schindelin, A. Cardona, and H. S. Seung, "Trainable weka segmentation: a machine learning tool for microscopy pixel classification," *Bioinformatics*, vol. 33, pp. 2424–2426, Mar. 2017.

[42] N. Otsu, "A threshold selection method from gray-level histograms," *IEEE Transactions on Systems, Man, and Cybernetics*, vol. 9, pp. 62–66, Jan. 1979.

[43] J. Schindelin, I. Arganda-Carreras, E. Frise, V. Kaynig, M. Longair, T. Pietzsch, S. Preibisch, C. Rueden, S. Saalfeld, B. Schmid, J.-Y. Tinevez, D. J. White, V. Hartenstein, K. Eliceiri, P. Tomancak, and A. Cardona, "Fiji: an open-source platform for biological-image analysis," *Nature Methods*, vol. 9, pp. 676–682, June 2012.

[44] M. Hall, E. Frank, G. Holmes, B. Pfahringer, P. Reutemann, and I. H. Witten, "The WEKA data mining software," *ACM SIGKDD Explorations Newsletter*, vol. 11, pp. 10–18, Nov. 2009.

[45] L. Breiman, "Random forests," *Machine Learning*, vol. 45, no. 1, pp. 5–32, 2001.

[46] A. Ziegler and I. R. König, "Mining data with random forests: current options for real-world applications," *Wiley Interdisciplinary Reviews: Data Mining and Knowledge Discovery*, vol. 4, pp. 55–63, Dec. 2013.

[47] L. Breiman, "Bagging predictors," *Machine Learning*, vol. 24, pp. 123–140, Aug. 1996.

[48] P. S. Institut, "csaxs website." `http://www.psi.ch/sls/csaxs`. Last accessed: 2020-05-23.

[49] P. S. Institut, "csaxs notes v1.02." `https://www.psi.ch/sites/default/files/import/sls/csaxs/ManualsEN/csaxs_notes.pdf`. Last accessed: 2020-05-23.

[50] M. Holler, J. Raabe, A. Diaz, M. Guizar-Sicairos, C. Quitmann, A. Menzel, and O. Bunk, "An instrument for 3d x-ray nano-imaging," *Review of Scientific Instruments*, vol. 83, p. 073703, July 2012.

[51] M. Holler, J. Raabe, A. Diaz, M. Guizar-Sicairos, R. Wepf, M. Odstrcil, F. R. Shaik, V. Panneels, A. Menzel, B. Sarafimov, S. Maag, X. Wang, V. Thominet, H. Walther, T. Lachat, M. Vitins, and O. Bunk, "OMNY—a tOMography nano crYo stage," *Review of Scientific Instruments*, vol. 89, p. 043706, Apr. 2018.

[52] P. S. Institut, "Pxct setup." `https://www.psi.ch/en/sls/csaxs/software`. Last accessed: 2020-05-23.

[53] I. Johnson, A. Bergamaschi, H. Billich, S. Cartier, R. Dinapoli, D. Greiffenberg, M. Guizar-Sicairos, B. Henrich, J. Jungmann, D. Mezza, A. Mozzanica, B. Schmitt, X. Shi, and G. Tinti, "Eiger: a single-photon counting x-ray detector," *Journal of Instrumentation*, vol. 9, pp. C05032–C05032, May 2014.

[54] M. Holler and J. Raabe, "Error motion compensating tracking interferometer for the position measurement of objects with rotational degree of freedom," *Optical Engineering*, vol. 54, p. 054101, May 2015.

[55] M. Guizar-Sicairos, M. Holler, A. Diaz, J. Vila-Comamala, O. Bunk, and A. Menzel, "Role of the illumination spatial-frequency spectrum for ptychography," *Physical Review B*, vol. 86, Sept. 2012.

[56] M. Holler, J. Raabe, R. Wepf, S. H. Shahmoradian, A. Diaz, B. Sarafimov, T. Lachat, H. Walther, and M. Vitins, "OMNY PIN—a versatile sample holder for tomographic measurements at room and cryogenic temperatures," *Review of Scientific Instruments*, vol. 88, p. 113701, Nov. 2017.

[57] R. Stratton, "Fundamentals of internal strength enhancement part 2 – studies on the bonding of single fibers," *Progress Report. Institute of Paper Science and Technology. Atlanta, Georgia*, July 1992.

[58] W. Demtröder, *Experimentalphysik 1.* Springer Berlin Heidelberg, 2015.

[59] M. Howells, T. Beetz, H. Chapman, C. Cui, J. Holton, C. Jacobsen, J. Kirz, E. Lima, S. Marchesini, H. Miao, D. Sayre, D. Shapiro, J. Spence, and D. Starodub, "An assessment of the resolution limitation due to radiation-damage in x-ray diffraction microscopy," *Journal of Electron Spectroscopy and Related Phenomena*, vol. 170, pp. 4–12, Mar. 2009.

[60] E. Gullikson, "X-ray attenuation length." `http://henke.lbl.gov/optical_constants/atten2.html`. Last accessed: 2020-06-18.

[61] B. Henke, E. Gullikson, and J. Davis, "X-ray interactions: Photoabsorption, scattering, transmission, and reflection at e = 50-30,000 eV, z = 1-92," *Atomic Data and Nuclear Data Tables*, vol. 54, pp. 181–342, July 1993.

[62] R. Henderson, "Cryo-protection of protein crystals against radiation damage in electron and x-ray diffraction," *Proceedings of the Royal Society of London. Series B: Biological Sciences*, vol. 241, pp. 6–8, July 1990.

[63] J. Polvi, P. Luukkonen, K. Nordlund, T. T. Järvi, T. W. Kemper, and S. B. Sinnott, "Primary radiation defect production in polyethylene and cellulose," *The Journal of Physical Chemistry B*, vol. 116, pp. 13932–13938, Nov. 2012.

[64] M. Odstrčil, M. Holler, J. Raabe, and M. Guizar-Sicairos, "Alignment methods for nanotomography with deep subpixel accuracy," *Optics Express*, vol. 27, pp. 36637–36652, Dec. 2019.

[65] G. Harauz and M. van Heel, "Exact filters for general geometry three dimensional reconstruction," *Optik (Stuttgart)*, vol. 73, no. 4, pp. 146–156, 1986.

[66] S. W. Smith, *The Scientist and Engineer's Guide to Digital Signal Processing*. California Technical Publishing, 1997. Available at www.dspguide.com.

[67] W. O. Saxton and W. Baumeister, "The correlation averaging of a regularly arranged bacterial cell envelope protein," *Journal of Microscopy*, vol. 127, pp. 127–138, Aug. 1982.

[68] M. van Heel, W. Keegstra, W. Schutter, and E. J. F. van Bruggen, "Arthropod hemocyanin structures studied by image analysis," *Life Chemistry Reports, Suppl. 1, "The Structure and Function of Invertebrate Respiratory Proteins", EMBO Workshop*, pp. 63–73, 1982.

[69] M. van Heel and M. Schatz, "Fourier shell correlation threshold criteria," *Journal of Structural Biology*, vol. 151, pp. 250–262, Sept. 2005.

[70] S. Sala, D. J. Batey, A. Prakash, S. Ahmed, C. Rau, and P. Thibault, "Ptychographic x-ray computed tomography at a high-brilliance x-ray source," *Optics Express*, vol. 27, p. 533, Jan. 2019.

[71] J. Sugiyama, R. Vuong, and H. Chanzy, "Electron diffraction study on the two crystalline phases occurring in native cellulose from an algal cell wall," *Macromolecules*, vol. 24, pp. 4168–4175, July 1991.

[72] K. Daicho, K. Kobayashi, S. Fujisawa, and T. Saito, "Crystallinity-independent yet modification-dependent true density of nanocellulose," *Biomacromolecules*, vol. 21, pp. 939–945, Dec. 2019.

List of Figures

List of Tables